Benchmark Flight Scenarios for Testing Fault Tolerant Control in High Performance Aircraft

Thesis Report

J.M. BAKKER

Benchmark Flight Scenarios for Testing Fault Tolerant Control of High Performance Aircraft

Thesis Report

by

J.M. Bakker

to obtain the degree of Master of Science

at the Delft University of Technology,

Student number:	4016076
Project duration:	August 1, 2017 – April 22, 2019
Supervisor:	Prof. dr. ir. C.C. de Visser, TU Delft
Date:	26-02-2019

Summary

One of the most essential systems for fly-by-wire aircraft is the Flight Control System (FCS) which can control the aircraft successfully based on pilot or autopilot inputs. The FCS is designed for standard flight conditions under the assumptions all the control effectors work perfectly. The ability of the FCS to deal with effector failures is limited to the inherent redundancy build into the system. Control related aviation accidents could be prevented if a Fault Tolerant Control (FTC) system had been present to reconfigure the FCS based on a Fault Detection and Isolation (FDI) algorithm. Nowadays research on FTC systems is mainly focused on building or adjusting aerodynamic models due to failures, however these methods are too computationally complex for real-time solutions. Furthermore the testing of these FTC is done mostly on conventional aircraft and thus challenging mission profiles like acrobatic or evasive manoeuvres are not investigated.

The focus of this research is on FTC system design, flight trajectory and autopilot design for flight performance testing of High Performance Aircraft while simulating common effector failures. The main goal is to evaluate the effectiveness of the Incremental Nonlinear Control Allocation (INCA) algorithm in case of one (or more) effector failure(s) of a tail-less over-actuated aircraft model for multiple benchmark flight trajectories. The main findings of this project will provide an answer to whether or not an adaptive incremental nonlinear dynamic inversion method will be robust enough to recover from a would be loss-of-control situation due to effector failure without the need for a degraded aerodynamic model or a recovery model.

In this work the FTC system design has been applied to the over-actuated tailles Innovative Concept Effectors (ICE) aircraft model, which is an extremely agile aircraft with 13 (unconventional) control effectors. The simulation and testing framework is set up with a high-fidelity model of the ICE aircraft, actuator and engine dynamics and the INCA algorithm. The FCS system is extended with a Fault Detection & Isolation (FDI) and autopilot module required for automatic benchmark trajectory following and FTC testing of multiple effector failure cases. Similarly a failure event module has been implemented to simulate the effector failures.

A sensitivity analysis of the experiment parameters showed that varying failure time and trim conditions have a high influence on the tracking performance and failure case analysis. For all four benchmark flight trajectories a hard-over of the Spoiler-slot deflectors (SSDs) decreased aircraft flight performance such that a loss-of-control event is highly likely. For the evasive flight manoeuvre, a hard-over of Thrust Vectoring (TV) in both directions for all tested conditions leads to loss-of-control. Depending on the flight condition during the evasive flight manoeuvre a hard-over of any effector has to possibility to cause loss-of-control. The failure time during a manoeuvre does effect which effector are more critical. During this yaw-critical manoeuvre where the aircraft has to change its heading within ten seconds a hard-over or lock-in-place is thus detrimental to the aircraft performance. Furthermore a hard-over of the yaw TV led to unacceptable load limits (>20) for all failure conditions tested during this manoeuvre.

Future directions and application can be automatic recovery trajectories following critical failure, i.e. for a maximum SSD failure in straight flight the flight control system could switch to a turning manoeuvre to prevent loss-of-control event. Moreover one can investigate other types of effector failures that were not investigated in this paper. Also essential flight trajectories like the final landing flare mode can be added to simulate a complete flight.

Preface

Dear reader,

In this document you will find my Master's Thesis project report, which I have been working on for over a year. Although this report represent the end of being a student at the TU Delft, which has been an amazing time of my life, I am looking forward to venture out in the world with the knowledge, engineering values and inspirational ideas from Delft.

Recent aircraft incidents with the Boeing 777-max highlighted the relevance of well-tested fault tolerant flight control systems, which is main topic of this report. This reports can be divided in three parts. The first three chapters after the introduction mainly describe the state-of-the art methods that were used as a basis for my research. Followed by two chapters which describes benchmark information which can be used for future research efforts on the ICE aircraft model and in the last chapters the results are analysed and discussed. I also made a compact version of my thesis in AIAA paper format, which can be used for a future paper submission. This paper is included in as appendix.

I want to thank my daily supervisor Coen de Visser for his guidance and advice. Also I like to thank Michael Niestroy for providing us with the opportunity to work with model of ICE. Special thanks to my wife Panchamy Krishnakumari for providing love and support. I thank my parents for their support throughout my career and my brother, my family, my colleagues at Proficium and my friends from Delft and outside of Delft.

J.M. Bakker
Delft, April 2019

Contents

List of Figures

List of Tables

List of Abbreviations

AFTC Active Fault Tolerant Control 23

AMT All Moving Wing Tip 6

AOA angle of attack 7

CA Control Allocation 2

DLEF Differential Leading Edge Flaps 6

DOF degrees-of-freedom 5

FDD Fault Detection and Diagnosis 23

FDI Fault Detection and Isolation 23

FTC Fault Tolerant Control 3

FDI Fault Detection and Isolation 23

LAMT Left All Moving Wing Tip 11

LELE Left Elevon 11

LPV Linear Parameter Varying 2

ICE	Innovative Control Effectors	3
INCA	Incremental Nonlinear Control Allocation	3
MM	Multiple Model	2
NDI	Nonlinear Dynamic Inversion	2
NN	Neural Network	2
PCH	Pseudo-control Hedging	ix
QP	Quadratic Programming	ix
RCS	Low radar cross section	2
PFTC	Passive Fault Tolerant Control	23
RFCS	Reconfigurable Flight Contol System	23
RWPI	Redistributed Weighted Pseudo-Inverse	17
SMC	Sliding Modes Control	2
SSD	Spoiler-Slot Deflector	6
TED	Trailing edge down	7
TV	Thrust Vectoring	xiii

List of Symbols

$\bar{q}$	Dynamic pressure, lb/ft^2
$\dot{p}, \dot{q}, \dot{r}$	roll, pitch and yaw angular acceleration, rad/s^2
$A_{x,y,z}$	Body accelerations, ft^2/s
$C_{L,M,N}$	Body moment coefficients
$C_{X,Y,Z}$	Body force coefficients
d	Pseudo-control input
I	Identity Matrix
J	Cost Function
J	Inertia matrix
M	Mach number
p, q, r	Roll, pitch and yaw rate, rad/s
t	Time. sec
u	Pseudo-control input vector
u, v, w	Body velocities, ft/s
V	Velocity
x	State vector
y	Output vector

Greek Symbols

α	Aerodynamic angle of attack, deg

β	Aerodynamic angle of sideslip, deg
δ	Control surface deflection, deg
ϵ	Weighting factor for the mixed optimization problem
ν	Virtual control
ω	Vector of angular body rates, rad/s
ρ	Air density, kg/m^3
σ	step size
τ	Vector of body-axis aerodynamic moments, $N \cdot m$
θ	Vector of measurable or estimated parameter

Subscripts

$lamt$	Left all-moving wing tip
lel	Left elevon
$liblef$	Left inboard leading edge flap
$loblef$	Left outboard leading edge flap
$lssd$	Left spoiler slot deflector
pf	Pitch flaps
$ramt$	Right all-moving wing tip
rel	Right elevon
$riblef$	Right inboard leading edge flap
$roblef$	Right outboard leading edge flap
$rssd$	Left spoiler slot deflector

1

Introduction

In aviation as more and more aircraft are being flown every day, the number of accidents increase. Analyzing previous aviation accidents, it can be concluded that loss-of-control is one of the major causes as indicated in [16]. In these cases, the Flight Control System (FCS) was not able to cope with the effector failures which contributed to the loss-of-control. In an attempt to improve the operation safety of aircraft, a lot of research has been done on designing active Fault Tolerant Control (FTC) systems in the last three decades. The aim of such systems is to improve the reliability and availability of the aircraft to automatically accommodate component failures while maintaining a desired performance (stability). In the field of FTC, as indicated in [2], the main challenge is to combine the research on failure detection, failure isolation, state estimation in presence of failures to design a control system that can deal with multiple actuator failures or airframe failures. In the past decades a considerable amount of research has been done on system identification approaches [15] and nonlinear control approaches [17]. Recently a new model identification method, Spline based model identification [3–5], has been used in combination with Nonlinear Dynamic Inversion (NDI) [21] to allocate the controls of a high performance aircraft subject to aerodynamic uncertainties in [24, 25]. This research is an important step towards realizing a certifiable FTC system.

In the area of FTC, one can distinguish between Active Fault Tolerant Control (AFTC) and Passive Fault Tolerant Control (PFTC) methods. The main focus of this work will be on AFTC, mainly because PFTC provide limited fault-tolerant capabilities especially for increasing fault scenarios as indicated in [11] and [27]. AFTC approaches can further be classified into nonlinear and linear methods. Most control applications are nonlinear by nature but linear methods can be applied around the equilibrium points of the system. Common linear methods that are used are gain scheduling, Multiple Model (MM) and Sliding Modes Control (SMC). Purely nonlinear approaches are feedback linearization, Nonlinear Dynamic Inversion (NDI), backstepping, Neural Network (NN), nonlinear regulator and lyapunov methods. Compared to their linear counterpart, NDI and backstepping use the well-known equations of motions of the aircraft which are valid throughout the flight envelope, while gain scheduling and Linear Parameter Varying (LPV) schemes are only designed for specific parts of the flight envelope. In most practical applications, these approaches are used in combination with each other to achieve the best overall FTC system. An historical overview of AFTC methods can be found in [27].

In this work, a nonlinear model of an over-actuated tail-less aircraft concept, the Innovative Control Effector (ICE) aircraft model, is used to investigate the performance of a newly developed control scheme, subject to multiple effector failures. The ICE program focuses on highly manoeuvrable fighter aircraft without vertical tails. Tailless aircraft are considered the next generation high performance aircraft, mainly because of the radar beam signature reduction as well as weight and drag reduction. Increased manoeuvrability and signature reduction requirements pose constrains on the geometry of the aircraft and on the controls required. To achieve Low radar cross section (RCS) designs the vertical tail is removed, the vertical control surfaces are eliminated, and the control surface edges are aligned with external airframe edges. These adjustments from conventional shaped fighters contribute to the design of an interesting new control concepts to achieve the necessary manoeuvrability and beam signature reduction.

Over-actuated aircraft can use multiple effectors to achieve the required moments, controlling the effectors and position δ is left to the Control Allocation (CA) algorithm that is designed for the aircraft. This is a non-trivial task as the performance of the aircraft is greatly effected by whichever effector is used during any flight trajectory. CA algorithms that are commonly used are the pseudo-reverse, modified pseudo-reverse, direct allocation, constrained optimization method, fixed point method or a combination of the aforementioned methods. In recent research on the ICE aircraft model, a control scheme called Incremental Nonlinear Control Allocation (INCA) has been developed in order to deal with the nonlinearities and coupling between the control effectors [18]. While this research showed this method can deal with uncertainties in its aerodynamic model, it has yet to be shown to which degree the aircraft model can deal with effector and airframe failures. Apart from investigating the INCA model in case of actuator failures, this research aims to improve upon this control scheme by supplementing an adaptive control module based on a Fault Detection and Isolation (FDI) system. Furthermore, the most important task in this work is the design of flight scenarios and performance parameters. They are made to serve as a benchmark for future research on the ICE model or any other high performance aircraft model as effector failures are yet to be tested for high performance. No standard flight trajectories of these aircraft are defined, mainly because the capabilities of high performance aircraft and their mission requirements are not openly available and differ from that of commercial aircraft.

The main objective of this research is to develop and evaluate a new Fault Tolerant Control (FTC) scheme for high-performance aircraft which is robust in case of multiple effector failures like lock-in-place or hard-overs.

The following research questions were formulated in order to be able to meet the research objective:

1. What fault-tolerant flight control scheme will be able to maintain sufficient handling qualities considering multiple effector failures for the Innovative Control Effectors (ICE) aircraft model?
    (a) What is the state-of-the art ICE aircraft concept model?
        i. To what degree has the ICE aircraft concept model been validated?
        ii. What are the characteristics of the effectors on-board the ICE aircraft model?
    (b) What does the theory state about nonlinear adaptive FTC?
        i. What does the theory state about the different mathematical tools used for nonlinear adaptive FTC?
            A. What is Adaptive Nonlinear Dynamic Inversion (ANDI)?
            B. What is adaptive Backstepping?
            C. Which of these methods is most suitable for this application?
        ii. What does the theory state about reconfiguration mechanics used for nonlinear adaptive FTC?
    (c) What is the state-of-the art research about online aerodynamic model identification?
        i. What does the theory state about Multivariate Splines for online aerodynamic model identification?
        ii. What does the theory state about the two-step method for online aerodynamic model identification?
        iii. What are the state-of-the art techniques to reduce computational complexity for real-time processing of the aerodynamic parameters/model?
2. What is the value of adding re-configurable flight control to the Incremental Nonlinear Control Allocation (INCA) model of the ICE aircraft concept?

    (a) Which effector failures, that are relevant, will be simulated for this model?
    (b) What are possible alternatives to using incremental nonlinear dynamic inversion for CA?
    (c) Is the CA allocation algorithm able to use the non-defective actuators automatically in case of actuator failure?
    (d) Is it computationally feasible to be implemented on-board and be used in real time?
    (e) Does this method guarantee stability, reliability, availability and robustness?

3. Does the control allocation using the incremental approach increase the operational safety for the fault-tolerant flight control model of the ICE aircraft concept?
    (a) Which factors contribute to increasing the operational safety?
    (b) To which degree has the operational safety been increased?
    (c) What flight manoeuvres should be tested to be able to compare them to similar research results?

The structure of this work is as follows, first, in chapter 2 the ICE model is investigated and in chapter 3 the INCA is discussed. In chapter 4 the concept of FTC design is discussed. The autopilot and benchmark flight trajectory design is elaborated in chapters 5 and 6 respectively. Results and discussion of the failure tests for all scenarios including the sensitivity analysis is discussed in chapter 7. Finally the conclusions and recommendations are given in chapter 8.

In the appendix a scientific paper of this work is included. It contains the main findings and can be used for submission to the AIAA Guidance, Navigation, and Control Conference, however the current version is not submitted or reviewed yet.

2

Innovative Control Effectors

Driven by the desire to design a more agile and less detectable fighter aircraft the ICE program was started in 1993 at the Air Force Research Laboratory. Research has shown that tailless aircraft can offer both, however new innovative controllers are necessary to provide sufficient control about the three axis (pitch, roll and yaw) as well as control techniques that can deal with complex nonlinearities. A high degree of coupling tend to exists aerodynamically between the controls for tailless configurations. The ICE program investigated a baseline vehicle and a couple of control concepts. Two baseline configurations were defined, an all-wing tailless configuration land-based configuration with a 65-deg sweep delta wing and a carrier-based configuration which has a canard-delta planform with 42-deg leading edge sweep. The ICE aircraft concept is described in two technical papers [7, 8] which are written by Kenneth M. Dorsett, the program manager. In these technical papers multiple configuration and new effectors were tested in wind tunnels, at a model scale.

The aerodynamic data of one of the most promising configuration has been made available by Lockheed Martin Aeronautics in a paper written by M.A Niestroy, 18 years after the technical papers from Kenneth M. Dorsett were written. [19] Alongside this data, a Simulink model in Matlab written by M.A. Niestory has been provided. This model does not include actuator dynamics or an engine model, it only considers the trim cases. This configuration to which this model belongs has thirteen control effectors to control six degrees-of-freedom (DOF), which can be considered a highly over-actuated aircraft. It is one of the configurations derived from the all-wing tailless land-based 101-series baseline configuration. This configuration is an all-wing tailless configuration employing a 65-deg sweep delta wing, single-engine, multi-role fighter aircraft with internal or low-observable weapons-carriage measures for reduced

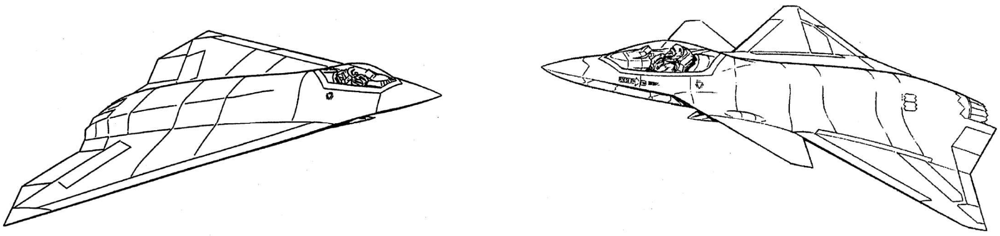

(a) The land-based baseline configuration (101-series)

(b) The carrier-based baseline configuration (201-series)

Figure 2.1: The baseline configurations considered in the ICE program [7, 8]

RCS and supersonic capability. The aircraft is equipped with innovative control concepts, the All Moving Wing Tip (AMT), inboard and outboard Differential Leading Edge Flaps (DLEF), Spoiler-Slot Deflector (SSD). Furthermore elevons and pitch flaps are used for pitch control and the aircraft is capable of pitch and yaw TV.

In this section the design phase of the ICE aircraft concept from [7, 8] is briefly covered in section 2.1. The different configurations and the innovative control effectors that were tested are explained in this section. The aerodynamic model of the configuration that will be considered in this research from [19] is discussed in section 2.2.

2.1. ICE design

As discussed in the introduction of this chapter the ICE program considered two baseline configuration, one land-based and one carrier-based configuration. These configurations are shown in figure 2.1. In the remaining of this report only the land-based 101-series is discussed and the carrier-based 102-series is outside the scope of this research.

As can be seen from figure 2.1, the ICE program focuses on highly maneuverable fighter aircraft without vertical tails. Tailless aircraft are considered the next generation high performance aircraft, mainly because of the radar beam signature reduction as well as weight and drag reduction. Increased maneuverability and signature reduction requirements pose constrains on the geometry of the aircraft and on the controls required. To achieve RCS designs the vertical tail is removed, the vertical control surfaces are eliminated, and the control surface edges are aligned with external airframe edges. These adjustments from conventional shaped fighters contribute to the design of interesting new control concepts to achieve the necessary maneuverability and beam signature reduction.

During the design phase six concepts for the baseline configuration where analyzed in a trade-off study for which a combination of a maximum of five innovative control concepts were investigated. Innovative control concepts are those controllers that are not being used or have not been used frequently enough in high performance aircraft but could be useful on the tailless design. These controls have to meet five requirements: 1) improved low signature characteristic over conventional controls, 2) improved high angle of attack (AOA) effectiveness, 3) applicability to tailless fighters, 4) potential weight and drag reduction and 5) reduced hinge moment and reduced susceptibility to aeroelastic effects as defined in [8]. The innovative control effector investigated in [8] are,

1. Clamshells. Also called drag rudders, use wing tip drag to generate yawing moment. Previously used on the B-2 bomber. Clamshell provide good yaw control for low and medium AOA, but for fighter aircraft at high AOA adverse rolling moments are being generated. Integration into fighter aircraft with short spans and thin wings is difficult.

2. Spoiler. Lateral control surface integrated into the wings, which can produce favorable roll-yaw characteristics. The downside is the loss in lift during roll maneuvers and loss of effectiveness at high AOA and transonic speeds. It will also effect any trailing edge control surfaces. At supersonic speeds the spoiler is effective, however it will require large actuators to compensate for the large hinge moment required.

3. All Moving Wing Tip. Also described as an "all-moving elevator". The AMT was already used before on the Horton H Va flying wing and testing has been done in the 1950's by NASA. The AMT produced roll moment like conventional elevators, however just like clamshells a yaw moment can be produced through increased profile and induced drag by Trailing edge down (TED) deflections. At low AOA adverse rolling moments are generated, but at high AOA favorable rolling moments. Yaw control magnitudes are in the order of an F-16 rudder at large delfections of the AMT.

4. Differential Leading Edge Flaps. DLEF provides lateral-directional control moments at moderate to high AOA. Control effectiveness is nonlinear in both roll and yaw depending on the AOA. The DLEF are also effective at high Mach conditions, but not as effective as for lower Mach.

5. Spoiler-Slot Deflector. SSD was already investigated in the 1941's for improving high AOA characteristics of lateral control devices. It is proven to lower actuator requirements, have improved high AOA and transonic effectiveness and improved control linearity over conventional spoiler arrangements. It however

requires cutting holes inside the upper wing skin and needs properly designed pitch control surfaces.

6. Deployable rudder. Presumably, used for low-speed flight conditions (take-off and landing, high AOA flight. However because of the short moment arm to the cg, it barely has any stabilizing tendencies and at high AOA result in worse overall stability than the bare airframe.
7. Lower Surface Spoiler. Although not really innovative, lower surface spoiler have been investigate to improve high AOA lateral-directional control power. It creates predictable rolling moments at high AOA, but similarly to convtional spoilers it suffers from structural integration drawbacks. Additionally these spoiler will loose there effectiveness around 10 to 20 deg AOA, loosing their usefulness for landing and approach purposes. Finally at high AOA adverse interaction with trailing edge control surfaces will result in high pitch requirements during rolls.

Not only these innovative control effectors were tested also TV in pitch and yaw was investigated. The aerodynamic control power was evaluated against the propulsion control power. After a thorough analysis of the innovative control effectors and the more conventional effectors a weighting and scoring matrix was set up and shown in figure 2.3. The AMT and TV score the hightest while the clamshell, deployable rudder and lower surface spoilers score the worst. In phase II the AMT, SSD and the DLEF were further investigated and some of their risks reduced. Mainly focusssing on where to place them and how large they should be designed as well as performing more windtunnel tests. [7]

Example: Mach 1.2 @ Sea Level
Flying Qualities Level

D 1	D 2	D 3	D 4	D 5	D 6IB	D 6OB	D 10	D 20	D 16OB	D 16IB	D 15	D 14	D 13	D 12	D 11	
X	1	2	1	X	2	X	1	2	X	2	X	1	2	1	1	D 1
	X	3	2	X	3	X	1	2	X	2	X	2	2	2	1	D 2
		X	3	X	L	X	2	3	X	3	X	3	L	2	2	D 3
			X	X	3	X	2	3	X	3	X	2	3	3	1	D 4
				X	X	X	X	X	X	X	X	X	X	X	X	D 5
					X	X	2	L	X	3	X	3	3	2	2	D 6IB
						X	X	X	X	X	X	X	X	X	X	D 6OB
							X	2	X	2	X	2	2	1	1	D 10
								X	X	L	X	3	3	2	2	D 20
									X	X	X	X	X	X	X	D 16OB
										X	X	3	L	3	2	D 16IB
											X	X	X	X	X	D 15
												X	3	2	1	D 14
													X	3	2	D 13
														X	1	D 12
															X	D 11

1 = Level 1
2 = Level 2
3 = Level 3
L = Loss-of-Control
X = Not Applicable

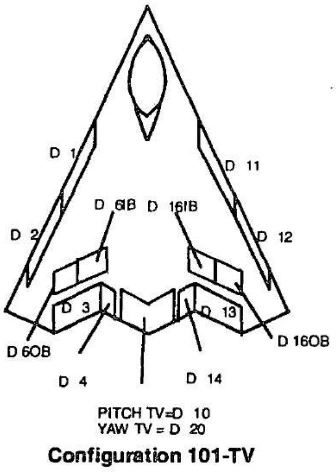

Figure 2.2: Example Control Surface Criticality Matrix 101-series [8]

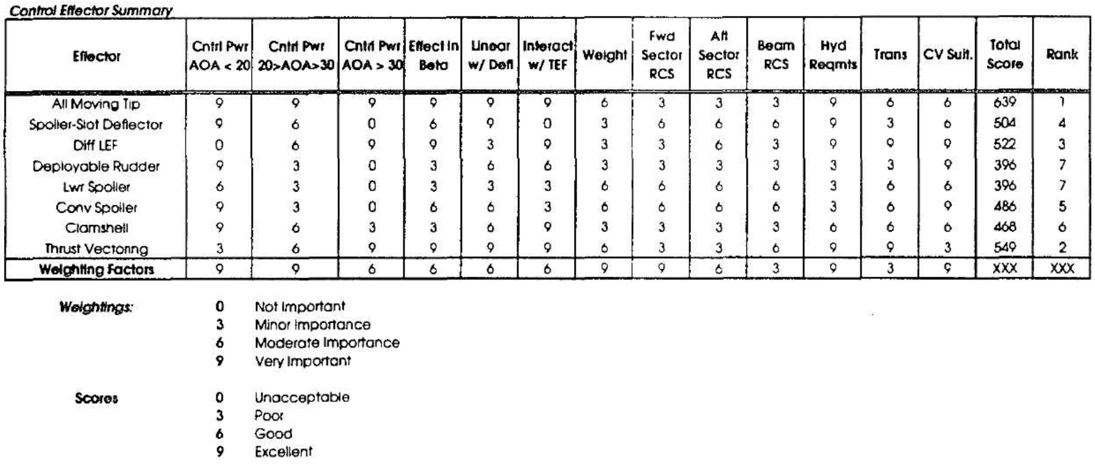

Control Effector Summary

Effector	Cntrl Pwr AOA < 20	Cntrl Pwr 20>AOA>30	Cntrl Pwr AOA > 30	Effect in Beta	Linear w/ Defl	Interact w/ TEF	Weight	Fwd Sector RCS	Aft Sector RCS	Beam RCS	Hyd Reqmts	Trans	CV Suit.	Total Score	Rank
All Moving Tip	9	9	9	9	9	9	6	3	3	3	9	6	6	639	1
Spoiler-Slot Deflector	9	6	0	6	9	0	3	6	6	6	9	3	6	504	4
Diff LEF	0	6	9	9	3	9	3	3	6	3	9	9	9	522	3
Deployable Rudder	9	3	0	3	6	6	3	3	3	3	3	3	9	396	7
Lwr Spoiler	6	3	0	3	3	3	6	6	6	6	3	6	6	396	7
Conv Spoiler	9	3	0	6	6	3	6	6	6	6	3	6	9	486	5
Clamshell	9	6	3	3	6	9	3	3	3	3	6	6	6	468	6
Thrust Vectoring	3	6	9	9	9	9	6	3	3	6	9	9	3	549	2
Weighting Factors	9	9	6	6	6	6	9	9	6	3	9	3	9	XXX	XXX

Weightings:		
	0	Not Important
	3	Minor Importance
	6	Moderate Importance
	9	Very Important
Scores	0	Unacceptable
	3	Poor
	6	Good
	9	Excellent

Figure 2.3: Control Effector weighting and scoring matrix [8]

In [8] on pages 170-173, actuator redundancy is discussed and a ranking system is made of the criticality of combined actuator failures in order to determine which effectors would require dual hydraulic systems, an example is shown in figure 2.2 This information can be used in the evaluation of the fault-tolerant ICE model that will be made in this thesis.

2.2. Aerodynamic model

In [19] the six DOF simulation model for the 65-deg sweep ICE tailless fighter aircraft that was developed from the wind tunnel test data is described. The control surfaces used on this model are the AMT, SSD, DLEF, pitch flaps and elevons. The engine is also used for trust vectoring for pitch and yaw control. A rough sketch of the approximate locations of these control effectors is shown in figure 2.4. The aerodynamic model consists of data covering a Mach number range between 0.1 and 2.16, an AOA range of -4 deg to 90 deg, and a sideslip angle range from -30 deg to 30 deg. Not all data comes directly from wind tunnel testing of this particular model, more information about the model sources can be found in [19].

The aerodynamic force and moment equations for this model are given in [19]. Coefficients in these equations are dependent up to five different variables. The moment and force coefficients given in this report are expressed in the body frame, the short hand notation of each control surface's deflection is given in table 2.1.

The force coefficients C_X, C_Y, C_Z and the moment coefficients C_L, C_M and C_N shown in equations 2.1 to 2.6 respectively consist of up to 18 coefficients. The coef-

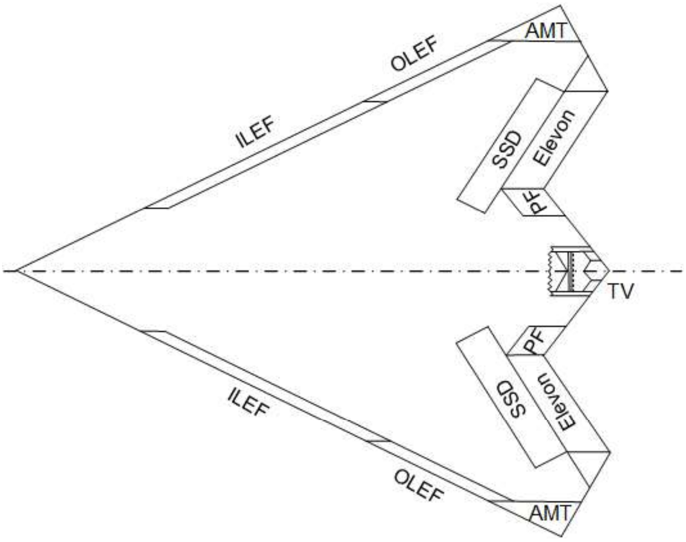

Figure 2.4: ICE control effector approximate locations

Deflection abbreviation	Description
δ_{liblef}	left inboard leading edge flap
δ_{loblef}	left outboard leading edge flag
δ_{lssd}	left spoiler slot deflector
δ_{lel}	left elevon
δ_{lamt}	left all moving wingtip
δ_{pf}	pitch flap
δ_{ramt}	right all moving wingtip
δ_{rssd}	right spoiler slot deflector
δ_{riblef}	right inboard leading edge flap
δ_{roblef}	right outboard leading edge flap
δ_{rel}	right elevon

Table 2.1: Effector deflection abbreviations used in force and moment coefficient equations

ficients that start with the Δ sign indicate increments due to the influence of the first effector on the second effector mentioned in the the dependent variables on that coefficient. For example in equation 2.1: $\Delta C_{X_8}(\alpha, \delta_{lamt}, \delta_{lel})$ means an increment increase due to the influence of the Left All Moving Wing Tip (LAMT) on the Left Elevon (LELE).

$$\begin{aligned}
C_X = {} & C_{X_1}(\alpha, M) + C_{X_2}(\alpha, \beta, M) + C_{X_3}(\alpha, \beta, M, \delta_{liblef}) \\
& + C_{X_4}(\alpha, \beta, M, \delta_{liblef}, \delta_{loblef}) + C_{X_5}(\alpha, M, \delta_{lssd}, \delta_{lel}) + C_{X_6}(\alpha, M, \delta_{lssd}, \delta_{lel}, \delta_{pf}) \\
& + C_{X_7}(\alpha, \delta_{lel}, \delta_{lamt}) + \Delta C_{X_8}(\alpha, \delta_{lamt}, \delta_{lel}) + \Delta C_{X_9}(\alpha, \delta_{loblef}, \delta_{lamt}) \\
& + \Delta C_{X_{10}}(\alpha, \delta_{ramt}, \delta_{rel}) + \Delta C_{X_{11}}(\alpha, \delta_{roblef}, \delta_{ramt}) + C_{X_{12}}(\alpha, \beta, \delta_{lssd}) \\
& + C_{X_{13}}(\alpha, \beta, \delta_{riblef}) + C_{X_{14}}(\alpha, \beta, M, \delta_{riblef}, \delta_{roblef}) + C_{X_{15}}(\alpha, M, \delta_{rssd}, \delta_{rel}) \\
& + C_{X_{16}}(\alpha, \beta, \delta_{ramt}) + C_{X_{17}}(\alpha, \beta, \delta_{rssd})
\end{aligned} \tag{2.1}$$

$$\begin{aligned}
C_Y = {} & C_{Y_1}(\alpha, M) + C_{Y_2}(\alpha, \beta, M) - C_{Y_3}(\alpha, \beta, M, \delta_{liblef}) \\
& - C_{Y_4}(\alpha, \beta, M, \delta_{liblef}, \delta_{loblef}) + C_{Y_5}(\alpha, M, \delta_{lssd}, \delta_{lel}) + C_{Y_6}(\alpha, \delta_{lel}, \delta_{lamt}) \\
& + C_{Y_7}(\alpha, \beta, \delta_{lssd}) + \Delta C_{Y_8}(\alpha, \delta_{lamt}, \delta_{lel}) + \Delta C_{Y_9}(\alpha, \delta_{loblef}, \delta_{lamt}) \\
& - \Delta C_{Y_{10}}(\alpha, \delta_{ramt}, \delta_{rel}) + \Delta C_{Y_{11}}(\alpha, \delta_{roblef}, \delta_{ramt}) + C_{Y_{12}}(\alpha, \beta, \delta_{riblef}) \\
& + C_{Y_{13}}(\alpha, \beta, M, \delta_{riblef}, \delta_{roblef}) - C_{Y_{14}}(\alpha, M, \delta_{rssd}, \delta_{rel}) - C_{Y_{15}}(\alpha, \beta, \delta_{ramt}) \\
& - C_{Y_{16}}(\alpha, \beta, \delta_{rssd})
\end{aligned} \tag{2.2}$$

$$\begin{aligned}
C_Z = {} & C_{Z_1}(\alpha, M) + C_{Z_2}(\alpha, \beta, M) + C_{Z_3}(\alpha, \beta, M, \delta_{liblef}) \\
& + C_{Z_4}(\alpha, \beta, M, \delta_{liblef}, \delta_{loblef}) + C_{Z_5}(\alpha, M, \delta_{lssd}, \delta_{lel}) + C_{Z_6}(\alpha, M, \delta_{lssd}, \delta_{rssd}, \delta_{pf}) \\
& + C_{Z_7}(\alpha, \beta, \delta_{lamt}) + \Delta C_{Z_8}(\alpha, \delta_{lamt}, \delta_{lel}) + \Delta C_{Z_9}(\alpha, \delta_{loblef}, \delta_{lamt}) \\
& + \Delta C_{Z_{10}}(\alpha, \delta_{ramt}, \delta_{rel}) + \Delta C_{Z_{11}}(\alpha, \delta_{roblef}, \delta_{ramt}) + C_{Z_{12}}(\alpha, \beta, \delta_{lssd}) \\
& + C_{Z_{13}}(\alpha, \beta, \delta_{riblef}) + C_{Z_{14}}(\alpha, \beta, M, \delta_{riblef}, \delta_{roblef}) + C_{Z_{15}}(\alpha, M, \delta_{rssd}, \delta_{rel}) \\
& + C_{Z_{16}}(\alpha, \beta, \delta_{ramt}) + C_{Z_{17}}(\alpha, \beta, \delta_{rssd}) + \frac{\bar{c} \cdot q}{2V} C_{Z_{18}}(\alpha, M)
\end{aligned} \tag{2.3}$$

$$\begin{aligned}C_L = {} & C_{L_1}(\alpha,M) + C_{L_2}(\alpha,\beta,M) - C_{L_3}(\alpha,\beta,\delta_{liblef}) \\ & - C_{L_4}(\alpha,\beta,M,\delta_{liblef},\delta_{loblef}) + C_{L_5}(\alpha,M,\delta_{lel},\delta_{lssd}) + C_{L_6}(\alpha,M,\delta_{lel},\delta_{lamt}) \\ & - C_{L_7}(\alpha,M,\delta_{lssd}) + \Delta C_{L_8}(\alpha,\delta_{lamt},\delta_{lel}) + \Delta C_{L_9}(\alpha,\delta_{loblef},\delta_{lamt}) \\ & - \Delta C_{L_{10}}(\alpha,\delta_{ramt},\delta_{rel}) - \Delta C_{L_{11}}(\alpha,\delta_{roblef},\delta_{ramt}) + C_{L_{12}}(\alpha,\beta,\delta_{ribref}) \\ & + C_{L_{13}}(\alpha,\beta,\delta_{riblef},\delta_{robref}) - C_{L_{14}}(\alpha,\beta,M,\delta_{rssd},\delta_{rel}) - C_{L_{15}}(\alpha,M,\delta_{ramt}) \\ & - C_{L_{16}}(\alpha,\beta,\delta_{rssd}) + \frac{b\cdot p}{2V}C_{L_{17}}(\alpha,M) + \frac{b\cdot r}{2V}C_{L_{18}}(\alpha,M)\end{aligned} \tag{2.4}$$

$$\begin{aligned}C_M = {} & C_{M_1}(\alpha,M) + C_{M_2}(\alpha,\beta,M) + C_{M_3}(\alpha,\beta,\delta_{liblef}) \\ & + C_{M_4}(\alpha,\beta,M,\delta_{liblef},\delta_{loblef}) + C_{M_5}(\alpha,M,\delta_{lel},\delta_{lssd}) + C_{M_6}(\alpha,M,\delta_{lssd},\delta_{rssd},\delta_{pf}) \\ & + C_{M_7}(\alpha,\beta,\delta_{lamt}) + \Delta C_{M_8}(\alpha,\delta_{lamt},\delta_{lel}) + \Delta C_{M_9}(\alpha,\delta_{loblef},\delta_{lamt}) \\ & + \Delta C_{M_{10}}(\alpha,\delta_{ramt},\delta_{rel}) + \Delta C_{M_{11}}(\alpha,\delta_{roblef},\delta_{ramt}) + C_{M_{12}}(\alpha,\beta,\delta_{lssd}) \\ & + C_{M_{13}}(\alpha,\beta,\delta_{riblef}) + C_{M_{14}}(\alpha,\beta,\delta_{riblef},\delta_{robref}) + C_{M_{15}}(\alpha,\beta,M,\delta_{rssd},\delta_{rel}) \\ & + C_{M_{16}}(\alpha,M,\delta_{ramt}) + C_{M_{17}}(\alpha,\beta,\delta_{rssd}) + \frac{\bar{c}\cdot q}{2V}C_{M_{18}}(\alpha,M)\end{aligned} \tag{2.5}$$

$$\begin{aligned}C_N = {} & C_{N_1}(\alpha,M) + C_{N_2}(\alpha,\beta,M) - C_{N_3}(\alpha,\beta,M,\delta_{liblef}) - C_{N_4}(\alpha,\beta,M,\delta_{liblef},\delta_{loblef}) \\ & + C_{N_5}(\alpha,M,\delta_{lssd},\delta_{lel}) + C_{N_6}(\alpha,M,\delta_{lel},\delta_{lamt}) + C_{N_7}(\alpha,\beta,\delta_{lssd}) + \Delta C_{N_8}(\alpha,\delta_{lamt},\delta_{lel}) \\ & + \Delta C_{N_9}(\alpha,\delta_{loblef},\delta_{lamt}) - \Delta C_{N_{10}}(\alpha,\delta_{ramt},\delta_{rel}) - \Delta C_{N_{11}}(\alpha,\delta_{roblef},\delta_{ramt}) \\ & + C_{N_{12}}(\alpha,\beta,\delta_{riblef}) + C_{N_{13}}(\alpha,\beta,M,\delta_{riblef},\delta_{roblef}) - C_{N_{14}}(\alpha,M,\delta_{rssd},\delta_{rel}) \\ & - C_{N_{15}}(\alpha,\beta,\delta_{ramt}) - C_{N_{16}}(\alpha,\beta,\delta_{rssd}) + \frac{b\cdot p}{2V}C_{N_{17}}(\alpha,M) + \frac{b\cdot r}{2V}C_{N_{18}}(\alpha,M)\end{aligned} \tag{2.6}$$

The force and moment coefficients are translated from the reference center of gravity to the actual location of the c.g. for the selected mass properties, after which they are dimensionlised and the effects of pitch an yaw TV are added to the aerodynamic moments. Since the model does not come with an engine model or actuation models, the actuation can be represented by the transfer function in equation 2.7 for leading edge actuators and the transfer function in equation 2.8 for other actuators and the engine.

$$\frac{(18)(100)}{(s+18)(s+100)} \tag{2.7}$$

$$\frac{(40)(100)}{(s+40)(s+100)} \tag{2.8}$$

The thrust (in x-, y- and z-direction) and the effectors (eleven deflections from the control surfaces and two from the TV) serve as input for the ICE aircraft model. The outputs are the velocity in inertial axis V_e, the position in inertial axis X_e, the body Euler angles ϕ, θ and ψ, the velocities in the body axis u, v and w, the rotation rates in the body axis p, q and r, the body rotational acceleration in the body axis $\dot{p}$, $\dot{q}$ and $\dot{r}$ and the accelerations in the body axis a_x, a_y and a_z. Further outputs of the model are the dynamic pressure $\bar{q}$, the airspeed V, the Mach number M, the angle of attack α and the sideslip angle β. For the computation of the aerodynamic coefficients, look-up tables are used from experimental data and results outside of the range are extrapolated linearly for low AOA and clipped for high AOA. Linear interpolation should be performed for α, β and M and cubic spline interpolation everywhere else. Note that this was not fully implemented in the model provided. Not all aerodynamic coefficients are defined on the same range of α, β and M. For example C_{X_1} is defined on $[-5°, 90°]$ while C_{X_3} is defined on $[-2.5°, 45°]$ AOA. The deflection limits and the rate limits of the actuators and TV are given in table 2.2.

Control effector	Deflection range limit (deg)	Rate Limit (deg/sec)
Inboard DLEF	0-40	40
Outboard DLEF	±40	40
Elevons	±30	150
Pitch flaps	±30	50
AMT	0-60	150
SSD	0-60	150
TV	±15	60

Table 2.2: Deflection and rate limits of the effectors and TV [8, 19]

In [18], the ICE model has been extended by 3D projection of the thrust vector T of the TV model that was provided. The moment arm of the thrust force is $d_n = 18.75$ ft, the moment τ_T of the thrust force is,

$$\tau_T = -T \cdot d_n \begin{bmatrix} 0 \\ \sin(\delta_{ptv}) \\ \cos(\delta_{ptv}) \tan(\delta_{ytv}) \end{bmatrix} \tag{2.9}$$

and the thrust in 3D is,

$$T = T \begin{bmatrix} \cos(\delta_{ptv}) / \cos(\delta_{ytv}) \\ \cos(\delta_{ptv}) \tan(\delta_{ytv}) \\ \sin(\delta_{ptv}) \end{bmatrix} \tag{2.10}$$

where δ_{ptv} and δ_{ytv} are the deflection angles in pitch and yaw direction of the TV respectively.

3

Incremental Nonlinear Control Allocation

Instead of updating the aerodynamic coefficients, one can take an incremental approach for which only the Jacobian of the control effectiveness matrix has to be updated each time step. The INCA approach was first used by Ismael Matamoros in his thesis named Nonlinear Control Allocation for a High-performance Tailless Aircraft with Innovative Control Effectors. In this thesis the benefits of using INCA over aerodynamic model methods becomes clear; it is able to perform real-time, it is robust against aerodynamic model mismatch, negative effects of the actuator dynamics are mitigated and it computationally less complex. The INCA does rely on angular acceleration feedback and actuator position feedback alongside a Jacobian control effectiveness model.

In this chapter the methods used to derive the INCA control scheme are discussed. Transforming the Nonlinear control problem in incremental form is discussed in section 3.1 and the Control Allocation problem in section 3.2. In section 3.3 the incremental flight control system design of INCA is discussed.

3.1. Nonlinear Control in Incremental Form

Consider the aircraft dynamics expressed in the general form,

$$\dot{x}(t) = f(x) + g(x)\tau \tag{3.1}$$

where x is the state vector and τ represents the aerodynamic inputs, in this case the aerodynamic moments in the body frame. The aerodynamic moments can be separated into a state-dependent and an input-dependent part,

$$\tau = \tau_a + \tau_\delta \tag{3.2}$$

where τ_a contains the aerodynamic moments generated by the airframe and τ_δ by the control effector model, providing the control-induced moments produced by the actuators. The control effector model can be expressed as the nonlinear mapping,

$$\tau_\delta = \Phi(x, \delta) \tag{3.3}$$

Thus the system dynamics can be rewritten as,

$$\dot{x} = [f(x) + g(x)\tau_a] + g(x)\Phi(x,\delta) = F(x) + g(x)\Phi(x,\delta) \tag{3.4}$$

where the term $F(x)$ contains the moments not produced by the control effectors. In a discrete-time scheme, this equation can be linearized locally at every time step around the current state x_0 and the actuator positions δ_0 as a first-order Taylor expansion:

$$\dot{x} \approx \dot{x}_0 + \frac{\partial}{\partial x}\left[F(x) + g(x)\Phi(x,\delta)\right]\bigg|_{\substack{\delta=\delta_0\\ x=x_0}} (x - x_0) + \frac{\partial}{\partial \delta}\left[F(x) + g(x)\Phi(x,\delta)\right]\bigg|_{\substack{\delta=\delta_0\\ x=x_0}} (\delta - \delta_0) \tag{3.5}$$

The time scale separation principle states that for systems with the derivatives of the states with significantly faster dynamics than the states themselves the change in state $(x - x_0)$ is small enough to be neglected at a high sampling frequency. Applying the time scale separation and setting the virtual control input $\nu(x) = \dot{x}$ the simplified linearized system dynamics are,

$$\nu(x) = \dot{x} \approx \dot{x}_0 + g(x_0)\frac{\partial \Phi(x_0, \delta_0)}{\partial \delta}\Delta\delta \tag{3.6}$$

where $g(x_0)\partial(x_0, \delta_0)/\partial\delta$ is a control effectiveness Jacobian function that can be nonlinear in δ and include interactions between input variables. $\dot{x}_0$ is the time derivative of the state vector, which corresponds to the body angular accelerations. This can be obtained from direct measurement or state estimation methods.

The incremental nonlinear dynamic inversion becomes,

$$\Delta\delta_c = \left[\frac{\partial \Phi(x_0, \delta_0)}{\partial \delta}\right]^{-1} g(x)^{-1}[\nu(x) - \dot{x}_0] \tag{3.7}$$

This incremental control law provides the increments of the actuator position with respect to the current position vector δ_0, such that the new actuator position can be calculated as follow,

$$\delta_c = \delta_0 + \Delta\delta_c \tag{3.8}$$

In over-actuated systems the Jacobian $\partial(x_0, \delta_0)/\partial\delta$ is a non-square $p \times n$ matrix and therefore cannot be inverted to implement the incremental control law. However a control allocation scheme can be implemented by reformulating the control allocation problem in incremental form.

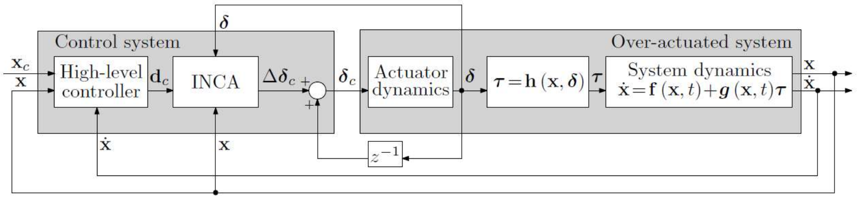

Figure 3.1: Incremental nonlinear control allocation scheme for over-actuated systems [18]

3.2. Control Allocation in Incremental Form

The INCA problem is formulated as: given the current state x_0, the control control effector position δ_0, acceleration measurements $\dot{x}_0$ and a pseudo-control input command $d_c = g(x)^{-1}[v(x) - \dot{x}_0]$, determine an increment in the control input vector $\Delta\delta$ such that,

$$\frac{\partial\Phi(x,\delta)}{\partial\delta} = d_c \tag{3.9}$$

subject to $\underline{\Delta\delta} \le \Delta\delta \le \bar{\Delta\delta}$, which are the most restrictive upper and lower bounds of the local position and rate constraints of the actuators, translated into local incremental constraints. An overview of this proposed control scheme is shown in figure 3.1.

The advantage of using INCA is that it is linear in actuator positions and therefore can be solved with simple and efficient linear methods such as Redistributed Weighted Pseudo-Inverse (RWPI) or QP and that using this solution there is no need for aerodynamic model identification. However another problem is introduced as the control effectiveness matrix is based on the wind tunnel data of the fully functioning model of the ICE aircraft. If one or more effectors are failing, the control effectiveness model does not correspond to the reality and has to be updated. Keeping in mind that the ICE model is robust against inaccuracies of the control effectiveness matrix. So one can also investigate how robust the INCA method is.

3.3. Incremental Flight Control System Design

The flight control system for incremental nonlinear control allocation method proposed by Ismael Matamoros is discussed in this section. First the Jacobian model based on multivariate simplex splines of the control effectiveness matrix is discussed in subsection 3.3.1. The innermost control loop design is discussed in subsection 3.3.2. To be able to solve the control allocation problem an active set-based quadratic programming algorithm is used, which is discussed in subsection 3.3.3. Finally, to prevent actuator saturation a technique called PCH has been implemented in the control system design and is discussed in subsection 3.3.4.

3.3.1. Multivariate Simplex Spline-based Jacobian Model

The Jacobian model $\frac{\partial\Phi(x,\delta)}{\partial\delta}$ that was used in [18] is based on a mutlivariate B-spline aerodynamic model of the ICE aircraft identified from the aerodynamic database described in chapter 2. The spline model was developed in [26] using the linear regression techniques presented in [6]. This spline model consists of 108 spline functions, corresponding to every dimensionless aerodynamic moment and force coefficient.

The directional derivatives of every coefficient $C^s_{i_x}$ in the aerodynamic model, where $i = \{X, Y, Z, L, M, N\}$ and x is the position of the derivative in the equation, to determine the Jacobian of the control effectiveness matrix can be calculated with a real-time efficiency in the order of 10^4 Jacobian calculation per second. This is done using a method for model reduction of parabolic partial differential equations presented in [23]. As can be derived from chapter 2 there are 107 spline models needed for every coefficient, each of these models will be partially differentiated by each control effector δ, which are 13 in total . Using this the control effectiveness Jacobian matrix is defined as,

$$\frac{\partial\Phi(x,\delta)}{\partial\delta} = \begin{bmatrix} \sum_{j=1}^{18} \frac{\partial C^s_{l_j}(x,\delta)}{\partial\delta_1} & \sum_{j=1}^{18} \frac{\partial C^s_{l_j}(x,\delta)}{\partial\delta_2} & \cdots & \sum_{j=1}^{18} \frac{\partial C^s_{l_j}(x,\delta)}{\partial\delta_13} \\ \sum_{j=1}^{18} \frac{\partial C^s_{m_j}(x,\delta)}{\partial\delta_1} & \sum_{j=1}^{18} \frac{\partial C^s_{m_j}(x,\delta)}{\partial\delta_2} & \cdots & \sum_{j=1}^{18} \frac{\partial C^s_{m_j}(x,\delta)}{\partial\delta_13} \\ \sum_{j=1}^{18} \frac{\partial C^s_{n_j}(x,\delta)}{\partial\delta_1} & \sum_{j=1}^{18} \frac{\partial C^s_{n_j}(x,\delta)}{\partial\delta_2} & \cdots & \sum_{j=1}^{18} \frac{\partial C^s_{n_j}(x,\delta)}{\partial\delta_13} \end{bmatrix} \tag{3.10}$$

It was decided in his thesis to have 0-order continuity to represent the worst-case scenario, as well as the least computational complex solution.

For TV the Jacobian matrix of τ_T is,

$$\frac{\partial\tau_T(\delta_{ptv},\delta_{ytv})}{\partial\delta_{tv}} = T\cdot d_n \begin{bmatrix} 0 & 0 \\ -\cos(\delta_{ptv}) & 0 \\ \sin(\delta_{ptv}\tan(\delta_{ytv}) & -\cos(\delta_{ptv})/\cos^2(\delta_{ytv}) \end{bmatrix} \tag{3.11}$$

The thrust vector arm in incremental is subject to a circular constraint, such that the new delfection increment has to be computed as,

$$\Delta\delta'_{tv} = \frac{\delta_{tv_{max}}}{\|\delta_{tv_0} + \Delta\delta_{tv}\|}(\delta_{tv_0} + \Delta\delta_{tv}) - \delta_{tv_0} \tag{3.12}$$

3.3.2. Angular Rate Control Loop

The innerloop of the control system used in INCA is a body angular rate control loop. Consider the aircraft rotational dynamics, where τ_e is now replaced by the nonlinear control effector model $\Phi(x,\delta)$,

$$\dot{\omega} = J^{-1}(\tau - \omega \times J\omega) = J^{-1}\Phi(x,\delta) + J^{-1}(\tau_a - \omega \times J\omega) \tag{3.13}$$

For a given time step, the incremental form of the rotational dynamics as a first-order Taylor expansion at the operation point (x_0,δ_0) is,

$$\dot{\omega} = \dot{\omega}_0 + \frac{\partial}{\partial \omega}\left[J^{-1}\Phi(x,\delta) + J^{-1}(\tau_a - \omega \times J\omega)\right]\Bigg|_{\substack{\delta=\delta_0\\ \theta=\theta_0}}(\omega - \omega_0) + \frac{\partial}{\partial \delta}\left[J^{-1}\Phi(x,\delta) + J^{-1}(\tau_a - \omega \times J\omega)\right]\Bigg|_{\substack{\delta=\delta_0\\ \theta=\theta_0}}(\delta - \delta_0) \tag{3.14}$$

where the angular accelerations at the current step $\dot{\omega}_0$ can be obtained from angular accelerometers, signal processing or acceleration estimation methods.

Equation 3.13 can be simplified as due to the previously discussed time scale separation principle the second term of the right-hand side, i.e. the changes in angular acceleration due to changes in angular rates, is negligible for high sampling rates in comparison to the input-dependent term. Thus equation 3.13 becomes,

$$\dot{\omega} = \dot{\omega}_0 + J^{-1}\frac{\partial}{\partial \delta}\Phi(x_0,\delta_0)\Delta\delta \tag{3.15}$$

Setting the angular acceleration as a virtual control input $v_\omega(x) = \dot{\omega}$ and solving for $\Phi(x_0,\delta_0)\Delta\delta$, the INCA formulation in equation 3.9 becomes for the body angular rate control loop problem,

$$\Phi(x_0,\delta_0)\Delta\delta = I\left[v_\omega(x) - \dot{\omega}_0\right] = \Delta\tau_c \tag{3.16}$$

where the pseudo-control input d_c corresponds to the required increments of control-induced moments $\Delta\tau_c$.

3.3.3. Active set-based Quadratic Programming

The control allocation problem can be formulated as an l_2-norm cost function of the multi-objective constrained optimization problem,

$$\begin{aligned} \min_u J =& W_d \|Bu - d_c\|_2 + \epsilon W_u \|u - u_p\|_2 \\ &\text{subject to} \quad \underline{u} \leq u \leq \bar{u} \end{aligned} \tag{3.17}$$

where W_d and W_u are non-singular weighting matrices for the minimization of the allocation error and the minimization of the control effort respectively. ϵ is a sufficiently small scalar to prioritize the minimization of the allocation error $(Bu - d_c)$ over the secondary objective of minimizing $(u - u_p)$.

For solving the control allocation problem with INCA an active set-based QP solver found to be most suitable as the active-set algorithm converges exactly to the optimal solution in a finite number of steps and is computationally efficient for small and medium size CA problems. [20] The active-set algorithm for QP was first introduced by [10]. To use the algorithm presented in [10] the cost function defined in equation 3.12 is reformulated,

$$\begin{gathered}\min_{u}\left\| \begin{bmatrix} W_u B \\ \epsilon W_u \end{bmatrix} u - \begin{bmatrix} W_d d_c \\ \epsilon W_u u_p \end{bmatrix} \right\|_2 \\ \text{subject to} \quad Bu = d_c, \quad Cu \geq U \end{gathered} \tag{3.18}$$

where $C = [I - I]^T$ and $U = \left[\underline{u}\bar{u}\right]$. The active set algorithm solves a sequence of equality constrained problems, where in every iteration some inequality constraints are regarded as equality constraints and form a working set W, whereas the remaining inequality constraints are disregarded. The working set W at the optimum is known as the active set of the solution [10].

3.3.4. Pseudo-Control Hedging

To prevent actuator saturation a method called PCH proposed in [12] was used for the INCA algorithm to shape the virtual control command $v_\omega(x)$. PCH was already successfully implemented succesfully in [13, 14].

The reshaping of the reference signal is done by subtracting the difference between the commanded $v_\omega(x)$ and the virtual control achieved, estimated with the actuator positions δ_0 as $\hat{v}_\omega(x) = f(x_0, \delta_0)$, where $f(x, \delta)$ is the virtual control law. δ_0 is obtained through a feedback loop. The PCH is computed as,

$$v_h(x) = v_\omega(x) - \hat{v}_\omega(x) \tag{3.19}$$

The hedge signal $v_h(x)$ is fed back into a first-order reference model as a compensation signal. The reference model $v_{rm}(x)$ is,

$$v_{rm}(x) = K_{rm}(\omega_c - \omega_{rm}) \tag{3.20}$$

with K_{rm} a diagonal matrix. The hedge reference signal is the state vector of the reference model,

$$\omega_{rm} = \frac{1}{s}(v_{rm}(x) - v_h(x)) \tag{3.21}$$

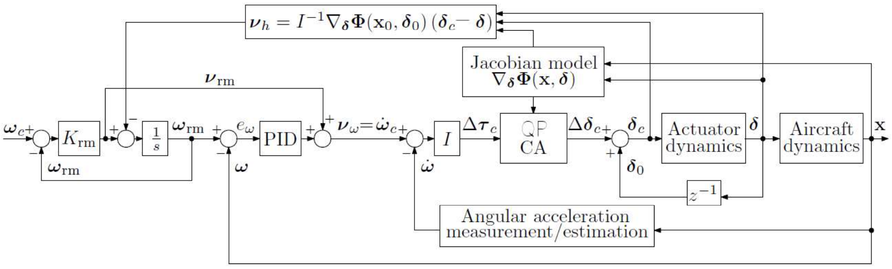

Figure 3.2: Schematic of the INCA-based angular rate control system using PCH and QP [18]

When no saturation occurs, $\upsilon_h(x) = 0$ and the reference model behaves as a low-pass filter of bandwidth K_{rm}, for the i-th component of ω_{rm}. In case of actuator saturation the hedge signal $\upsilon_h(x)$ is used to reshape the reference input and avoid unfeasible commands. The reference model $\upsilon_{rm}(x)$ corresponds to the first-order derivatives of the commanded variables, which can be used a a feed-forward term added to $\upsilon_\omega(x)$ to improve tracking performance [22].

The virtual control law is given by,

$$\upsilon_\omega(x) = \dot\omega_0 + I^{-1}\frac{\partial\Phi(x_0,\delta_0)}{\partial\delta}(\delta - \delta_0) \tag{3.22}$$

hence the PCH is defined as,

$$\upsilon_h(x) = \left[\dot\omega_0 + I^{-1}\frac{\partial\Phi(x_0,\delta_0)}{\partial\delta}(\delta_c - \delta_0)\right] - \left[\dot\omega_0 + I^{-1}\frac{\partial\Phi(x_0,\delta_0)}{\partial\delta}(\delta - \delta_0)\right] \tag{3.23}$$

$$\upsilon_h(x) = I^{-1}\frac{\partial\Phi(x_0,\delta_0)}{\partial\delta}(\delta_c - \delta) \tag{3.24}$$

In figure 3.2 an overview of the PCH used in INCA for an angular rate control system is shown.

4

Fault-tolerant Control

FTC systems are control systems that are able to accommodate for system component failures. They are capable of maintaining overall system stability and acceptable performance during such failures. FTC systems are mostly a combination of redundancy in the components and automation in the software that monitors the system behaviour. Faults are detected by such control system and appropriate actions are taken to mitigate the risks of critical failures. In the area of FTC, one can distinguish between Active Fault Tolerant Control (AFTC) and Passive Fault Tolerant Control (PFTC) methods. The main focus of this work will be on AFTC, mainly because PFTC provide limited fault-tolerant capabilities especially for increasing fault scenarios as indicated in [11] and [27]. A historical overview of AFTC (or Reconfigurable Flight Contol System (RFCS)) methods is given in [27].

AFTC approaches rely mostly on Fault Detection and Isolation (FDI) or Fault Detection and Diagnosis (FDD) schemes, i.e. fault detection, fault isolation and fault estimation. These schemes are either logic-based or based on the feedback of the estimator. AFTC approaches can be split into nonlinear and linear methods. Most control applications are nonlinear by nature but linear methods can be applied around the equilibrium points of the system. Common linear methods that are used are gain scheduling, MM and SMC. Purely nonlinear approaches are feedback linearization, NDI, backstepping, NN, nonlinear regulator and lyapunov methods. Compared to their linear counterpart, NDI and backstepping use the well-known equations of motions of the aircraft which are valid throughout the flight envelope, while gain scheduling and LPV schemes are only designed for specific parts of the flight envelope. Along with these approaches one must select an appropriate CA algorithm to supplement these methods especially when the aircraft is over-actuated. CA algorithms that are commonly used are the pseudo-reverse, modified pseudo-reverse, direct allocation, constrained optimization method, fixed point method or a combination of the aforementioned methods.

In this section, the fault scenarios used for ICE are discussed followed by the proposed FTC system design. An overview of the framework which incorporates the FTC with other components described previously along with testing modules is shown in figure 4.1.

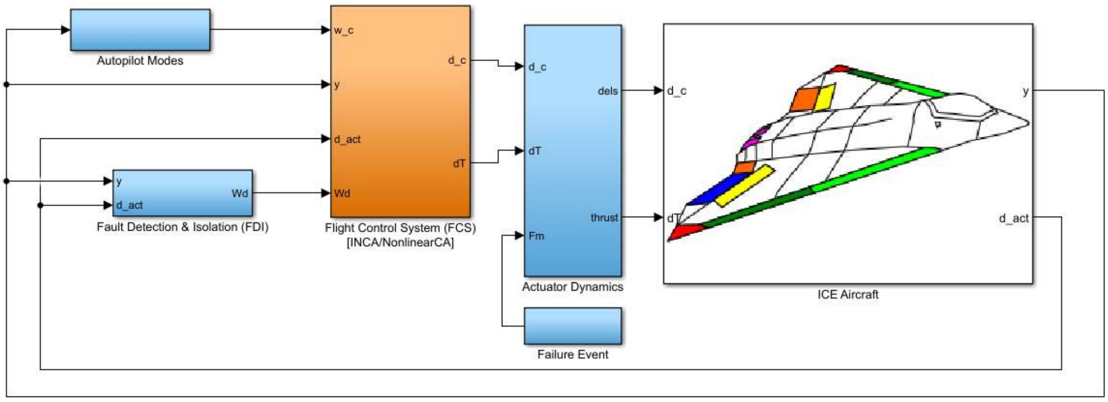

Figure 4.1: Schematic of the FTC system design including the ICE, INCA, FDI, failure event and autopilot modules. The blue coloured subsystems were added in this work

4.1. Effector failures

As mentioned in the introduction, AFTC method is used in this work instead of PFTC. AFTC approaches rely mostly on FDI or FDD schemes. Logically, it can be reasoned that the CA scheme for over-actuated aircraft is an AFTC system by itself and hence should not require a FDI scheme. The reasoning behind this hypothesis is as follows: The ICE aircraft model is inherently a nonlinear system and to be able to control this model in case of effector failures, a nonlinear fault tolerant control design is best suited. Along with these approaches one must select an appropriate CA algorithm to supplement these methods especially when the aircraft is over-actuated. This has been done successfully for ICE using INCA as explained in Section 3. An inherent property of the control allocation method mitigates the risk of loss-of-control due to a single effector failure, i.e. not a single actuator of the ICE aircraft is solely responsible for the generation of one of the aerodynamic moments. Thus, the INCA flight control scheme can be considered to be an AFTC system by itself.

However knowledge about the failure scenario, which effector and the nature of the fault, is necessary to determine the correct effectiveness matrix B in equation 3.17 used for solving INCA. An Erroneous B matrix will result in control inputs allocated to an effector which does not or can only partly generate the necessary change in moment. Therefore, an FDI module has been added to the current INCA flight control scheme as shown in figure 4.1. Due to the unavailability of a working FDI module, this work investigates the performance of the ICE aircraft model against critical effector failures using the AFTC system under the assumption of perfect fault detection.

In general, there are different types of effector failures such as lock-in-place, hard-over, free floating, loss of effectiveness, missing control effector, loss of hydraulic power, etc. The FDI system is designed to detect only three effector faults due to the scope of this work and these faults are described below:

- *Lock-in-place* failure is a type of failure of the control effector when the effector freezes in a certain position and does not respond to subsequent commands. Such a failure introduces both constant and state-dependent disturbances into the overall closed-loop systems, whereby control reconfiguration is necessary for maintaining the stability and robustness of the system as shown in [1].
- *Hard-over* is a special case of freezing when the effector locks at its saturation position limit.
- *Loss of effectiveness* can occur due to (minor) structural damage loss. This means a slow or sudden decrease in the control effector gain, such that the same control signal results in a smaller control deflection compared to nominal airframe condition. One can try to accommodate the fault by increasing the control input gain, however this will increase the possibility of saturation.

4.2. Control law update for FTC design

AFTC of the model and/or flight control scheme has been successfully implemented in nonlinear flight scenarios. One such method involves deriving aerodynamic models of the possible fault scenarios beforehand while others try to update the aerodynamic model parameters in real-time. The former method requires more extensive wind-tunnel or prototype flight testing, while the latter requires extensive computational power for increased performance with nonlinear and over-actuated aircraft such as the ICE aircraft model. In this work, a third method is used where the aerodynamic model does not have to be updated but the flight control system itself is changed to increase fault tolerance. This can be achieved either by,

- Limiting effector deflection range and rate limits specified in table 2.2 or

- Adjusting the weight W_δ assigned to the control effector for each effector as defined in equation 3.17

Limiting effector deflection and rate limits can only be done with prior knowledge about the effect this limitation has on the operational range of the aircraft, while adjusting the weights of W_δ can be applied immediately after determining the degradation of the control effectiveness of the effector using FDI. In this work, the second method has been implemented and tested whereas the first method is recommended for future research.

In [18], the preferred deflection in each time step and the weight W_δ is used to determine the deflection rates and absolute positions of the effectors. Due to the change in weights proposed in this work, the preferred deflection also has to be updated. First, we re-introduce the preferred deflection defined in [18]. In discrete-time, the position limits over a time step Δt is defined with respect to the rate limit as

$$\begin{aligned} \Delta\delta^r_{max} &= \dot{\delta}_{max}\Delta t \\ \Delta\delta^r_{min} &= \dot{\delta}_{max}\Delta t \end{aligned} \tag{4.1}$$

Furthermore, the absolute deflection limit is expressed in local constraints in the time step Δt as

$$\begin{aligned} \Delta\delta^p_{max} &= \delta_{max} - \delta_0 \\ \Delta\delta^p_{min} &= \delta_{min} - \delta_0 \end{aligned} \tag{4.2}$$

The minimum and maximum deflection limit in time step Δt is chosen between the constraints due to the rate limits and those due to the absolute position as

$$\begin{aligned} \overline{\Delta\delta} &= \min\left(\Delta\delta^r_{max}, \Delta\delta^p_{max}\right) \\ \underline{\Delta\delta} &= \max\left(\Delta\delta^r_{min}, \Delta\delta^p_{min}\right) \end{aligned} \tag{4.3}$$

In [18], it has been observed that if the preferred position change in each time step is set to $\Delta\delta_p = 0$, complementary actuators diverge to asymmetric nonzero deflections while still producing a resulting moment of zero. To avoid this situation, the control effectors must attain their preferred absolute positions δ_p. Thus, the preferred incremental deflection at each time step is defined as

$$\Delta\delta_p = \min\Big(|\delta_p - \delta_0|, |\overline{\Delta\delta}|, |\underline{\Delta\delta}|\Big) \cdot \mathrm{sign}(\delta_p - \delta_0) \tag{4.4}$$

During lock-in-place and hard-over failures, the preferred absolute deflection cannot be attained anymore. Therefore, it is best to assign the failure position as preferred deflection position such that $\Delta\delta_p = 0$. However, this assignment alone is not sufficient in case all effectors are in their preferred position and a change in moment is required because the failed effector can still be chosen by the algorithm to provide the necessary change in moment. Therefore, the weight matrix W_δ which is responsible for assigning importance to certain effectors over others also needs to be updated. In straight flight, the weights in W_δ are set to 1 except for the SSDs. For SSDs, the weight is chosen as a function of AoA. This is because at low AoA, the control effectiveness of downstream effectors is negatively affected while at high AoA, the control effectiveness of trailing-edge devices is recovered by SSDs redirecting the airflow towards the upper wing skin. The W_δ for SSDs is defined in [18] as,

$$W_{\delta SSD}(\alpha) = [-0.25 + .35\exp(1.6\alpha)]^{-1} \tag{4.5}$$

At $\alpha = 0$, $W_{\delta SSD}$ is 10 and is 1 at $\alpha \approx 45$ deg.

In case of stuck-in-place or hard-over failure the effector is assigned a W_δ of 100. For partial loss of effectiveness, an exponential formula can be applied to assign W_δ. In normal conditions $W_\delta = 1$ and in the case where there is a total loss of effectiveness $W_\delta = 100$. The assumption is that a linear relationship is not beneficial because at a small loss of effectiveness the effector would still be functional. Given the effectiveness is denoted by δ_{eff} (in percentage), then the weight for the failing effector W_{δ_f} is defined as,

$$W_{\delta_f} = 0.955 + 0.005 \cdot \exp(0.1 \cdot (100 - \delta_{eff})) \tag{4.6}$$

At $\delta_{eff} = 100\%$, $W_\delta = 1$, at 50%, $W_{\delta_f} = 1.7371$ and at 10%, $W_{\delta_f} = 41.51$. Thus, for a stuck-in-place effector not only the preference position δ_p is adjusted to its failure position but also a penalty weight W_{δ_f} of 100 is assigned. At the FDI module the weights and preference deflection positions are determined based on the detected failures.

The flight control scheme is extended by allowing effector faults to occur using a switch function within the actuator dynamics block (see figure 4.1) to introduce the effector failure at failure time t_{fail}. Inside the switch function, the angle δ_{fail} of the effector can be set and is used to investigate stuck or hard-over failure cases set to specific angles. The FDI for the effector failures is assumed to have a perfect detection rate within 1 second after failure time t_{fail}.

5

Autopilot design

In the last couple of years autopilot are used more widely in the aircraft industry mostly to reduce pilot work load and to have more fuel efficient flight trajectories. An important part of this research is to design and integrate the autopilots as the outer-loop control schemes of INCA. The output of the autopilots designed in this chapter serve as the input to the INCA inner-loop control schema: the rotational rate vector ω_c.

The flight trajectories for testing are defined within the autopilot control module in figure 4.1. All trajectories require a predefined set of inputs for lateral and longitudinal flight control. The autopilots for lateral and longitudinal control is discussed in this section. A non trivial task within this research is tuning the gains K_i used in the chosen inner and outer-loops of the FCS. Both lateral and longitudinal autopilots, an auto-throttle controller and a sideslip hold mode are used simultaneously. The autopilot modes are listed in table 5.1.

Lateral	**Longitudinal**
Altitude Hold	Heading Hold
Glideslope Intercept	Localizer Intercept
Flight Path Angle Hold	Roll Angle Hold

Table 5.1: List of autopilot modes

These autopilot modes are the outer-loops for the flight scenarios while the inner-loop is given by using the INCA methods including PCH control as shown in figure 3.1. The control schemes and the input and outputs for the six autopilots are:

1. The altitude hold mode is shown in figure 5.1. The inputs are the reference altitude h_{ref}, the measured altitude h_m, the pitch angle θ and the angle of attack α. The output is the commanded pitch rate $\dot{\theta}$. The altitude hold mode should be used only to keep the current altitude, not to initiate flight level changes. The gain K_h is used to couple the altitude error to a preferred change in flight path angle. The flight path angle γ is obtained from $\gamma_m = \theta_m - \alpha_m$ and is translated to a commanded pitch rate using PID. The commanded pitch rate $\dot{\theta}$ serves as the input to the inner-loop (see figure 3.2).

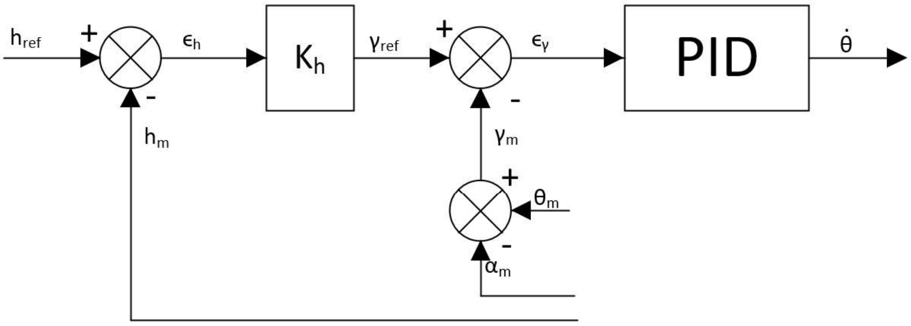

Figure 5.1: Lateral Autopilot: Altitude Hold Mode control scheme

2. The flight path angle hold mode is shown in the latter part of altitude hold mode control system in figure 5.1. The input is the reference flight path γ_{ref} and the measured flight path $\gamma_m = \theta_m - \alpha_m$. The output is the commanded pitch rate $\dot{\theta}$.

3. The glideslope intercept control scheme is shown in figure 5.2. An overview of the glideslope is shown in figure 5.3. The glideslope reference angle Γ is zero, when the glideslope error e_Γ is zero that means the aircraft follows the glideslope with no deviation d. The glideslope path is the path defined by an angle of 3 degrees from the ground up. The distance of the aircraft to this path is deviation d and the absolute range between the aircraft and the localizer is Slant Range R. The deviation angle Γ is then,

$$\Gamma_m = \frac{1}{s} \cdot \frac{V_0(\gamma + 3)}{R} \cdot \frac{\pi}{180} \tag{5.1}$$

   The glideslope deviation angle error is translated to a reference pitch angle using a PID coupler. The output of the glideslope intercept is $\dot{\theta}$.

4. The heading hold mode is shown in figure 5.4. The input is the reference heading ψ_{ref}, the measured heading ψ_m and the roll angle ϕ_m. The output is the commanded roll rate $\dot{\phi}$. Roll angles are allowed between -85 and 85 degrees, heading reference angle between 0 and 360 degrees.

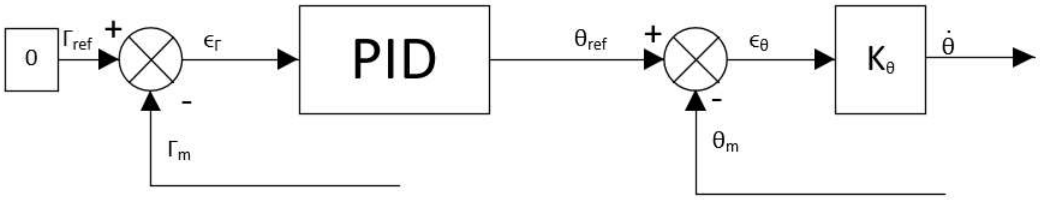

Figure 5.2: Lateral Autopilot: Glideslope Intercept control scheme

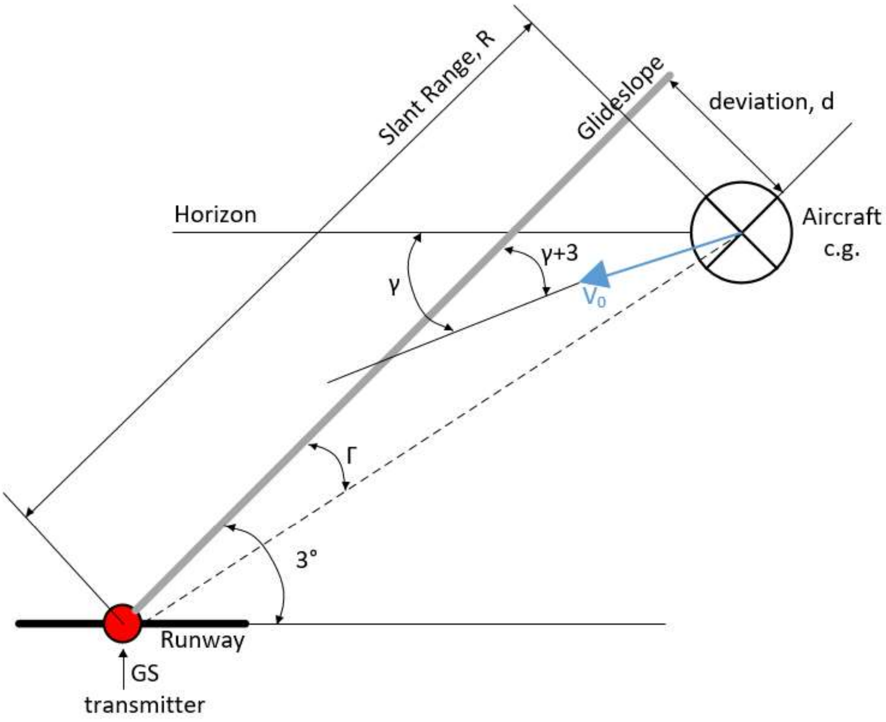

Figure 5.3: Glideslope overview

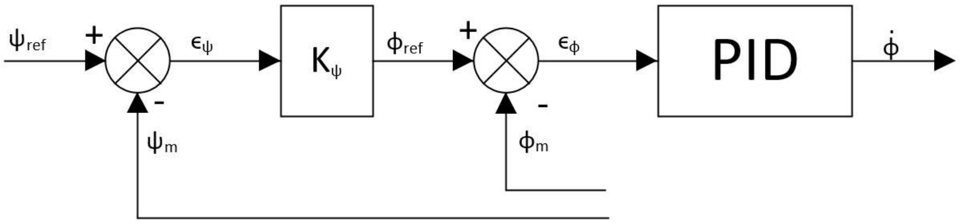

Figure 5.4: Longitudinal Autopilot: Heading Hold control scheme

5. In figure 5.5, the localizer intercept control scheme for longitudinal control is shown. The reference angle λ is the angle between the slant range R and the intended path. The slant range is the absolute distance from the aircraft c.g. to the localizer transmitter. An overview of the localizer is shown in figure 5.6. The localizer angle λ is defined as

$$\lambda = \operatorname{asin}\left(\frac{d}{R}\right) \approx \frac{d}{R} \tag{5.2}$$

where the deviation distance d is

$$d(s) = \frac{1}{s} V_0 \cdot (\psi_m - \psi_{airport}) \tag{5.3}$$

where the slant range R is the absolute distance between the localizer and aircraft c.g. The input is the reference localizer angle of $\lambda = 0$ and the position of the airport in relation to the aircraft. The output is the reference heading angle ψ_c, which is translated to the roll angle reference angle ϕ_{ref} using PID. The final output of this outer-loop is the commanded roll rate $\dot{\phi}$.

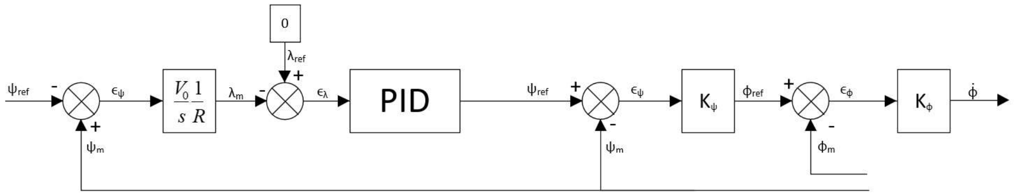

Figure 5.5: Longitudinal Autopilot: Localizer Intercept control scheme

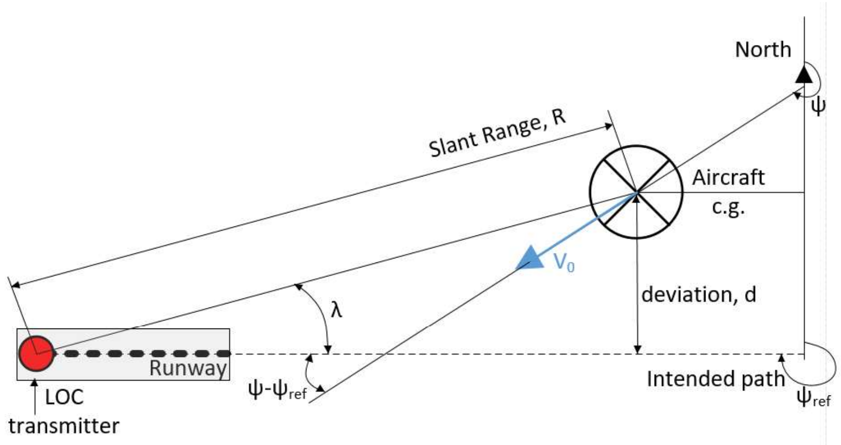

Figure 5.6: Localizer overview

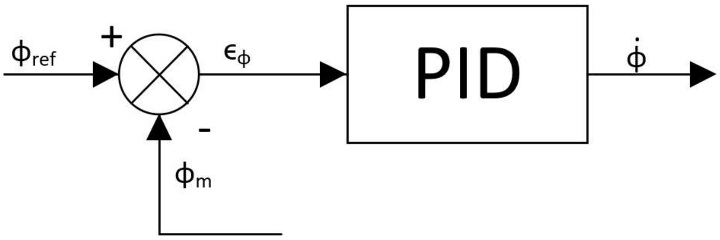

Figure 5.7: Longitudinal Autopilot: Roll Angle Hold control scheme

6. The roll angle hold mode is shown in figure 5.7. The inputs are ϕ_m and ϕ_{ref}. The output is $\dot{\phi}$.

Beside the six autopilots, an additional control loop is used for the flight control system. In figure 5.8, the sideslip angle hold mode control scheme is shown. The sideslip reference signal $\beta = 0$ throughout the simulation. The input is β_m and the output is $\dot{\beta}$.

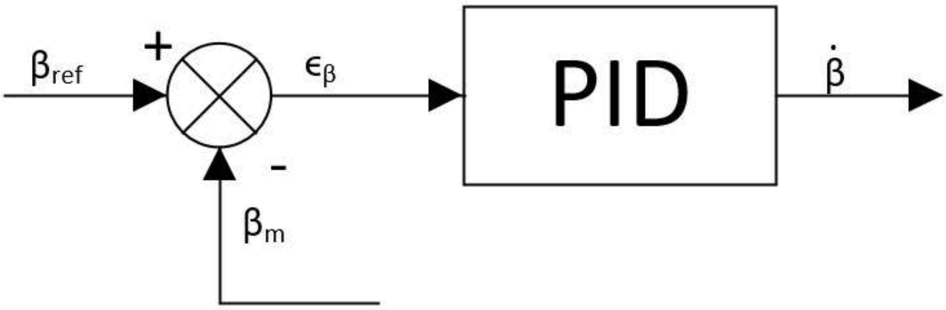

Figure 5.8: Sideslip Angle Hold control scheme

The lateral and longitudinal autopilots all have as output the commanded pitch rate $\dot{\theta}$ and roll rate $\dot{\phi}$ respectively and are used as direct controlled variables. The yaw rate r however is obtained by performing dynamic inversion of the sideslip angle [18]. The sideslip angle β can be defined as,

$$\beta = \sin^{-1}\frac{u}{V} \tag{5.4}$$

The first derivative of the sideslip angle is,

$$\dot{\beta} = \frac{\dot{u}V - u\dot{V}}{V\sqrt{u^2+V^2}} = \frac{\dot{v}}{\sqrt{u^2+w^2}} - \frac{v(u\dot{u} + v\dot{v} + w\dot{w}}{(u^2+v^2+w^2)\sqrt{u^2+w^2}} \tag{5.5}$$

The acceleration in the aerodynamic frame are given by,

$$\begin{aligned}\dot{u} &= A_x - g\sin\theta + rv - qw \\ \dot{v} &= A_y + g\sin\phi\cos\theta - ru + pw \\ \dot{w} &= A_z + g\cos\theta\cos\phi + qu - pv\end{aligned} \tag{5.6}$$

Substituting equation 5.6 in 5.5,

$$\dot{\beta} = \left(\frac{1}{\sqrt{u^2+w^2}}\right)(F_x + F_y + F_z) + \left[\frac{w}{\sqrt{u^2+w^2}} 0 \frac{-u}{\sqrt{u^2+w^2}}\right]\begin{bmatrix} p \\ q \\ r \end{bmatrix} \tag{5.7}$$

with

$$\begin{aligned}F_x &= -\frac{uv}{V^2}(A_x - g\sin\theta) \\ F_y &= \left(1 - \frac{v}{V^2}\right)(A_y + g\sin\phi\cos\theta) \\ F_z &= -\frac{vw}{V^2}(A_z + g\sin\phi\cos\theta)\end{aligned} \tag{5.8}$$

Then by solving for input r and the virtual control input $\nu_\beta(x)$,

$$\begin{aligned}r_c &= \underbrace{\left(\frac{-u}{\sqrt{u^2+w^2}}\right)}_{a_\beta(x)}{}^{-1}\left[\nu_\beta(x) - \underbrace{\frac{1}{\sqrt{u^2+w^2}}(F_x + F_y + F_z + wp_c)}_{b_\beta(x)}\right] \\ &= a_\beta(x)^{-1}[\nu_\beta(x) - b_\beta(x)]\end{aligned} \tag{5.9}$$

The sideslip compensation loop is shown in figure 5.9.

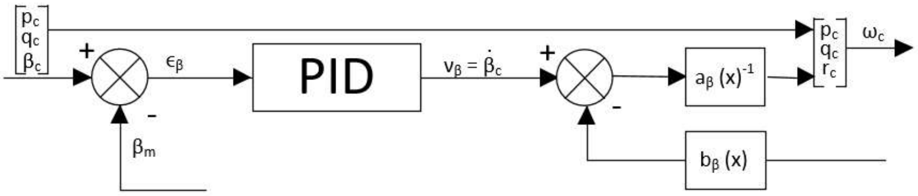

Figure 5.9: Sideslip dynamic inversion scheme

Each flight mode uses a combination of longitudinal and lateral autopilot together with the sideslip compensation loop. In this way the benchmark flight trajectories defined in the next chapter are flown.

6

Flight trajectory design

In this work, one of the main contribution is the four benchmark trajectories proposed for FTC testing for high performance aircraft. The trajectories are designed to test the robustness and performance of the ICE aircraft model while simulating effector failures. The impact of a chosen flight trajectory on the flight performance is assumed to be significant. Besides varying the flight trajectory to measure flight performance, the impact of disturbances such as wind and different starting conditions are also evaluated.

A high performance aircraft such as the ICE aircraft model is designed for far more extreme flight conditions than any passenger aircraft. Any flight testing on these aircraft can thus only serve as a reference to the flight testing of the ICE aircraft. However, the performance characteristics of high performance aircraft is not readily available, so one can only estimate which flight manoeuvres are possible. Since little research is available on the flight trajectories of high performance aircraft, this research aims to set the benchmark scenarios of future performance tests to be able to more easily compare results obtained from this research to other research on the performance of these type of aircraft models.

The failure cases considered in this research are limited to lock-in-place and hard-overs, which means that at time t_{fail}, the effector will be locked in-place at a defined failure angle δ_{fail}. In this case, the connection between actuator and flight control system is cut off. Other than the failure type, the failure time also has an impact on the performance. It is likely that the same failure that occurs in straight flight and during a turn or evasive manoeuvre will result in a significant difference in flight performance measured. To prove this fact, a sensitivity analysis is done on the failure time. Another part of the sensitivity analysis is to investigate the effect of starting conditions on the performance of the failed scenarios flown. The sensitivity analysis is performed using the Dryden turbulence model to simulate 20 realisations per failure condition. The details of the experiment will be explained in chapter 7.

Although there are currently no benchmark trajectories for fault tolerant control flight performance testing of high performance aircraft models in case of effector failures, there is one available for commercial aircraft in [9]. For high performance aircraft, these flight trajectories are also applicable. However, high performance aircraft have been designed for aggressive and evasive manoeuvres to be able to perform their missions. Therefore, two flight phases have been designed to reflect the full capabilities of these aircraft. One is an avoidance manoeuvre, a 180 degree turn within 10 seconds, while the other is a 270 degrees roll manoeuvre within 1.5 second. Although these time-frames will not be the minimum time-frames in which these actions can be performed, they are sufficiently aggressive for the tests in this research. The current model of the ICE aircraft does not include any additional turbulence model due to ground effect, therefore the final approach trajectory will not be included in this research and is left for future research. The full benchmark flight scenario for the qualification of the fault tolerant control system with four trajectories is shown in figure 6.1 and are described below.

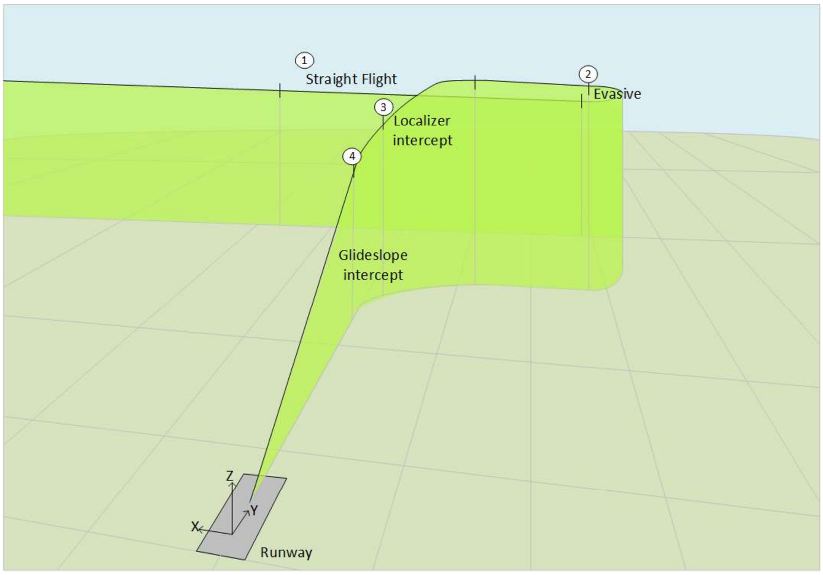

Figure 6.1: Benchmark flight scenario for performance testing of the INCA FTC system of the ICE aircraft model with effector failures.

1. **Straight Flight**

   During straight flight, the altitude, flight speed and heading is kept constant using the Altitude Hold mode for lateral control, Heading Hold mode for longitudinal control and auto-throttle for constant airspeed. In table 6.1, the aircraft states are listed that are used to analyse aircraft performance between straight flight with and without failure. By analysing the closed loop system time responses, one can compare the quality of different control strategies. During this manoeuvre, the aircraft should remain within a predefined box like a tunnel in the sky.

Table 6.1: Aircraft state variables for straight flight

Symbol	Quantity
V	Velocity
γ	Flight path angle
α	Angle of attack
β	Sideslip angle
n_z	Load factor
ϕ	Roll angle

Table 6.2: Aircraft state variables for evasive manoeuvre

Symbol	Quantity
V	Velocity
p	Roll rate
q	Pitch rate
q	Yaw rate
α	Angle of attack
β	Sideslip angle
n_z	Load factor
A_y	Lateral Specific Force
ϕ	Roll angle

2. **Evasive manoeuvre**

   A 180 degree turn (change in heading) is performed to investigate to which degree mission specific manoeuvres can be flown in case of effector failure for high performance aircraft. This turn is followed by a 270 degree roll manoeuvre to quickly attain straight flight conditions. For the evasive manoeuvre a direct p and q rate control input is given while the sideslip angle is kept at zero $\beta_{ref} = 0$. Followed by straight flight using the previous discussed autopilot. In table 6.2, the assessment criteria for this manoeuvre are listed.

   The turn itself is an upwards spiral manoeuvre. One criteria is that it should be performed within 10 seconds. Such a turn can only be achieved at a lower velocity than cruise velocity which is achieved by a sudden increase in angle of attack. The performance of this manoeuvre is evaluated in two phases, the first phase is the turn within 10 seconds and is evaluated by the change in heading. The second phase is the the roll manoeuvre to attain straight flight and the criteria that is measured specifically for this phase is the time it takes to return the aircraft to equilibrium conditions.

3. **Left-hand turn and localizer intercept**

   A left hand turn is performed to get in range of the localizer of the nearest runway. For this manoeuvre, the Heading Angle Hold mode is used to turn towards the runway till the localizer intercept mode is engaged. In table 6.3, the aircraft state variables for this manoeuvre are listed. An overview of the lcoalizer hold mode was given in figure 5.6. One performance criteria that is monitored is the localizer deviation and should be close to zero at the end of the manoeuvre.

Table 6.3: Aircraft state variables for left-hand turn and localizer intercept

Symbol	Quantity
λ	Localizer deviation angle during end
V	Velocity
p	Roll rate
q	Pitch rate
q	Yaw rate
α	Angle of attack
β	Sideslip angle
n_z	Load factor
A_y	Lateral Specific Force
ϕ	Roll angle

Table 6.4: Aircraft state variables for the glideslope intercept

Symbol	Quantity
λ	Localizer deviation angle
Γ	Glideslope deviation angle during end
V	Velocity
p	Roll rate
q	Pitch rate
q	Yaw rate
α	Angle of attack
n_z	Load factor

4. **Glideslope intercept**

   When the aircraft is close enough to the airport, the glideslope intercept mode is engaged. The reference trajectory is given by a glideslope of 3 degrees. In table 6.4, the aircraft state variables for this manoeuvre are listed. An overview of the glideslope manoeuvre was shown in figure 5.3. When the glideslope intercept mode is engaged the localizer hold mode is still active and the localizer deviation λ should be kept minimum. The glideslope deviation angle is also monitored and should be close to zero at the end of the manoeuvre. This manoeuvre is used mainly to show that a landing procedure can be followed while effector failures are present.

The flight trajectories described in this section will be used to assess the performance of the aircraft. The designed flight envelope limits for nominal aircraft operations, i.e. load limits, rotational rate limits, maximum and minimum velocity, can be used to identify catastrophic failures. After the failure event, the reference trajectories still have to be followed consecutively as shown in figure 6.1.

The two main evaluation criteria are,

- The operating limits of the aircraft may not be exceeded after failure

- The ability to reconfigure the controller such that the aircraft states are controlled with adequate performance

The performance can be measured by the time to reach equilibrium and the time to accomplish for manoeuvres where only an end-point is defined. The input commands and performance criteria are different for each flight trajectory as different autopilot (and gains) are used to complete the flight trajectories. Throughout all flight phases, the commanded speed is kept constant. The aircraft has been tuned per flight trajectory.

7

Results and discussion

The evaluation of the FTC performance of INCA using the autopilots designed in chapter 5 for the benchmark trajectories defined in 6 was based on real-time simulation setup with the high-fidelity ICE model described in chapter 2. The evaluation was done for the lock-in-place and hard-over effector failures for every flight trajectory. The metrics used to evaluate the performance of each failure were the tracking performance of the flight control system with respect to the failure free case and the severity of the failure bounded by load factor, maximum yaw rate and minimum velocity. First, a sensitivity analysis of the impact of the chosen simulation parameters, failure time and initial flight condition, is tested. Then the aircraft parameters and the control effector deflections are analysed for each flight trajectory.

In this chapter the simulation setup and results are discussed. The simulation setup is described in section 7.1. The sensitivity analysis of the parameters failure time and initial conditions is discussed in Section 7.2 and the performance results and analysis of each trajectory in Section 7.3.

7.1. Simulation Setup

The high fidelity ICE model described in chapter 2 and the INCA algorithm described in chapter 3 were set up in a Matlab/Simulink framework to test the effector failures identified in chapter 4. The INCA algorithm was used with the active set-based QP control allocation solver. The simulations were run in real-time with a fixed sampling rate of 100Hz and a 4th-order Runge-Kutta solver. The simulations were run on a 64-bit (Windows 10) laptop with four Intel(R) Core(TM) i7-4710MQ CPU @ 2.50GHz processors and 8.0 Gb of RAM.

Depending on the flight trajectory, the flight simulations were initialised in trim conditions at an altitude of 2000ft and a Mach number of 0.85 or at 1000ft with a Mach number of 0.4. The corresponding true airspeed was 880 ft/s and 430 ft/s respectively and is used as a constant reference for the auto-throttle (A/T) module. The linear gains of the inner-loops for body rate control were all set to the values listed in table 7.1. For the fault-free case the penalty gains in W_δ were set to 1 except for the AMTs and PF, which were set to 0.5 and as discussed in section 4.2 the $W_{\delta SSD}$ is a function of α as given by equation 4.5. For failure cases this weight is dependant on the type of failure. The weight of W_τ were all set to 1 and the control preference vector δ_p was set to 0 for all control effectors in all cases.

	p	**q**	**r**
$K_{\omega P}$	6.5	6.5	5.8
$K_{\omega I}$	0	0	0
$K_{\omega D}$	0.5	0.5	0.5

Table 7.1: Linear gain used for inner loop body rate control

7.2. Sensitivity Analysis

Using a sensitivity analysis, one can show the impact of model parameters such as the failure time and initial conditions on the results that are obtained. All the analysis in this section are performed only for the evasive manoeuvre and straight flight manoeuvre. Because the left hand turn is a much less demanding manoeuvre than the evasive manoeuvre and the glideslope intercept is a special case of straight flight with a small glide path angle and heading angle difference. The first part of the evasive manoeuvre is performed by providing control inputs directly to the inner loop. To initiate the turn a roll rate input p is given of 50 deg/s for 1 second and simultaneously a pitch rate command of 20 deg/s during 10 seconds while the sideslip input is kept at $\beta = 0$. After 10 seconds a 1.35 roll rate input of 200 deg/s is given to roll the aircraft around after the turn is finished. The second part starts at 16 seconds after the turn manoeuvre was initiated, the auto pilot system is engaged for altitude and heading control with $h_{ref} = h_{trim}$ and $\psi_{ref} = 180$ degrees. The straight flight manoeuvre is also controlled by the auto pilot with the altitude and heading control engaged at $h_{ref} = h_{trim}$ and $\psi_{ref} = 0$. The simulation length for all tests is 40 seconds not only to limit total simulation time for all tests but also because only a short simulation time is needed to analyse the robustness of the flight system for single manoeuvres.

7.2.1. Dryden turbulence model

The influence of turbulence is added with a Dryden Turbulence model. The settings were chosen with a wind speed of 5 ft/s at low-altitude, a medium/high altitude scale length of 1750 ft and the noise seed of $ug = 23341$, $vg = 23342$, $wg = 23343$, $pg = 2344$. The Dryden models uses the mathematical representation specified in the Military Specification MIL-F-8785C. The continuous Dryden Wind Turbulence Simulink Model block has been used to simulate the turbulence. Turbulence is used to determine to what degree the outcomes of the failures tests depend on the turbulence settings. For this purpose 20 realisations, 20 flights with varying noise seeds, of the same effector failure are run to determine the mean and the variance of the total RMS error between the fault free body rates and the effector failure case. The total RMS error is the addition of the RMS error of p, q and r between the failure free case and the failure case. A single manoeuvre where all effectors are tested in this way generates a total of 521 simulations to test 13 effectors for both the upper and lower limits. These 521 simulations are visualised in a single figure with both a boxplot to show the mean of the RMS error as well as a bar graph for those tests that failed before the end of the simulation. A simulation fails when the limit load factor of 20, a yaw rate higher than 200 deg/s, the minimum velocity or minimum altitude has been reached. No RMS error is recorded for failed flights but are visualised in the bar graph.

7.2.2. Failure time

To investigate the effect of failure time during the flight manoeuvre, two different failure times are compared to each other for the evasive manoeuvre case. A comparison of failure time for the straight flight manoeuvre is not performed as during normal operations of this manoeuvre no significant change is aircraft states are present between time T_0 and T_1. The standard failure time of $T_{fail} = 5$ is compared to the failure time of $T_{fail} = 11$, the second failure time occurs during the end of the fast roll manoeuvre while the standard failure occurs during the turning phase. An impression of the flight trajectory for every realisation is given in figure 7.1a and figure 7.1b. In both trajectory one can see that large deviations from the nominal trajectory occurs close to time of failure. A closer look at the specific effectors can be seen in figure 7.2a for $T_{fail} = 5$ and in figure 7.2b for $T_{fail} = 11$. The failures case tested here is for hard-overs to find at which failure condition it is likely to find more realisations that stay within specified structural limits. A more in-dept analysis will be given for each critical effector in the next section of this chapter. Both figures show high RMS error and a failed realisations for the same effectors: SSDs, elevons and TV. The most significant difference is that the failure at 11 seconds has a greatly reduced tolerance to a hard-over of the left elevon at 15/20 realisations failed compared to the 5 seconds case where no realisation failed.

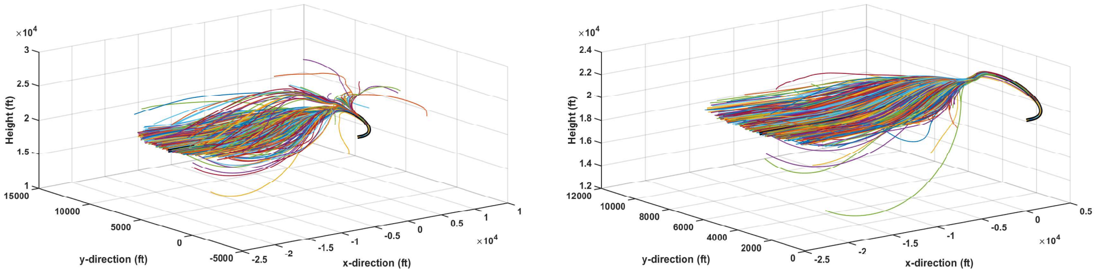

(a) (b)

Figure 7.1: Aircraft trajectories starting at trim conditions FL200 and target velocity of 880 ft/s of the evasive manoeuvre for **all** realisations with a) failure time $T = 5$ and b) failure time $T = 11$ during 40 seconds of simulation time of hard-over failure testing.

A possible explanation is that the left elevon is used during the roll manoeuvre and at that time a hard-over causes a more significant flight trajectory change than the same failure during the turn at the failure time of 5 seconds.

7.2.3. Initial conditions

Another important parameter that has an impact on the flight performance is the starting condition, i.e. flight level and velocity, at which trim conditions have been established has an impact on which manoeuvres are possible due to effector failures. In this analysis the previously discussed trajectory at failure time $T = 5$ is compared at two different flight levels: FL200 and FL100. The failure cases are identical to the ones used in the failure time sensitivity analysis. For the evasive manoeuvre the results of this analysis are shown in figures 7.2b and figure 7.2c. What is noticeable is that at FL100 more flights fail and also almost every hard-over of any effector can cause failures compared to the FL200 case.

An initial condition analysis has also been performed for the straight flight manoeuvre. The angles used in this failure analysis are the maximum and minimum obtainable angles for each effector specified in table 2.2. The results are shown in figure 7.3a for FL200 and in figure 7.3b for FL100. From these figures it can be shown that the most critical effector failures occur for hard-over failures of the SSDs, AMTs and yaw TV. One significant change between FL200 and FL100 is that at FL100 yaw TV causes failures instead of the AMTs at FL200. This might indicate that at higher speed and altitude AMT is more critical and at lower speed and altitude the yaw TV for straight flight.

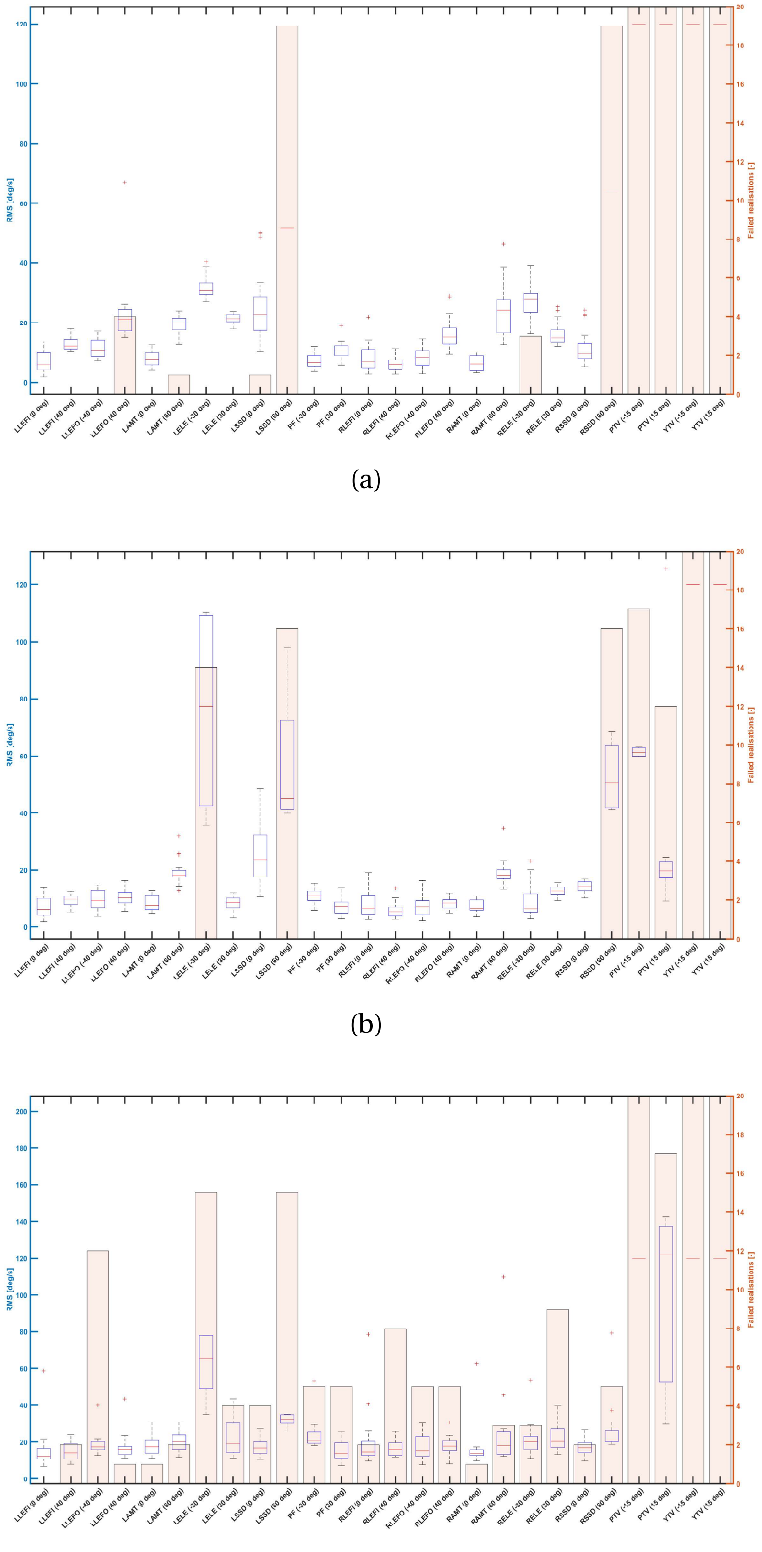

(a)

(b)

(c)

Figure 7.2: The total RMS error between the realisations and the fault free flight case for each realisation shown in a boxplot for evasive flight of 40 seconds with FL200 and target velocity of 880 ft/s on the left y-axis and the corresponding failed realisations on the right y-axis in a) for failure time $T_{fail} = 5$ and in b) for failure time $T_{fail} = 11$ and in c) for failure time $T_{fail} = 5$ at FL100 instead of FL200.

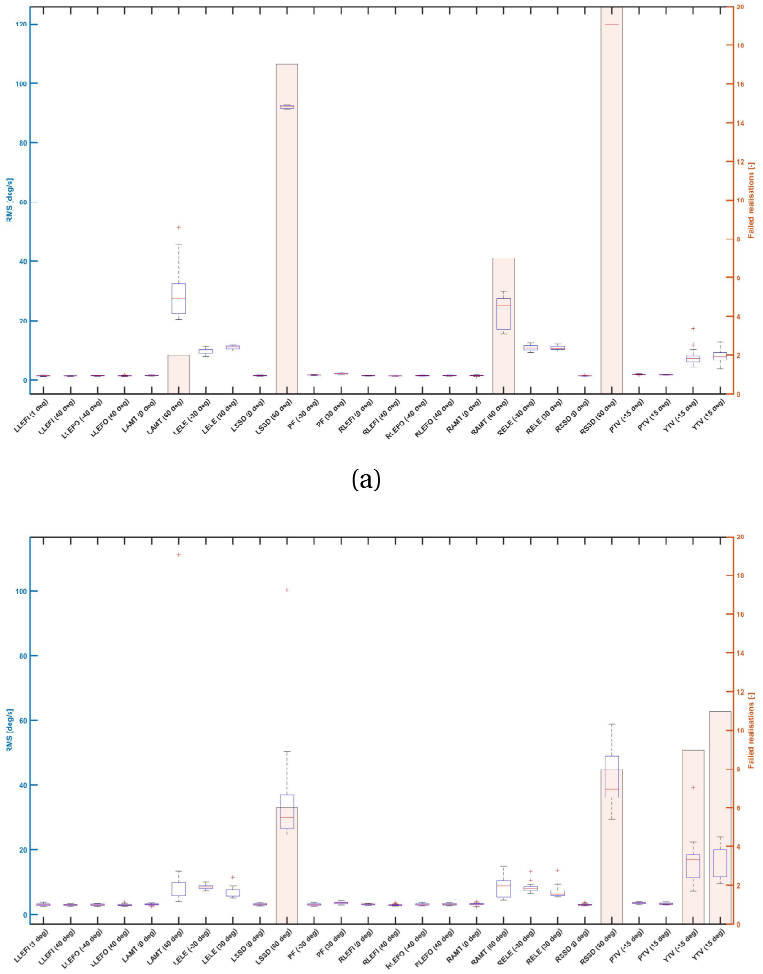

(a)

(b)

Figure 7.3: The total RMS error between the realisations and the fault free flight case for each realisation shown in a boxplot for straight flight of 40 seconds on the left y-axis and the corresponding failed realisations on the right y-axis in a) for FL200 and in b) for FL100.

7.3. Trajectory Performance

Although a lot of results are obtained from each flight trajectory, only a chosen few are shown in this section to provide a clear overview. For each flight trajectory, the Root-Mean Square (RMS) error between the fault-free flight and flight with a failure is measured of the rotation rates p, q and r. The flights are then ordered from high to low based on the total RMS error of these rates. In the figures shown in this section, only the highest, lowest and the closest to the median of the total RMS effector failure flight cases are shown. The normal flight is shown as a straight solid line. The 'worst-case' with the highest total RMS error flight is shown as the dashed line. The average total RMS error case is shown as the dotted line and the flight close to the fault-free case as the dash-dot line. Furthermore additional failure tests were performed based on the sensitivity analysis results in previous section to gain more insight in the failure behaviour of the critical effectors for each flight phase. That means for straight flight additional test on the SSDs and AMTs were performed at different angles, each angle tested using 20 realisation, to obtain the box-bar plots seen in section 7.2. Note that the failures shown in the figures for flight trajectory, aircraft states and effector deflections are single realisations of the failure case which did not exceed the structural and operational limits imposed on these tests.

Straight flight

All flight manoeuvres tested start from trim conditions in straight flight. Straight flight is performed at a height of 20000 ft with $M = 0.85$ in trim conditions and the failure is introduced after 5 seconds. Starting with the limit deflections, both upper and lower limits, the scenario is flown for a duration of 40 seconds. Not all flights can be performed as the loads on the aircraft become unrealistically high. For the ICE aircraft, the limits loads are assumed to be $n_z > 20$ or $n_z < -20$ before the structural integrity of the aircraft is affected. After single realisation testing the worst, best and median failure cases are automatically selected from the simulation files for straight flight. Note that these labels are not absolute truths as it depends on the turbulence conditions and not all possible failure cases (not all angles) were tested before selection. In this case the worst performing failure case was found to be the LSSD at 59 degrees, the closest to failure free flight was the RLEFI at 0 degrees and the RELE at -30 degrees was closest to the median of all test cases considered. The aircraft trajectories of these realisations are shown in figure 7.4a and the aircraft states are shown in figure 7.4b. The RMS errors are shown for the highest, average and smallest RMS error in table 7.2.

Performance	**LSSD (59 deg)**	**RELE (-30 deg)**	**RLEFI (0 deg)**
p [deg/s]	57.94	5.493	0.0006792
q [deg/s]	23.11	2.47	0.0009798
r [deg/s]	37.6	2.394	0.0003714
Total RMS [deg/s]	118.6	10.36	0.00203

Table 7.2: RMS of the error between the normal straight flight manoeuvre and flights with failure shown for the highest, medium and smallest total RMS error

In these figures, it can be seen that the 'worst case', where the LSSD is stuck at 59

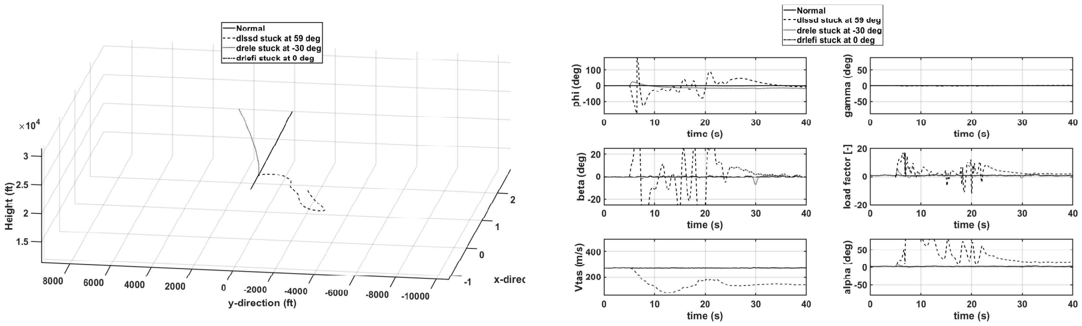

(a)

(b)

Figure 7.4: Aircraft trajectories and aircraft states during the limit failures that are within structural limits for straight flight of the tested limit cases.

degrees, can not be considered to be flying a straight level flight. An initial spike in the roll angle can be observed along with a large drop in speed and a constant high AOA during the first 15 seconds after failure. In case the RELE is stuck at -30 deg, much less noticeable aircraft states deviations are observed at failure time. However, the trajectory does diverge from the original heading due to the failure event.

Although the load limits were not exceeded in these cases, the aircraft is clearly not controllable with just the autopilots engaged for the LSSD and RELE failure case. Furthermore it is not clear whether or not in different turbulence (weather) conditions structural limits will not be exceeded. For this reason 20 realisations have been simulated of the worst single failure cases for the straight flight condition. In figures 7.6a and 7.6b the flight realisations which did not exceed structural limits for 40 seconds of flight for the right and left SSDs respectively are shown.

16 realisations out of 20 were within structural limits for both SSD effector failures at 59 degrees are measured. In appendix B flight data of the realisations for straight flight is shown in a table. Also the right and left AMT have been tested at maximum failure deflection of 60 degrees, but none of these realisations crossed the load limits of 20. The mean of the RMS error between normal flight and the realisations per failure case can be seen from the boxplot shown in figure 7.7.

It is clear from the boxplot in figure 7.7 that the SSDs are much more critical near their maximum deflection failure than the AMTs at FL100 for straight flight as the RMS is higher and the fact that only 16 realisations were within structural limits. These results are in accordance with the results obtained from the initial condition sensitivity analysis.

In figure 7.5a, the thirteen aircraft effector deflections during straight flight are

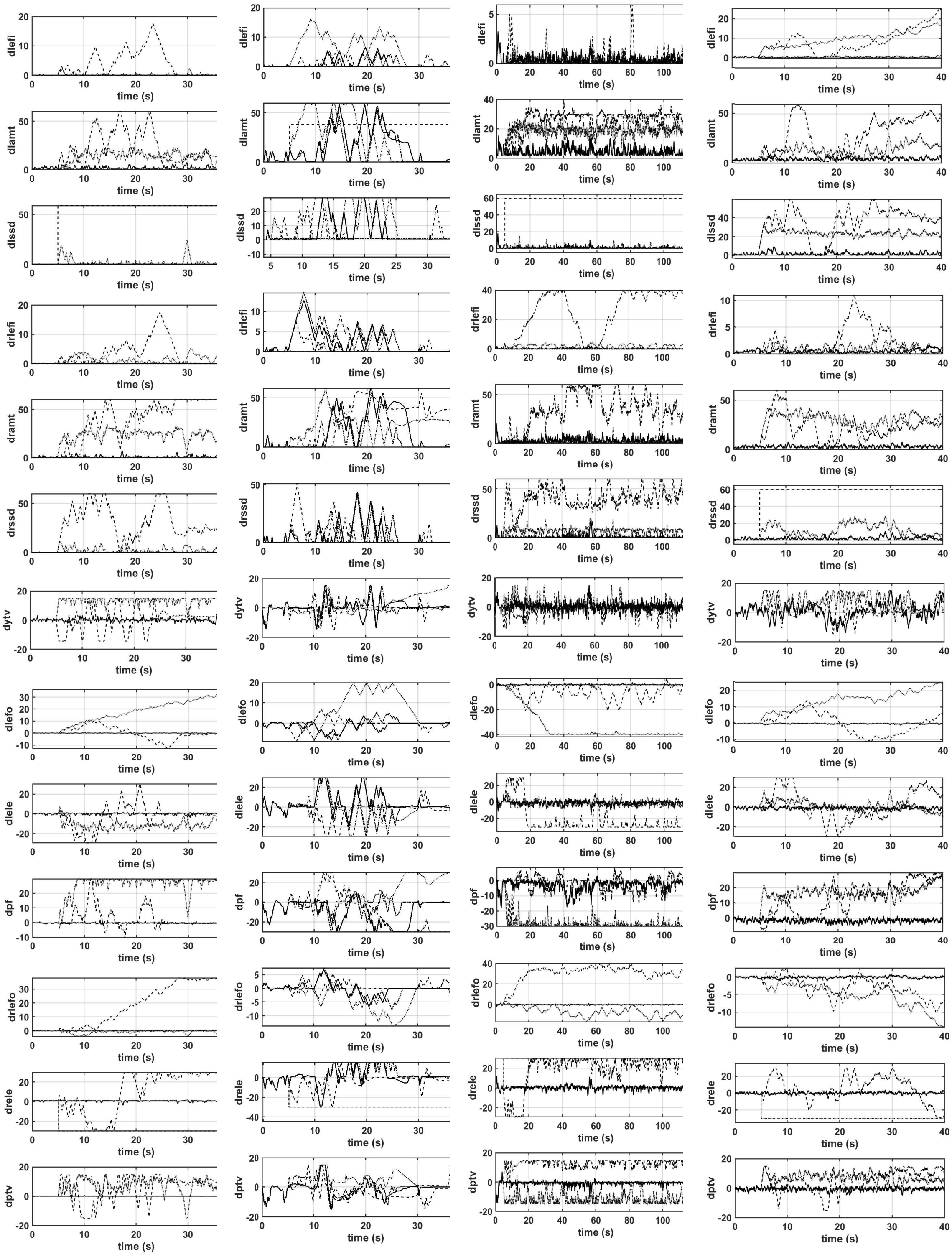

(a) (b) (c) (d)

Figure 7.5: Aircraft effector deflections during (a) the limit failures that are within structural limits for straight flight, (b) a 180-degree turn within 10 seconds followed by a 270 degree roll and straight flight of the tested limit cases, (c) the left hand turn and localizer hold mode of the tested limit cases, and (d) glideslope of the tested limit cases.

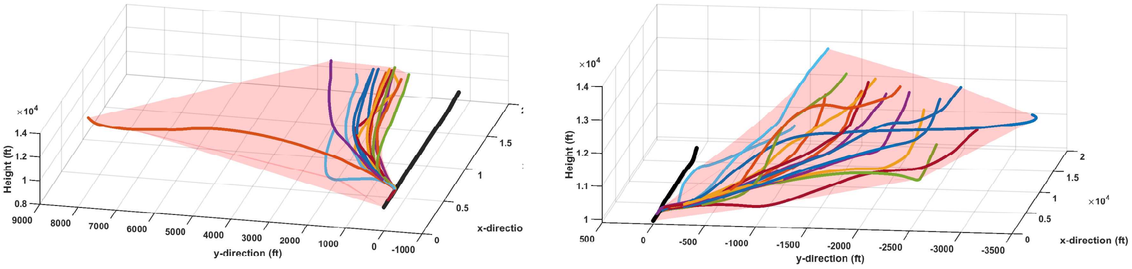

(a) (b)

Figure 7.6: (a) 16 realisation of the RSSD failure stuck at 59 degrees (b) 16 realisation of the LSSD failure stuck at 59 degrees. Both are measured at FL200 and velocity of 880 fps for 40 second flight with failure time $T = 5$

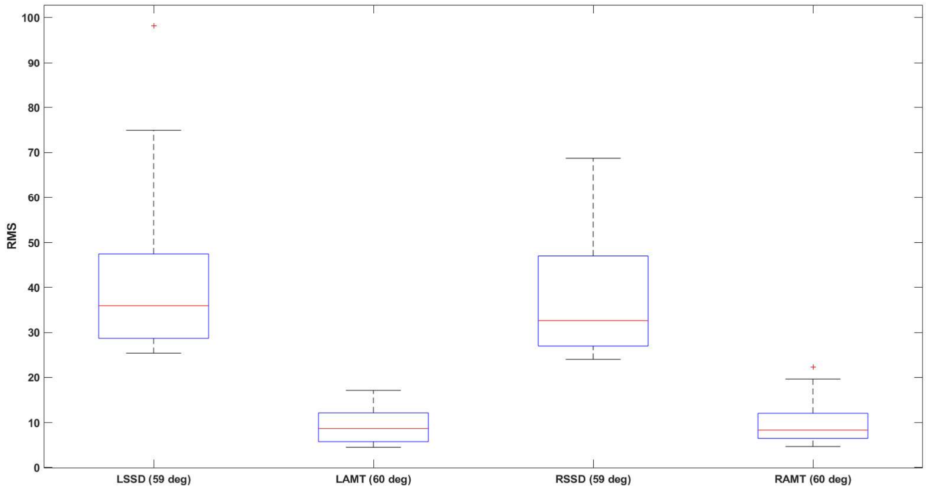

Figure 7.7: The total RMS error between the realisations and the fault free flight case for each realisation shown in a boxplot for the SSDs and AMTs in straight level flight condition for 40 seconds with FL100 and velocity of 430 ft/s and failure time $T = 5$

shown. In these figures the effector failure of the effectors can be seen and how the control effort of failed flights is much larger than of the fault-free case. As well as near saturation of the pitch flap from the average failure case and right side saturation of the RLEFO and RELE in the worst case.

Evasive manoeuvre

The 180 degrees turn within 10 seconds is performed from straight flying conditions as defined previously. At time $T = 5$, the effector failure occurs and at time $T = 10$, the manoeuvre should be finished. To return to straight flight, a 270 degree roll manoeuvre is performed at time $T = 10$. The total simulation time for this manoeuvre is 40 seconds. Four flight trajectories of this manoeuvre are shown in figure 7.8a and the corresponding aircraft states in figure 7.8b. Next to normal flight the flight trajectories and their states of the failure cases with a high, average and small RMS error as given in table 7.3 are shown in the figures.

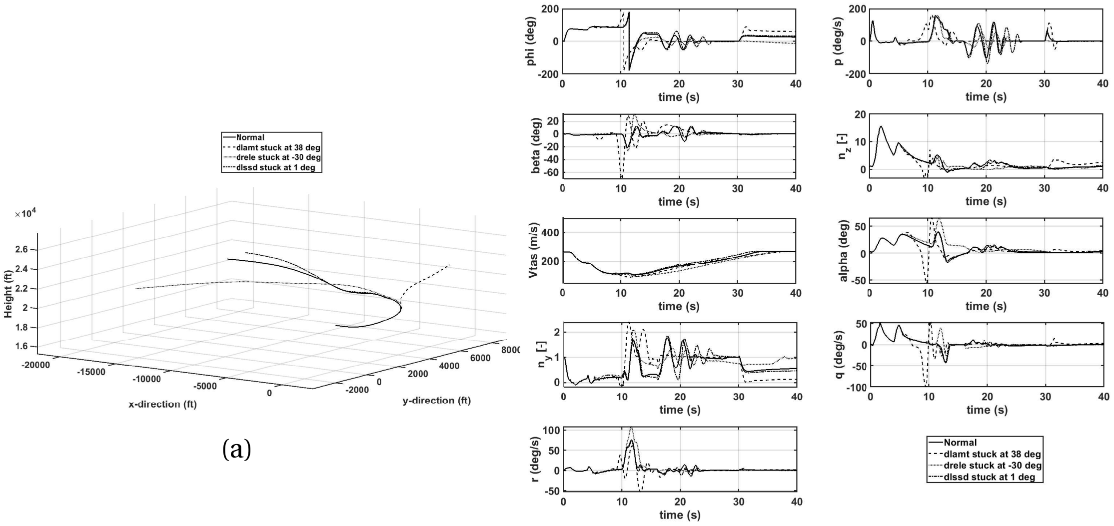

(a)

(b)

Figure 7.8: Aircraft trajectories and aircraft states of a 180-degree turn within 10 seconds followed by a 270 degree roll and straight flight of the tested limit cases.

Performance	LAMT (38 deg)	RELE (-30 deg)	LSSD (1 deg)
p [deg/s]	44.92	29.34	18.93
q [deg/s]	16.28	7.775	1.793
r [deg/s]	12.81	8.85	2.896
Total RMS [deg/s]	74.02	45.96	23.62

Table 7.3: RMS of the error between the normal evasive manoeuvre and flights with failure shown for the worst, medium and smallest total RMS error

The LAMT stuck at 38 degree and the RELE stuck at -30 degree diverge by large margin from the fault-free scenario. The effector deflections belonging to this manoeuvre are shown in figure 7.5b. It can be seen in these figures that this manoeuvre requires quite a bit of control effort even without effector failure. For the high and average (RMS error) case, the pitch flap is saturated at the end of the manoeuvre. For the average case, the TV in both directions gets saturated at the end as well. For this manoeuvre also more realisations have been run to determine the certainty bounds. The mean of the RMS error between normal flight and the realisations per failure case can be seen from the boxplot shown in figure 7.9.

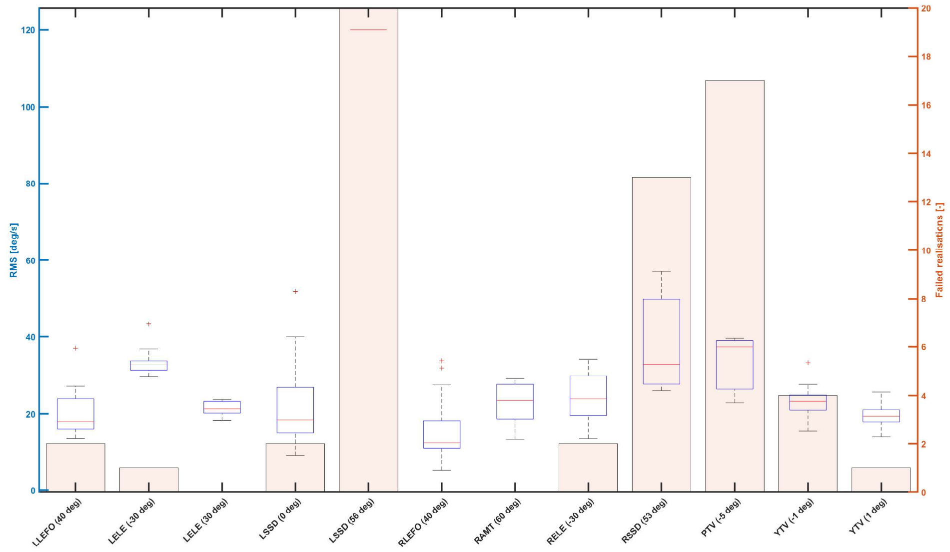

Figure 7.9: The total RMS error between the realisations and the fault free flight case for each realisation shown in a boxplot for evasive flight of 40 seconds with FL200 and target velocity of 880 ft/s including the corresponding failed realisations on the right y-axis.

In figure 7.9 the number of realisations that exceeded limit loads is given per failure case as well. For the failure case were the LSSD is stuck at 56 degree all realisations exceeded the load limits. The failure cases of the PTV stuck at -5 degrees and the RSSD stuck at 53 degrees are shown in figure 7.10a and 7.10b respectively. From these figures together with the boxplot it is clear that these two failures are critical as most realisations result in a loss-of-control event and the remaining have a high RMS error. All the other figures and data from the realisation analysis can be seen in appendix C.

The angle used for this realisation test are not hard-overs but are stuck at different angles. The yaw TV failures were tested close to their neutral position at 1 and -1 degrees. The Yaw TV hard-overs shown in figure 7.2 resulted in a 100% failure rate and even close to their neutral position for this manoeuvre loss-of-control events still occur.

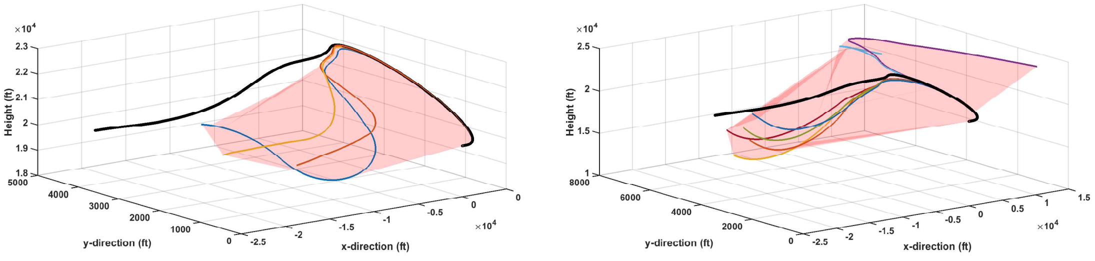

(a) (b)

Figure 7.10: (a) 3 realisation of the PTV failure stuck at -5 degrees (b) 7 realisation of the RSSD failure stuck at 53 degrees for the evasive manoeuvre. Both are measured at FL200 and velocity of 880 fps for 40 second flight with failure time $T = 5$

Left hand turn & localizer

This manoeuvre is tested starting at trim conditions at $FL = 100$, with 430 ft/s. For the first 40 seconds the heading angle hold mode is activated for a 280 degree heading and the altitude hold mode at 10000 ft. At 40 seconds the localizer is engaged as the aircraft enters the airports range. With a runway at 270 degrees at (4500ft, -100,000ft). The simulation is run for 120 seconds. The flight trajectory is shown in figure 7.11a. It can be seen that for the case where the LSSD is stuck at 60 degrees the normal flight trajectory can not be followed. In figure 7.11b, the aircraft state variables are shown. The RMS errors are shown for the highest, average and smallest RMS error in table 7.4.

Performance	**LSSD (60 deg)**	**RELE (30 deg)**	**LEFI (0 deg)**
p [deg/s]	12.04	1.653	0.02026
q [deg/s]	6.876	1.367	0.01156
r [deg/s]	6.178	0.7615	0.007722
Total RMS [deg/s]	25.09	3.782	0.03954

Table 7.4: RMS of the error between the normal localizer intercept manoeuvre and flights with failure shown for the highest, medium and smallest total RMS error

The initial spike in α and β causes the trajectory to change drastically. During the mode change a spike in ϕ and p can be observed, this is due to the sudden change in heading reference. In figure 7.5c, the effector deflections are shown during this manoeuvre.

From these deflections, it can be seen that for the worst case with the LSSD stuck at 60 degrees, a large control effort is demanded from the right-side control effectors to compensate for this. For the case the RELE is stuck at 30 degrees, most compensation

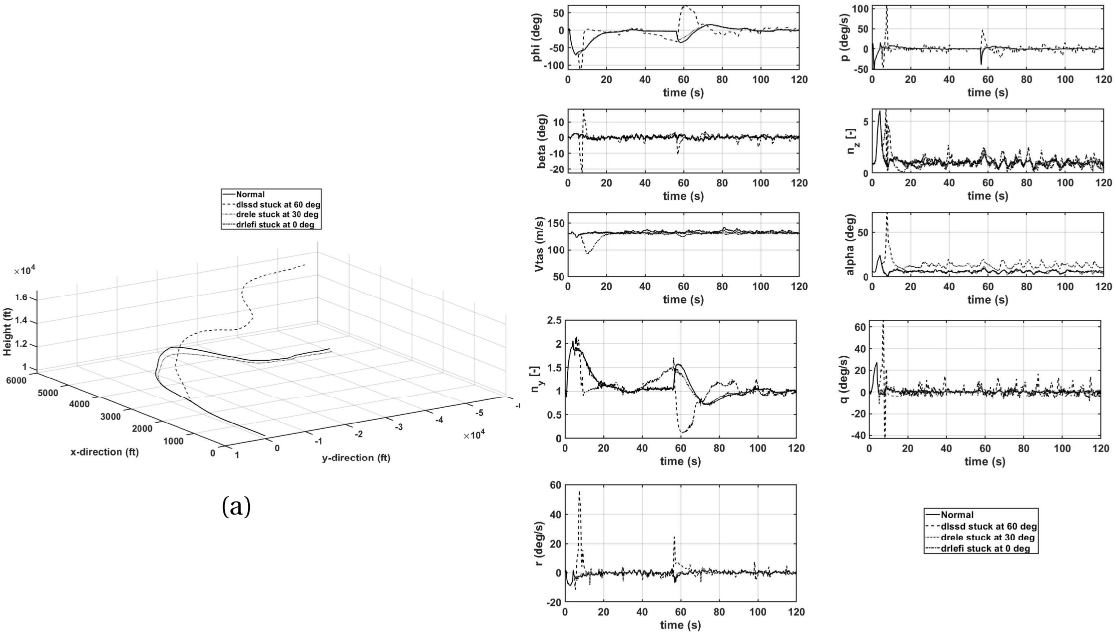

(a)

(b)

Figure 7.11: Aircraft trajectories and aircraft states of the left hand turn and localizer hold mode starting at FL100 with 430 ft/s for 120 seconds of the tested limit cases.

is asked of the PF and the LAMT as well as pitch TV.

Glideslope

Like the Localizer Hold mode the Glideslope is tested at FL=100 for 430 ft/s. This time it is the RSSD instead of the LSSD that has the highest RMS error. In figure 7.12a the Glideslope trajectory is shown.

It can be seen that a stuck RSSD of 60 degree does not follow the glideslope at all. While the average RMS error case, the RELE stuck at -30 degree, is not far off. The aircraft states confirm that mainly the worst case causes a large deviation from fault-free aircraft states as shown in figure 7.12b. The RMS errors are shown for the highest, average and smallest RMS error in table 7.5.

In this table it can be seen that the highest RMS error is caused by roll rate control and that the total RMS of the RSSD at 60 degrees is at least 8 times higher than the RMS of the RELE at -30 degrees. The effector deflections during the glideslope are given in figure 7.5d. In these figures, the effect on the control allocation due to the failure is shown by large deflections of the SSDs and AMTs after failure time t_{fail}.

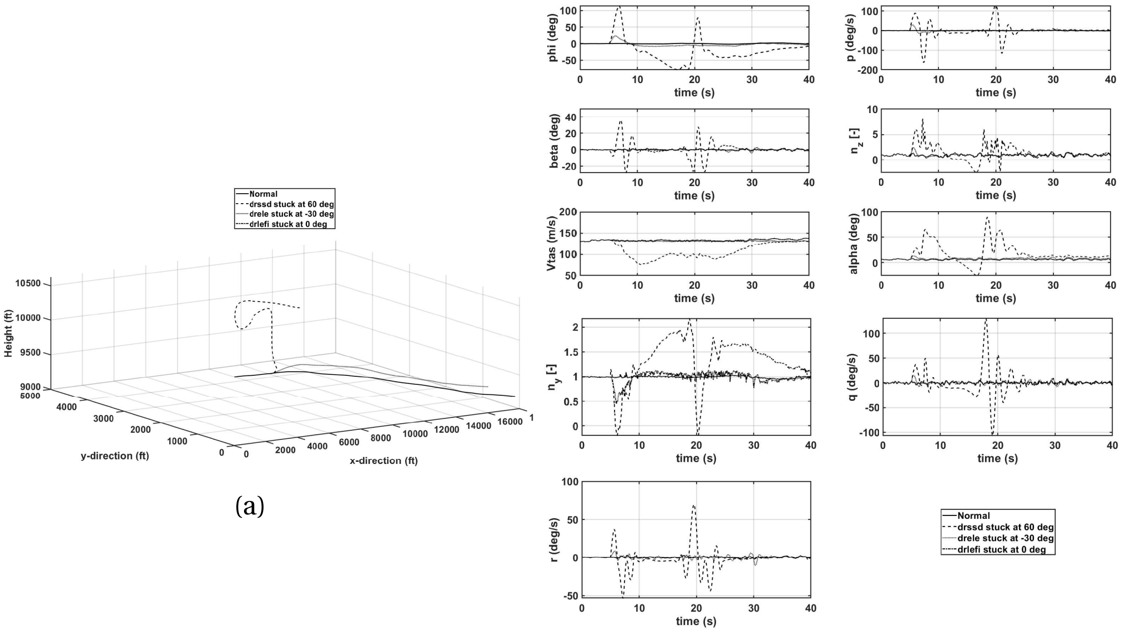

(a)

(b)

Figure 7.12: Aircraft trajectories and aircraft states of the glideslope starting at FL100 with 430 ft/s for 40 seconds of the tested limit cases.

Performance	RSSD (60 deg)	RELE (-30 deg)	RLEFI (0 deg)
p [deg/s]	34.96	4.619	0.04157
q [deg/s]	24.76	2.656	0.02473
r [deg/s]	15.59	2.095	0.03048
Total RMS [deg/s]	75.31	9.371	0.09678

Table 7.5: RMS of the error between the normal glideslope manoeuvre and flights with failure shown for the highest, medium and smallest total RMS error

All trajectories have been tested and the most critical effectors during each trajectory were identified. Because this aircraft has not been build yet, it is interesting to compare the criticality of the effectors identified during the design phase to the simulated criticality of the effectors in this paper. In [8], actuator redundancy is discussed and a ranking system is made of the criticality of combined actuator failures in order to determine which effectors would require dual hydraulic systems, an example is shown in figure 2.2. This information shows that during the design the yaw TV, SSD and Elevons were already found to be the most critical. However the AMT were not evaluated in this criticality matrix, but in this paper it was shown that they do have a big impact on the performance during evasive manoeuvres at lower velocity and altitude.

8

Conclusions and recommendations

In this thesis, multiple novel methods were discussed which are (combined) able to improve on existing Fault Tolerant Control (FTC) methods. For a high-performance aircraft such as the Innovative Control Effector (ICE) model aircraft the nonlinearities and high coupling between the control effectors shown in its aerodynamic model are particularly relevant when designing the appropriate control system. The Incremental Nonlinear Control Allocation (INCA) method for control allocation is able to capture these effects in its control scheme. [18] showed that even in the presence of aerodynamic uncertainties the aircraft is controllable. The extent to which the aircraft is controllable has yet to be determined. By conducting research on new FTC methods for future high performance aircraft, in this work an answers to the question to which degree the ICE model aircraft is able to recover from a would be loss-of-control situation duo to effector failures is found.

The ICE aircraft model is a high fidelity model of a high performance aircraft. Its aerodynamic performance has been extensively tested. Because of its tailless configuration the stability of yaw control is hard to guarantee in critical flight manoeuvres and failure conditions. That is one of the reasons why innovative effector concepts were used on-board this aircraft such as the All-Moving-Wingtip (AMT) effectors and Spoiler-Slot Deflectors (SSDs). The flight control system (FCS) needed to properly control this aircraft has to be able to find the optimal control settings of 13 effectors combined to generate the 3 moments. This is a control allocation problem which was solved by using the INCA algorithm using Quadratic Programming (QP). It proved to be the most suitable and accurate solution to be performed in real-time using state-of-the-art zero-order continuity multi-variable simplex spline model for aerodynamic model identification. This model calculates the Jacobian of the control effectiveness to determine the effector deflection increments. The most common fault scenarios that were tested are stuck-in-place effector failures and hard-overs. The INCA method provided a optimal solution to update the control law depending on the effector failures for these effector failures. A possible alternative to update the control law can be on-line aerodynamic model identification, however this increased the computational complexity outside the scope of real-time use. By using a Fault Detection and Isolation (FDI) module that can detect the type of effector failure the INCA algorithm will be prevented or limited from using the defective effector(s). The benefit of using FDI has not been demonstrated in this paper. Furthermore the failure tests performed were mainly aimed at investigating the robustness of each effector for multiple flight manoeuvres, stability, reliability and availability were not investigated.

The robustness of the INCA method for fault tolerant control has been evaluated for stuck effectors in their maximum and minimum deflection positions on the high performance ICE aircraft model. By using a FDI module, the faulty effectors are detected and the control law is updated such that these effectors are not chosen by INCA. For the evaluation of the fault tolerant flight control system, benchmark flight trajectories have been defined to be able to compare the results obtained in this research to similar research efforts. To be able to automatically control the aircraft for all flight scenarios and test cases multiple autopilots were designed and tuned.

A sensitivity analysis using a variance in turbulence to investigate the model parameters of the trim conditions and time of failure show that the time of the fault and the trim condition have an impact on the degree of failure. For straight flight using an altitude and heading hold mode, combined with an auto-throttle control module the most critical effector failures to maintain straight flight are the SSD's. A hard-over failure to the maximum deflection position of either SSD will results in a loss-of-control event. At a lower altitude and velocity also the yaw thrust vectoring hard-over failure may result in a loss-of-control event. A different conclusion can be drawn for the evasive manoeuvre that was performed. For this scenario the SSD's are not the most critical effector failures but the Thrust Vectoring, in particular the thrust vectoring for longitudinal control. If the thrust vectoring is stuck in its position it is catastrophic for the aircraft during this flight manoeuvre. The SSDs are the second worst performer during the evasive manoeuvre to be stuck. But also the Left elevon and the AMTs can be critical. Overall almost for any hard-over during the turn in the evasive manoeuvre there is a chance of loss-of-control. However for most effectors there is a range of effector angles at which flight performance does not degrade as much as the hard-over failure cases. During the localizer hold mode and the glideslope the worst effects are the SSDs like the straight flight scenario. During all the flight trajectories, if one of the elevons is stuck at limit deflection the flight performance is moderately effected and the trajectory cannot be followed accurately using the designed autopilots only. The flight manoeuvres tested and the autopilots that were used showed that they both have combined impact on the performance during failures. Because flight manoeuvres were not changed after the failure event a huge potential lies in the design of tuning and testing of recovery manoeuvres that would prevent the loss-of-control events identified in this paper. By knowing which control effector failures are critical during a manoeuvre one can more easily change the course of action and thus increase the operation safety.

The overall flight performance of the ICE aircraft during single effector failures is in most cases robust enough to continue flying with the autopilot and controller settings for the manoeuvre. In the case hard-overs failures occur the SSDs, (yaw) TV, AMTs and elevons are the most critical effectors for all flight manoeuvres. Any hard-over during the evasive manoeuvre can results in a loss-of-control event and therefore to increase safety a recovery manoeuvre is recommended. The other manoeuvre require a lot less control effort and similar conclusions can be drawn between these manoeuvres.

Future directions and application can be automatic recovery trajectories following critical failure for each manoeuvre, i.e. for a maximum SSD failure in straight flight the flight control system could switch to a turning manoeuvre to prevent loss-of-control. Moreover one can investigate other types of effector failures that were not investigated in this paper. Improvements of FDI or the control laws used in this paper can be compared to the results obtained in this research. The effect of limiting effector deflection range and rate limits specified in table 2.2 on the operational range and the viability of using this to prevent loss-of-control events can be investigated as well. Another method one can try is to update the aerodynamic model in real-time, however note that computational complexity of the solution does have to be taken into account.

Bibliography

[1] Jovan D Boskovic, Ssu-Hsin Yu, and Raman K Mehra. A stable scheme for automatic control reconfiguration in the presence of actuator failures. In *American Control Conference, 1998. Proceedings of the 1998*, volume 4, pages 2455–2459. IEEE, 1998.

[2] A.J. Calise, S. Lee, and M. Sharma. Development of a reconfigurable flight control law for tailless aircraft. *Journal of Guidance, Control, and Dynamics*, 24(5):896–902, 2001.

[3] C. C. De Visser, J. A. Mulder, and Q. P. Chu. Global nonlinear aerodynamic model identification with multivariate splines. In *AIAA Atmospheric Flight Mechanics Conference*. No. AIAA-2009-5726, 2009.

[4] C. C. de Visser, J. A. Mulder, and Q. P. Chui. A multidimensional spline based global nonlinear aerodynamic model for the cessna citation ii. In *AIAA Atmospheric Flight Mechanics Conference*, 2010.

[5] C. C. de Visser, J. A. Mulder, and Q. P. Chu. Validating the multidimensional spline based global aerodynamic model for the cessna citation ii. In *AIAA Atmospheric Flight Mechanics Conference*, 2011.

[6] C.C. de Visser, Q.P. Chu, and J.A. Mulder. A new approach to linear regression with multivariate splines. *Automatica*, 45(12):2903 – 2909, 2009. ISSN 0005-1098. doi: https://doi.org/10.1016/j.automatica.2009.09.017.

[7] Fears S.P. Dorsett, K.M. and H.P. Houlden. Innovative control effectors (ice) phase ii, 1997.

[8] K.M. Dorsett and D.R. Mehl. Innovative control effectors (ice), 1996.

[9] Christopher Edwards, Thomas Lombaerts, Hafid Smaili, et al. Fault tolerant flight control. *Lecture Notes in Control and Information Sciences*, 399:1–560, 2010.

[10] Ola Harkegard. Efficient active set algorithms for solving constrained least squares problems in aircraft control allocation. In *Decision and Control, 2002, Proceedings of the 41st IEEE Conference on*, volume 2, pages 1295–1300. IEEE, 2002.

[11] J. Jiang and X. Yu. Fault-tolerant control systems: A comparative study between active and passive approaches. *Annual Reviews in Control*, 36(1):60–72, 2012.

[12] Eric N Johnson and Anthony J Calise. Pseudo-control hedging: A new method for adaptive control. In *Advances in navigation guidance and control technology workshop*, pages 1–2, 2000.

[13] Eric N Johnson and Suresh K Kannan. Adaptive trajectory control for autonomous helicopters. *Journal of Guidance Control and Dynamics*, 28(3):524–538, 2005.

[14] Quang Lam, Itzhak Barkana, and Willow Grove. Direct adaptive control treatment to flight control input saturation. In *To be Presented at the AIAA 2005 GN&C Conference, AIAA2005-6179*, 2005.

[15] T. J. J. Lombaerts, Q. P. Chu, J. A. Mulder, and D. A. Joosten. Real time damaged aircraft model identification for reconfiguring flight control. In *AIAA Atmospheric Flight Mechanics Conference*, volume 2, pages 1207–1231, 2007.

[16] T.J.J. Lombaerts, H.O. Huisman, Q.P. Chu, J.A. Mulder, and D.A. Joosten. Nonlinear reconfiguring flight control based on online physical model identification. *Journal of Guidance, Control, and Dynamics*, 32(3):727–748, 2009. doi: 10.2514/1.40788.

[17] P. Lu, E.-J. van Kampen, C. de Visser, and Q. Chu. Aircraft fault-tolerant trajectory control using incremental nonlinear dynamic inversion. *Control Engineering Practice*, 57:126–141, 2016. doi: 10.1016/j.conengprac.2016.09.010.

[18] Ismael Matamoros and Coen de Visser. Incremental nonlinear control allocation for a tailless aircraft with innovative control effectors. *Msc Thesis at Delft University of Technology*, 2017.

[19] M.A. Niestroy, K.M. Dorsett, and K. Markstein. A tailless fighter aircraft model for control-related research and development. In *AIAA Modeling and Simulation Technologies Conference*, 2017.

[20] John AM Petersen and Marc Bodson. Constrained quadratic programming techniques for control allocation. *IEEE Transactions on Control Systems Technology*, 14(1):91–98, 2006.

[21] J. Reiner, G.J. Balas, and W.L. Garrard. Flight control design using robust dynamic inversion and time-scale separation. *Automatica*, 32(11):1493–1504, 1996. doi: 10.1016/S0005-1098(96)00101-X.

[22] P. Simplício, M.D. Pavel, E. van Kampen, and Q.P. Chu. An acceleration measurements-based approach for helicopter nonlinear flight control using incremental nonlinear dynamic inversion. *Control Engineering Practice*, 21(8): 1065 – 1077, 2013. ISSN 0967-0661. doi: https://doi.org/10.1016/j.conengprac.2013.03.009. URL `http://www.sciencedirect.com/science/article/pii/S0967066113000634`.

[23] H. J. Tol, C. C. de Visser, and M. Kotsonis. Model reduction of parabolic pdes using multivariate splines. *International Journal of Control*, 0(0):1–16, 2016. doi: 10.1080/00207179.2016.1222554. URL `https://doi.org/10.1080/00207179.2016.1222554`.

[24] H.J. Tol, C.C. De Visser, E. Van Kampen, and Q.P. Chu. Nonlinear multivariate spline-based control allocation for high-performance aircraft. *Journal of Guidance, Control, and Dynamics*, 37(6):1840–1862, 2014. doi: 10.2514/1.G000065.

[25] H.J. Tol, C.C. De Visser, L.G. Sun, E. Van Kampen, and Q.P. Chu. Multivariate spline-based adaptive control of high-performance aircraft with aerodynamic uncertainties. *Journal of Guidance, Control, and Dynamics*, 39(4):781–800, 2016. doi: 10.2514/1.G001079.

[26] Ivo van der Peijl and Coen de Visser. Physical splines for aerodynamic modelling of innovative control effectors. *Msc Thesis at Delft University of Technology*, 2017.

[27] Y. Zhang and J. Jiang. Bibliographical review on reconfigurable fault-tolerant control systems. *Annual Reviews in Control*, 32(2):229–252, 2008. doi: 10.1016/j.arcontrol.2008.03.008.

A

Scientific paper

Benchmark Flight Scenarios for Testing Fault Tolerant Control in High Performance Aircraft

J.M. Bakker [*] and C.C. de Visser[†]
Delft University of Technology, Delft, 2600 GB, The Netherlands

The Innovative Effector Concept (ICE) aircraft model is a high performance aircraft. The aircraft is over-actuated and new control allocation algorithm has been designed previously to control this aircraft effectively: Incremental Nonlinear Control Allocation (INCA). Although, this control algorithm has been proven to be robust in case of aerodynamic uncertainty, it is unknown to what degree effector failures will effect aircraft performance. Hence, the main aim of this research is to investigate the performance of the over-actuated ICE aircraft model in presence of effector failures by varying failure and flight conditions. From the set of fault scenarios only actuator failures are considered in this research. A failure detection and isolation module (FDI) is build-in the control systems to detect such failures. New benchmark flight trajectories were defined for high performance aircraft performance testing. For control multiple autopilot were designed and tuned to automatically test all failure cases and manoeuvres. One such manoeuvre is to perform a 180 degree heading change within 10 seconds, another is to roll the aircraft 360 degrees within 1 second. Tests of single effector failures for each flight condition and failure condition show the degradation in performance of the aircraft. Furthermore, sensitivity analysis was conducted to test the influence of failure time and turbulence on the outcome of the performance for the most critical flight manoeuvre. Based on the results a few recommendations were made for future research in effector failure testing and potential recovery solutions.

I. Nomenclature

α = angle of attack
β = angle of sideslip
δ = deflection angle
Γ = glideslope error angle
γ = flight path angle
λ = localizer error angle
ϕ = roll angle
ψ = heading angle
τ = aerodynamic moment vector
θ = pitch angle
χ = ground track angle
$\dot{\omega}$ = angular rates vector
A = specific force
B = control effector matrix
C = force or moment coefficient
$c.g.$ = center of gravity
h = altitude (height)
I, J = moment of inertia
K = proportional gain
M = mach number

---

[*] MSc. Student, Control and Simulation Devision, Faculty of Aerospace Engineering, Kluyverweg 1, 2629HS Delft, The Netherlands,; jerry-m.b@live.nl, Student Member AIAA

[†] Assistant Professor, Control and Simulation Devision, Faculty of Aerospace Engineering, Kluyverweg 1, 2629HS Delft, The Netherlands; C.C.deVisser@tudelft.nl, Member AIAA

n = load factor
p, q, r = roll, pitch and yaw rate
R = slant range
u = control input vector
V = velocity
v = virtual control signal
W_d = allocation weighting matrix
W_u = control effort weighting matrix

II. Introduction

In aviation, as more and more aircraft are being flown every day, the number of accidents also increases. Analysing previous aviation accidents, it can be concluded that loss-of-control is one of the major causes as indicated in [1]. In these cases, the Flight Control System (FCS) was not able to cope with the effector failures which contributed to the loss-of-control. In an attempt to improve the operation safety of aircraft, a lot of research has been done on designing active Fault Tolerant Control (FTC) systems in the last three decades. The aim of such systems is to improve the reliability and availability of the aircraft to automatically accommodate component failures while maintaining a desired performance (stability). In the field of FTC, as indicated in [2], the main challenge is to combine the research on failure detection, failure isolation, state estimation in presence of failures to design a control system that can deal with multiple actuator failures or airframe failures. In the past decades a considerable amount of research has been done on system identification approaches [3] and nonlinear control approaches [4]. Recently a new model identification method, Spline based model identification [5–7], has been used in combination with Nonlinear Dynamic Inversion (NDI) [8] to allocate the controls of a high performance aircraft subject to aerodynamic uncertainties in [9, 10]. This research is an important step towards realizing a certifiable FTC system.

In the area of FTC, one can distinguish between Active Fault Tolerant Control (AFTC) and Passive Fault Tolerant Control (PFTC) methods. The main focus of this work will be on AFTC, mainly because PFTC provide limited fault-tolerant capabilities especially for increasing fault scenarios as indicated in [11] and [12]. AFTC approaches can further be classified into nonlinear and linear methods. Most control applications are nonlinear by nature but linear methods can be applied around the equilibrium points of the system. Common linear methods that are used are gain scheduling, Multiple Model (MM) and Sliding-Mode Control (SMC). Purely nonlinear approaches are feedback linearization, Nonlinear Dynamic Inversion (NDI), backstepping, Neural Networks (NN), nonlinear regulator and lyapunov methods. Compared to their linear counterpart, NDI and backstepping use the well-known equations of motions of the aircraft which are valid throughout the flight envelope, while gain scheduling and Linear Parameter-Varying (LPV) schemes are only designed for specific parts of the flight envelope. In most practical applications, these approaches are used in combination with each other to achieve the best overall FTC system. An historical overview of AFTC methods can be found in [12].

In this work, a nonlinear model of an over-actuated tail-less aircraft concept, the Innovative Control Effector (ICE) aircraft model, is used to investigate the performance of a newly developed control scheme, subject to multiple effector failures. The ICE program focuses on highly manoeuvrable fighter aircraft without vertical tails. Tailless aircraft are considered the next generation high performance aircraft, mainly because of the radar beam signature reduction as well as weight and drag reduction. Increased manoeuvrability and signature reduction requirements pose constrains on the geometry of the aircraft and on the controls required. To achieve RCS designs the vertical tail is removed, the vertical control surfaces are eliminated, and the control surface edges are aligned with external airframe edges. These adjustments from conventional shaped fighters contribute to the design of an interesting new control concepts to achieve the necessary manoeuvrability and beam signature reduction.

Over-actuated aircraft can use multiple effectors to achieve the required moments, controlling the effectors and position δ is left to the Control Allocation (CA) algorithm that is designed for the aircraft. This is a non-trivial task as the performance of the aircraft is greatly effected by whichever effector is used during any flight trajectory. CA algorithms that are commonly used are the pseudo-reverse, modified pseudo-reverse, direct allocation, constrained optimization method, fixed point method or a combination of the aforementioned methods. In recent research on the ICE aircraft model, a control scheme called Incremental Nonlinear Control Allocation (INCA) has been developed in order to deal with the nonlinearities and coupling between the control effectors [13]. While this research showed this method can deal with uncertainties in its aerodynamic model, it has yet to be shown to which degree the aircraft model can deal with effector and airframe failures. Apart from investigating the INCA model in case of actuator failures, this research aims to improve upon this control scheme by supplementing an adaptive control module based on a Fault Detection and Isolation (FDI) system. Furthermore, the most important task in this work is the design of flight scenarios and performance parameters. They are made to serve as a benchmark for future research on the ICE model or any other high performance aircraft model as effector failures are yet to be tested for high performance. No standard flight trajectories of these aircraft are defined, mainly because the capabilities of high performance aircraft and their mission requirements are not openly available and differ from that of commercial aircraft.

First, in section III the ICE aircraft model, the CA method and the FCS design needed for INCA is discussed. Second, the FTC system design is proposed in section IV followed by the autopilot design needed for the benchmark trajectories. The benchmark trajectories are defined in section VI, the testing results presented in section VII and finally, in section VIII, the conclusions and recommendations are provided.

III. Background

The objective of this work is to build a framework for testing FTCS for an innovative aircraft model. For this, the following state-of-the-art components are used in this work - ICE aircraft model, INCA and incremental FCS. In this section, we will briefly introduce these components which are used alongside the FTCS design. The ICE aircraft model is described in Section III.A. The control algorithm that has been developed for the ICE method is INCA, which is explained in Section III.B and the incremental flight control system design in Section III.C.

A. Innovative Control Effector Aircraft Model

Driven by the desire to design a more agile and less detectable fighter aircraft the ICE program was started in 1993 at the Air Force Research Laboratory. Research has shown that tailless aircraft can offer both, however new innovative controllers are necessary to provide sufficient control about the three axis (pitch, roll and yaw) as well as control techniques that can deal with complex nonlinearities. A high degree of coupling tend to exists aerodynamically between the controls for tailless configurations. The ICE program investigated a baseline vehicle and a couple of control concepts. Two baseline configurations were defined as shown in figure 1. An all-wing tailless land-based configuration with a 65-deg sweep delta wing and a carrier-based configuration which has a canard-delta planform with 42-deg leading edge sweep. The ICE aircraft concept is described in two technical papers [14, 15]. In these technical papers multiple configuration and new effectors were tested in wind tunnels, at a model scale.

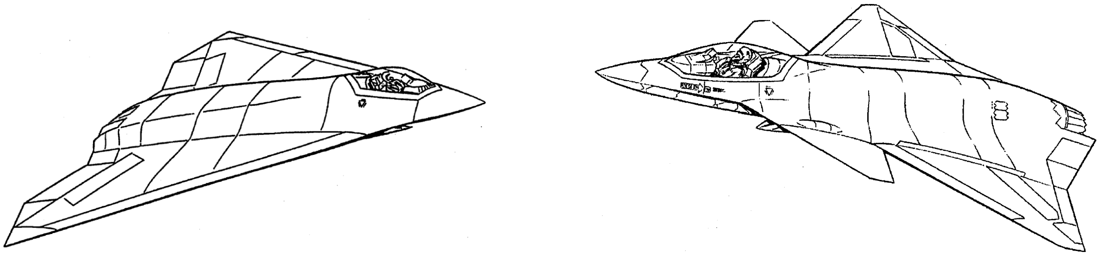

(a) The land-based baseline configuration (101-series) **(b) The carrier-based baseline configuration (201-series)**

Fig. 1 The baseline configurations considered in the ICE program [14, 15]

The aerodynamic data from a derived configuration of the all-wing tailless land-based 101-series baseline has been made available by Lockheed Martin Aeronautics in [16]. This model does not include actuator dynamics or an engine model. The configuration to which this model belongs has thirteen control effectors to control six Degree of Freedom (DOF), which can be considered a highly over-actuated aircraft. It is an all-wing tailless configuration employing a 65-deg sweep delta wing, single-engine, multi-role fighter aircraft with internal or low-observable weapons-carriage measures for reduced Radar Cross-Section (RCS) and supersonic capability. The aircraft is equipped with innovative control concepts: All-Moving Wing Tips (AMT), inboard and outboard Leading Edge Flaps (LEF), Spoiler-Slot-Deflector (SSD). Furthermore elevons and pitch flaps are used for pitch control and the aircraft is capable of pitch and yaw Thrust Vectoring (TV). Due to the data availability this configuration was used in this work. A rough sketch of the approximate locations of the control effectors used in the aircraft model is shown in figure 2 and the abbreviations used are given in table 1. The aerodynamic model consists of data covering a Mach number range between 0.1 and 2.16, an Angle of Attack (AOA) range of -4 deg to 90 deg, and a sideslip angle range from -30 deg to 30 deg.

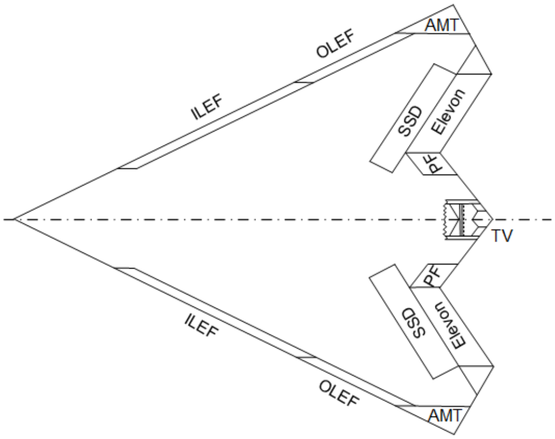

Fig. 2 ICE control effector approximate locations

Deflection abbreviation	Description
$LILEF$	left inboard leading edge flap
$LOLEF$	left outboard leading edge flag
$LSSD$	left spoiler slot deflector
LEL	left elevon
$LAMT$	left all moving wingtip
PF	pitch flap
$RAMT$	right all moving wingtip
$RSSD$	right spoiler slot deflector
$RILEF$	right inboard leading edge flap
$ROLEF$	right outboard leading edge flap
REL	right elevon

Table 1 Effector deflection abbreviations

Since the model does not come with an engine model or actuation model, the actuation can be represented by the transfer function in equation 1 for leading edge actuators and the transfer function in equation 2 for other actuators and the engine as introduced in [13].

$$\frac{(18)(100)}{(s+18)(s+100)} \tag{1}$$

$$\frac{(40)(100)}{(s+40)(s+100)} \tag{2}$$

In the model used in [16], the thrust (in x-, y- and z-direction) and the effectors (eleven deflections from the control surfaces and two from the TV) serve as input. The deflection limits and the rate limits of the eleven actuators and the two from TV are given in table 2.

Control effector	Deflection range limit (deg)	Rate Limit (deg/sec)
Inboard DLEF	0-40	40
Outboard DLEF	±40	40
Elevons	±30	150
Pitch flaps	±30	50
AMT	0-60	150
SSD	0-60	150
TV	±15	60

Table 2 Deflection and rate limits of the effectors and TV [14, 16]

B. Nonlinear Control Allocation

The aircraft model discussed in Section III.A is by itself not controllable. First, the required aerodynamic moments to perform any manoeuvre have to be translated to 13 control deflections and the required thrust. This is a nontrivial problem due to, over-actuation, the non-linearity and the coupling of the effectors. A successful solution proposed by Ismael Matamoros in [13] is called the Incremental Nonlinear Control Allocation (INCA) method. This method is further elaborated in this section as it lays the ground work for effector failure investigation. First, we briefly overview nonlinear control in incremental form, then show how this is can be used for control allocation as introduced in [13] and discuss the linear method to solve the control allocation problem.

Consider the aircraft dynamics expressed in the general form,

$$\dot{x}(t) = f(x) + g(x)\tau \tag{3}$$

where x is the state vector and τ represents the aerodynamic inputs, in this case the aerodynamic moments in the body frame. The aerodynamic moments can be separated into a state-dependent and an input-dependent part,

$$\tau = \tau_a + \tau_\delta \tag{4}$$

where τ_a contains the aerodynamic moments generated by the airframe and τ_δ by the control effector model, providing the control-induced moments produced by the actuators. The control effector model can be expressed as the nonlinear mapping,

$$\tau_\delta = \Phi(x, \delta) \tag{5}$$

Thus the system dynamics can be rewritten as,

$$\dot{x} = [f(x) + g(x)\tau_a] + g(x)\Phi(x, \delta) = F(x) + g(x)\Phi(x, \delta) \tag{6}$$

where the term $F(x)$ contains the moments not produced by the control effectors. In a discrete-time scheme, this equation can be linearized locally at every time step around the current state x_0 and the actuator positions δ_0 as a first-order Taylor expansion:

$$\dot{x} \approx \dot{x}_0 + \frac{\partial}{\partial x}\left[F(x) + g(x)\Phi(x, \delta)\right]\Bigg|_{\substack{\delta=\delta_0\\ x=x_0}} (x - x_0) + \frac{\partial}{\partial \delta}\left[F(x) + g(x)\Phi(x, \delta)\right]\Bigg|_{\substack{\delta=\delta_0\\ x=x_0}} (\delta - \delta_0) \tag{7}$$

The time scale separation principle states that for systems with the derivatives of the states with significantly faster dynamics than the states themselves the change in state $(x - x_0)$ is small enough to be neglected at a high sampling frequency. Applying the time scale separation and setting the virtual control input $v(x) = \dot{x}$ the simplified linearized system dynamics are,

$$v(x) = \dot{x} \approx \dot{x}_0 + g(x_0)\frac{\partial \Phi(x_0, \delta_0)}{\partial \delta}\Delta\delta \tag{8}$$

where $g(x_0)\partial(x_0, \delta_0)/\partial\delta$ is a control effectiveness Jacobian function that can be nonlinear in δ and include interactions between input variables. $\dot{x}_0$ is the time derivative of the state vector, which corresponds to the body angular accelerations. This can be obtained from direct measurement or state estimation methods.

The incremental nonlinear dynamic inversion becomes,

$$\Delta\delta_c = \left[\frac{\partial \Phi(x_0, \delta_0)}{\partial \delta}\right]^{-1} g(x)^{-1}[v(x) - \dot{x}_0] \tag{9}$$

This incremental control law provides the increments of the actuator position with respect to the current position vector δ_0, such that the new actuator position can be calculated as follow,

$$\delta_c = \delta_0 + \Delta\delta_c \tag{10}$$

In over-actuated systems the Jacobian $\partial(x_0, \delta_0)/\partial\delta$ is a non-square $p \times n$ matrix and therefore cannot be inverted to implement the incremental control law. However a control allocation scheme can be implemented by reformulating the control allocation problem in incremental form. The INCA problem is formulated as: given the current state x_0, the control control effector position δ_0, acceleration measurements $\dot{x}_0$ and a pseudo-control input command $d_c = g(x)^{-1}[v(x) - \dot{x}_0]$, determine an increment in the control input vector $\Delta\delta$ such that,

$$\frac{\partial \Phi(x, \delta)}{\partial \delta} = d_c \tag{11}$$

subject to $\underline{\Delta\delta} \leq \Delta\delta \leq \bar{\Delta}\delta$, which are the most restrictive upper and lower bounds of the local position and rate constraints of the actuators, translated into local incremental constraints. An overview of this proposed control scheme is shown in figure 3.

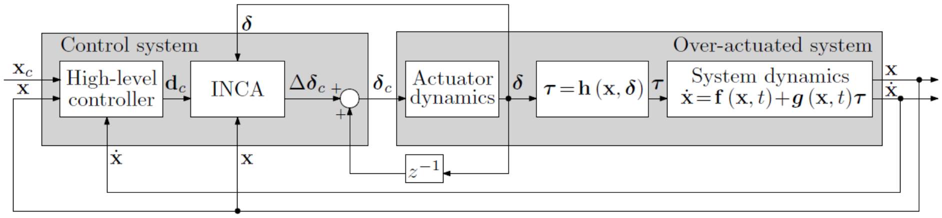

Fig. 3 Incremental nonlinear control allocation scheme for over-actuated systems[13]

The advantage of using INCA is that it is linear in actuator positions and therefore can be solved with simple and efficient linear methods such as Redistributed Weighted Pseudo-Inverse (RWPI) or Quadratic Programming (QP) and that using this solution there is no need for aerodynamic model identification.

For solving the control allocation problem with INCA, an active set-based QP solver was found to be most suitable as the active-set algorithm converges exactly to the optimal solution in a finite number of steps and is computationally efficient for small and medium size CA problems [17]. The active-set algorithm for QP was first introduced by [18]. The control allocation problem in general form is formulated as an l_2-norm cost function of the multi-objective constrained optimization problem,

$$\begin{aligned} \min_u J = & W_d|Bu - d_c|_2 + \epsilon W_u |u - u_p|_2 \\ \text{subject to} \quad & \underline{u} \leq u \leq \bar{u} \end{aligned} \tag{12}$$

where W_d and W_u are non-singular weighting matrices for the minimization of the allocation error and the minimization of the control effort respectively. ϵ is a sufficiently small scalar to prioritize the minimization of the allocation error $(Bu - d_c)$ over the secondary objective of minimizing $(u - u_p)$.

To use the algorithm presented in [18], the cost function defined in equation 12 is reformulated,

$$\begin{gathered} \min_u \left\| \begin{bmatrix} W_u B \\ \epsilon W_u \end{bmatrix} u - \begin{bmatrix} W_d d_c \\ \epsilon W_u u_p \end{bmatrix} \right\|_2 \\ \text{subject to} \quad Bu = d_c, \quad Cu \geq U \end{gathered} \tag{13}$$

where $C = [I - I]^T$ and $U = \left[\underline{u}\bar{u}\right]$. The active set algorithm solves a sequence of equality constrained problems, where in every iteration some inequality constraints are regarded as equality constraints and form a working set W, whereas the remaining inequality constraints are disregarded. The working set W at the optimum is known as the active set of the solution [18].

C. Incremental Flight Control System Design

The FCS for INCA as introduced in [13] consists of three additional modules besides the CA discussed in Section III.B: the Jacobian calculation of the control effectiveness matrix needed in INCA, inner-loop control module for rate control and Pseudo Control Hedging module to prevent actuator saturation. These modules combined with INCA are the incremental FCS design as shown in figure 4, which is used as the basis of the FTC design proposed in this work.

The **Jacobian model** $\frac{\partial \Phi(x,\delta)}{\partial \delta}$ used in [13] is based on a mutlivariate B-spline aerodynamic model of the ICE aircraft. The spline model was developed in [19] using the linear regression techniques presented in [20]. This spline model consists of 108 spline functions, corresponding to every dimensionless aerodynamic moment and force coefficient shown in Appendix A.

The directional derivatives of every coefficient $C^s_{i_x}$ in the aerodynamic model, where $i = \{X, Y, Z, L, M, N\}$ and x is the position of the derivative in the equation, to determine the Jacobian of the control effectiveness matrix can be calculated with a real-time efficiency in the order of 10^4 Jacobian calculation per second. This is done using a method for model reduction of parabolic partial differential equations presented in [21]. There are 108 spline models needed for every coefficient, each of these models will be partially differentiated by each control effector δ, which are 13 in total.

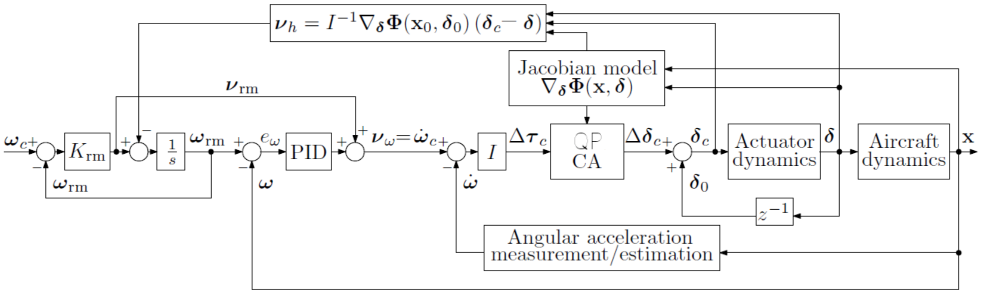

Fig. 4 Schematic of the INCA-based angular rate control system using PCH, Jacobian model and QP [13]

Using this the control effectiveness Jacobian matrix is defined as,

$$\frac{\partial \Phi(x,\delta)}{\partial \delta} = \begin{bmatrix} \sum_{j=1}^{18} \frac{\partial C^s_{l_j}(x,\delta)}{\partial \delta_1} & \sum_{j=1}^{18} \frac{\partial C^s_{l_j}(x,\delta)}{\partial \delta_2} & \cdots & \sum_{j=1}^{18} \frac{\partial C^s_{l_j}(x,\delta)}{\partial \delta_1 3} \\ \sum_{j=1}^{18} \frac{\partial C^s_{m_j}(x,\delta)}{\partial \delta_1} & \sum_{j=1}^{18} \frac{\partial C^s_{m_j}(x,\delta)}{\partial \delta_2} & \cdots & \sum_{j=1}^{18} \frac{\partial C^s_{m_j}(x,\delta)}{\partial \delta_1 3} \\ \sum_{j=1}^{18} \frac{\partial C^s_{n_j}(x,\delta)}{\partial \delta_1} & \sum_{j=1}^{18} \frac{\partial C^s_{n_j}(x,\delta)}{\partial \delta_2} & \cdots & \sum_{j=1}^{18} \frac{\partial C^s_{n_j}(x,\delta)}{\partial \delta_1 3} \end{bmatrix} \tag{14}$$

In [13], 0-order continuity was used to represent the worst-case scenario as well as the least computational complex solution.

For TV, the Jacobian matrix of τ_T is

$$\frac{\partial \tau_T(\delta_{ptv}, \delta_{ytv})}{\partial \delta_{tv}} = T \cdot d_n \begin{bmatrix} 0 & 0 \\ -\cos(\delta_{ptv}) & 0 \\ \sin(\delta_{ptv} \tan(\delta_{ytv}) & -\cos(\delta_{ptv})/\cos^2(\delta_{ytv}) \end{bmatrix} \tag{15}$$

The thrust vector arm, in incremental form, is subject to a circular constraint such that the new deflection increment has to be computed as,

$$\Delta\delta'_{tv} = \frac{\delta_{tv_{max}}}{|\delta_{tv_0} + \Delta\delta_{tv}|}(\delta_{tv_0} + \Delta\delta_{tv}) - \delta_{tv_0} \tag{16}$$

The **inner-loop** of the control system used in INCA is a body angular rate control loop. Consider the aircraft rotational dynamics, where τ_e is now replaced by the nonlinear control effector model $\Phi(x, \delta)$,

$$\dot{\omega} = J^{-1}(\tau - \omega \times J\omega) = J^{-1}\Phi(x,\delta) + J^{-1}(\tau_a - \omega \times J\omega) \tag{17}$$

For a given time step, the incremental form of the rotational dynamics as a first-order Taylor expansion at the operation point (x_0, δ_0) is,

$$\dot{\omega} = \dot{\omega}_0 + \frac{\partial}{\partial \omega}\left[J^{-1}\Phi(x,\delta) + J^{-1}(\tau_a - \omega \times J\omega)\right]\Bigg|_{\substack{\delta=\delta_0 \\ \theta=\theta_0}}(\omega - \omega_0) + \frac{\partial}{\partial \delta}\left[J^{-1}\Phi(x,\delta) + J^{-1}(\tau_a - \omega \times J\omega)\right]\Bigg|_{\substack{\delta=\delta_0 \\ \theta=\theta_0}}(\delta - \delta_0) \tag{18}$$

where the angular accelerations at the current step $\dot{\omega}_0$ can be obtained from angular accelerometers, signal processing or acceleration estimation methods.

Equation 17 can be simplified as the second term of the right-hand side is negligible for high sampling rates in comparison to the input-dependent term based on the time scale separation principle. Thus equation 17 becomes,

$$\dot{\omega} = \dot{\omega}_0 + J^{-1}\frac{\partial}{\partial \delta}\Phi(x_0, \delta_0)\Delta\delta \tag{19}$$

Setting the angular acceleration as a virtual control input $\nu_\omega(x) = \dot{\omega}$ and solving for $\Phi(x_0, \delta_0)\Delta\delta$, the INCA formulation in equation 11 becomes for the body angular rate control loop problem,

$$\Phi(x_0, \delta_0)\Delta\delta = I\left[\nu_\omega(x) - \dot{\omega}_0\right] = \Delta\tau_c \tag{20}$$

where the pseudo-control input d_c corresponds to the required increments of control-induced moments $\Delta\tau_c$.

To prevent actuator saturation, **PCH** was used for the INCA algorithm to shape the virtual control command $\nu_\omega(x)$ as proposed in [22]. PCH was already successfully implemented in [23, 24]. The reshaping of the reference signal is done as follows:

$$\nu_h(x) = \nu_\omega(x) - \hat{\nu}_\omega(x) \tag{21}$$

where $\nu_\omega(x)$ is the commanded virtual control and $\hat{\nu}_\omega(x)$ is the actual virtual control which is estimated with the actuator positions δ_0 as $\hat{\nu}_\omega(x) = f(x_0, \delta_0)$. $f(x, \delta)$ is the virtual control law and δ_0 is obtained through a feedback loop. The hedge signal $\nu_h(x)$ is fed back into a first-order reference model as a compensation signal. The reference model $\nu_{rm}(x)$ is,

$$\nu_{rm}(x) = K_{rm}(\omega_c - \omega_{rm}) \tag{22}$$

with K_{rm} a diagonal matrix. The hedge reference signal is the state vector of the reference model,

$$\omega_{rm} = \frac{1}{s}(\nu_{rm}(x) - \nu_h(x)) \tag{23}$$

When no saturation occurs, $\nu_h(x) = 0$ and the reference model behaves as a low-pass filter of bandwidth K_{rm}, for the i-th component of ω_{rm}. In case of actuator saturation the hedge signal $\nu_h(x)$ is used to reshape the reference input and avoid unfeasible commands. The reference model $\nu_{rm}(x)$ corresponds to the first-order derivatives of the commanded variables, which can be used a a feed-forward term added to $\nu_\omega(x)$ to improve tracking performance [25]. The virtual control law is given by,

$$\nu_\omega(x) = \dot{\omega}_0 + I^{-1}\frac{\partial\Phi(x_0, \delta_0)}{\partial\delta}(\delta - \delta_0) \tag{24}$$

Using equation 24 in 21, PCH is defined as:

$$\nu_h(x) = \left[\dot{\omega}_0 + I^{-1}\frac{\partial\Phi(x_0, \delta_0)}{\partial\delta}(\delta_c - \delta_0)\right] - \left[\dot{\omega}_0 + I^{-1}\frac{\partial\Phi(x_0, \delta_0)}{\partial\delta}(\delta - \delta_0)\right] \tag{25}$$

$$\nu_h(x) = I^{-1}\frac{\partial\Phi(x_0, \delta_0)}{\partial\delta}(\delta_c - \delta) \tag{26}$$

IV. Fault Tolerant Control System Design

FTC systems are an integral part of any aircraft model but as of now it has not been integrated in ICE. FTC systems are control systems that are able to accommodate for system component failures. They are capable of maintaining overall system stability and acceptable performance during such failures. FTC systems are mostly a combination of redundancy in the components and automation in the software that monitors the system behaviour. Faults are detected within this control system and appropriate actions are taken to mitigate the risks of critical failures. In this section, the fault scenarios used for ICE are discussed followed by the proposed FTC system design. An overview of the framework which incorporates the FTC with other components described in section III along with testing modules is shown in figure 5.

As mentioned in the introduction, AFTC method is used in this work instead of PFTC. AFTC approaches rely mostly on Fault Detection and Isolation (FDI) or Fault Detection & Diagnoses (FDD) schemes. Logically, it can be reasoned that the CA scheme for over-actuated aircraft is an AFTC system by itself and hence should not require a FDI scheme. The reasoning behind this hypothesis is as follows: The ICE aircraft model is inherently a nonlinear system and to be able to control this model in case of effector failures, a nonlinear fault tolerant control design is best suited. Along with these approaches one must select an appropriate CA algorithm to supplement these methods especially when the aircraft is over-actuated. This has been done successfully for ICE using INCA as explained in Section III.B. An inherent property of the control allocation method mitigates the risk of loss-of-control due to a single effector failure, i.e. not a single actuator of the ICE aircraft is solely responsible for the generation of one of the aerodynamic moments. Thus, the INCA flight control scheme can be considered to be an AFTC system by itself.

However knowledge about the failure scenario, which effector and the nature of the fault, is necessary to determine the correct effectiveness matrix B in equation 13 used for solving INCA. Erroneous B will result in control inputs allocated to an effector which does not or can only partly generate the necessary change in moment. Therefore, an FDI module has been added to the current INCA flight control scheme as shown in figure 5. Due to the unavailability of a

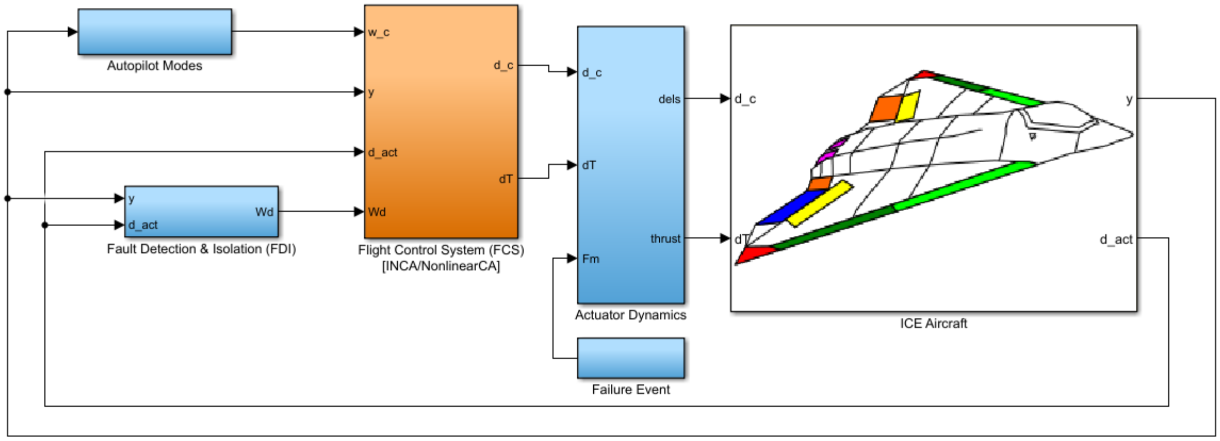

Fig. 5 Schematic of the FTC system design including the ICE, INCA, FDI, failure event and autopilot modules

working FDI module, this work investigates the performance of the ICE aircraft model against critical effector failures using the AFTC system under the assumption of perfect fault detection.

In general, there are different types of effector failures such as lock-in-place, hard-over, free floating, loss of effectiveness, missing control effector, loss of hydraulic power, etc. The FDI system is designed to detect only three effector faults due to the scope of this work and these faults are described below:

- *Lock-in-place* failure is a type of failure of the control effector when the effector freezes in a certain position and does not respond to subsequent commands. Such a failure introduces both constant and state-dependent disturbances into the overall closed-loop systems, whereby control reconfiguration is necessary for maintaining the stability and robustness of the system as shown in [26].
- *Hard-over* is a special case of freezing when the effector locks at its saturation position limit.
- *Loss of effectiveness* can occur due to (minor) structural damage loss. This means a slow or sudden decrease in the control effector gain, such that the same control signal results in a smaller control deflection compared to nominal airframe condition. One can try to accommodate the fault by increasing the control input gain, however this will increase the possibility of saturation.

AFTC of the model and/or flight control scheme has been successfully implemented in nonlinear flight scenarios. One such method involves deriving aerodynamic models of the possible fault scenarios beforehand while others try to update the aerodynamic model parameters in real-time. The former method requires more extensive wind-tunnel or prototype flight testing, while the latter requires extensive computational power for increased performance with nonlinear and over-actuated aircraft such as the ICE aircraft model. In this work, a third method is used where the aerodynamic model does not have to be updated but the flight control system itself is changed to increase fault tolerance. This can be achieved either by,

- Limiting effector deflection range and rate limits specified in table 2 or
- Adjusting the weight W_d assigned to the control effector for each effector as defined in equation 13

The first method can only be done with prior knowledge about the effect this limitation has on the operational range of the aircraft, while the latter can be applied immediately after determining the degradation of the control effectiveness of the effector using FDI. In this work, the second method has been implemented and tested whereas the first method is recommended for future research.

In [13], the preferred deflection in each time step and the weight W_d is used to determine the deflection rates and absolute positions of the effectors. Due to the change in weights proposed in this work, the preferred deflection also has to be updated. First, we re-introduce the preferred deflection defined in [13]. In discrete-time, the position limits over a time step Δt is defined with respect to the rate limit as

$$\begin{aligned} \Delta\delta^r_{max} &= \dot{\delta}_{max}\Delta t \\ \Delta\delta^r_{min} &= \dot{\delta}_{max}\Delta t \end{aligned} \tag{27}$$

Furthermore, the absolute deflection limit is expressed in local constraints in the time step Δt as

$$\begin{aligned} \Delta\delta^p_{max} &= \delta_{max} - \delta_0 \\ \Delta\delta^p_{min} &= \delta_{min} - \delta_0 \end{aligned} \tag{28}$$

The minimum and maximum deflection limit in time step Δt is chosen between the constraints due to the rate limits and those due to the absolute position as

$$\begin{aligned} \overline{\Delta\delta} &= \min\left(\Delta\delta^r_{max}\ ,\ \Delta\delta^p_{max}\right) \\ \underline{\Delta\delta} &= \max\left(\Delta\delta^r_{min}\ ,\ \Delta\delta^p_{min}\right) \end{aligned} \tag{29}$$

In [13], it has been observed that if the preferred position change in each time step is set to $\Delta\delta_p = 0$, complementary actuators diverge to asymmetric nonzero deflections while still producing a resulting moment of zero. To avoid this situation, the control effectors must attain their preferred absolute positions δ_p. Thus, the preferred incremental deflection at each time step is defined as

$$\Delta\delta_p = \min\Big(|\delta_p - \delta_0|, |\overline{\Delta\delta}|, |\underline{\Delta\delta}|\Big) \cdot \mathrm{sign}(\delta_p - \delta_0) \tag{30}$$

During lock-in-place and hard-over failures, the preferred absolute deflection cannot be attained anymore. Therefore, it is best to assign the failure position as preferred deflection position such that $\Delta\delta_p = 0$. However, this assignment alone is not sufficient in case all effectors are in their preferred position and a change in moment is required because the failed effector can still be chosen by the algorithm to provide the necessary change in moment. Therefore, the weight matrix W_δ which is responsible for assigning importance to certain effectors over others also needs to be updated. In straight flight, the weights in W_δ are set to 1 except for the SSDs. For SSDs, the weight is chosen as a function of AoA. This is because at low AoA, the control effectiveness of downstream effectors is negatively affected while at high AoA, the control effectiveness of trailing-edge devices is recovered by SSDs redirecting the airflow towards the upper wing skin. The W_δ for SSDs is defined in [13] as,

$$W_{\delta SSD}(\alpha) = [-0.25 + .35\exp(1.6\alpha)]^{-1} \tag{31}$$

At $\alpha = 0$, $W_{\delta SSD}$ is 10 and is 1 at $\alpha \approx 45$ deg.

In case of stuck-in-place or hard-over failure the effector is assigned a W_δ of 100. For partial loss of effectiveness, an exponential formula can be applied to assign W_δ. In normal conditions $W_\delta = 1$ and in the case where there is a total loss of effectiveness $W_\delta = 100$. The assumption is that a linear relationship is not beneficial because at a small loss of effectiveness the effector would still be functional. Given the effectiveness is denoted by δ_{eff} (in percentage), then the weight for the failing effector W_{δ_f} is defined as,

$$W_{\delta_f} = 0.955 + 0.005 \cdot \exp(0.1 \cdot (100 - \delta_{eff})) \tag{32}$$

At $\delta_{eff} = 100\%$, $W_\delta = 1$, at 50%, $W_{\delta_f} = 1.7371$ and at 10%, $W_{\delta_f} = 41.51$. Thus, for a stuck-in-place effector not only the preference position δ_p is adjusted to its failure position but also a penalty weight W_{δ_f} of 100 is assigned. At the FDI module the weights and preference deflection positions are determined based on the detected failures.

The flight control scheme is extended by allowing effector faults to occur using a switch function within the actuator dynamics block (see figure 5) to introduce the effector failure at failure time t_{fail}. Inside the switch function, the angle δ_{fail} of the effector can be set and is used to investigate stuck or hard-over failure cases set to specific angles. The FDI for the effector failures is assumed to have a perfect detection rate within 1 second after failure time t_{fail}.

V. Autopilot Design

The flight trajectories for testing are defined within the autopilot control module in figure 5. All trajectories require a predefined set of inputs for lateral and longitudinal flight control. The autopilots for lateral and longitudinal control is discussed in this section. An important part of this research is tuning the gains K_i used in the chosen inner and outer-loops of the FCS. Both lateral and longitudinal autopilots, an auto-throttle controller and a sideslip hold mode are used simultaneously. The autopilot modes are listed in table 3.

These autopilot modes are the outer-loops for the flight scenarios while the inner-loop is given by using the INCA methods including PCH control as shown in figure 3. The control schemes and the input and outputs for the six autopilots are:

Lateral	Longitudinal
Altitude Hold	Heading Hold
Glideslope Intercept	Localizer Intercept
Flight Path Angle Hold	Roll Angle Hold

Table 3 List of autopilot modes

1) The altitude hold mode is shown in figure 6. The inputs are the reference altitude h_{ref}, the actual altitude h_{act}, the pitch angle θ and the angle of attack α. The output is the commanded pitch rate $\dot{\theta}$. The altitude hold mode should be used only to keep the current altitude, not to initiate flight level changes.

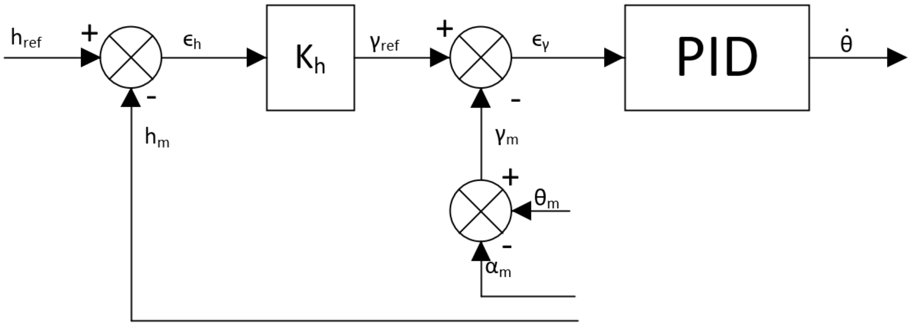

Fig. 6 Lateral Autopilot: Altitude Hold Mode control scheme

2) The flight path angle hold mode is shown in the latter part of altitude hold mode control system in figure 6. The input is the reference flight path γ_{ref} and the measured flight path $\gamma_m = \theta_m - \alpha_m$. The output is the commanded pitch rate $\dot{\theta}$.
3) The glideslope intercept control scheme is shown in figure 7. The glideslope error angle Γ should be zero. The glideslope path is the path defined by and angle of 3 degrees from the ground up. The distance of the aircraft to this path is d and the absolute range between the aircraft and the localizer is R. The deviation angle Γ is then,

$$\Gamma_m = \frac{1}{s} \cdot \frac{V_0(\gamma + 3)}{R} \cdot \frac{\pi}{180} \tag{33}$$

The output of the glideslope intercept is $\dot{\theta}$.

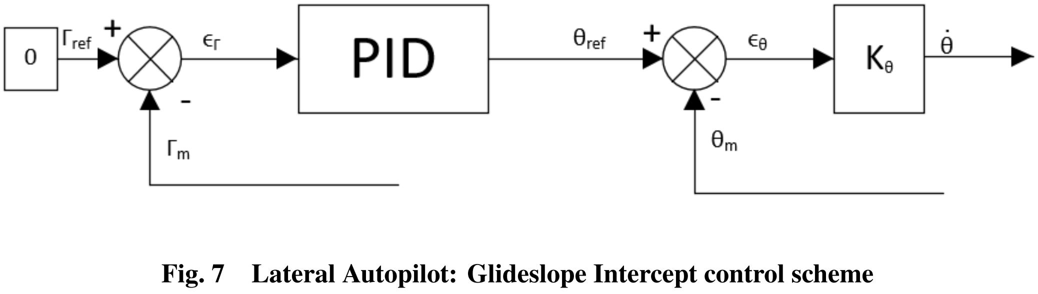

Fig. 7 Lateral Autopilot: Glideslope Intercept control scheme

4) The heading hold mode is shown in figure 8. The input is the reference heading ψ_{ref}, the actual heading ψ_{act} and the roll angle ϕ_{act}. The output is the commanded roll rate $\dot{\phi}$. Roll angles are allowed between −85 and 85 degrees, heading reference angle between 0 and 360 degrees.
5) In figure 9, the localizer intercept control scheme for longitudinal control is shown. The reference angle λ is the angle between the slant range R and the intended path. The slant range is the absolute distance from the aircraft

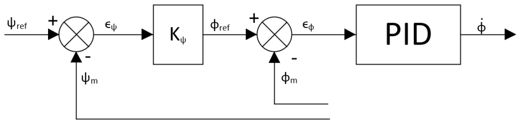

Fig. 8 Longitudinal Autopilot: Heading Hold control scheme

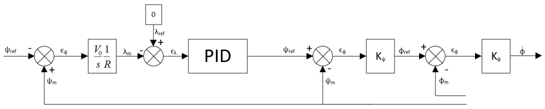

Fig. 9 Longitudinal Autopilot: Localizer Intercept control scheme

c.g. to the localizer transmitter. The localizer angle λ is defined as

$$\lambda = \operatorname{asin}\left(\frac{d}{R}\right) \approx \frac{d}{R} \tag{34}$$

where the deviation distance d is

$$d(s) = \frac{1}{s} V_0 \cdot (\psi_{act} - \psi_{airport}) \tag{35}$$

where the slant range R is the absolute distance between the localizer and aircraft c.g. The input is the reference localizer angle of $\lambda = 0$ and the position of the airport in relation to the aircraft. The output is the reference heading angle ψ_c.

6) The roll angle hold mode is shown in figure 10. The inputs are ϕ_{act} and ϕ_{ref}. The output is $\dot{\phi}$.

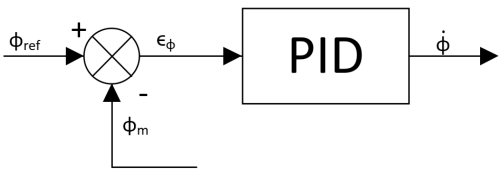

Fig. 10 Longitudinal Autopilot: Roll Angle Hold control scheme

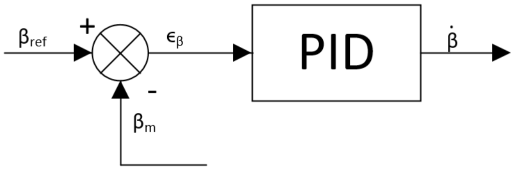

Fig. 11 Sideslip Angle Hold control scheme

Beside the six autopilots, an additional control loops is added to the flight control scheme. In figure 11, the sideslip angle hold mode control scheme is shown. The reference signal $\beta = 0$ throughout the simulation. The input is β_{act} and the output is $\dot{\beta}$.

VI. Benchmark trajectories

In this work, one of the main contribution is the four benchmark trajectories proposed for FTC testing for high performance aircraft. The trajectories are designed to test the robustness and performance of the ICE aircraft model under effector failure. The impact of a chosen flight trajectory on the flight performance is assumed to be significant. Besides varying the flight trajectory to measure flight performance, the impact of disturbances such as wind and different starting conditions are also evaluated.

A high performance aircraft such as the ICE aircraft model is designed for far more extreme flight conditions than any passenger aircraft. Any flight testing on these aircraft can thus only serve as a reference to the flight testing of the ICE aircraft. However, the performance characteristics of high performance aircraft is not readily available, so one can only estimate which flight manoeuvres are possible. Since little research is available on the flight trajectories of high performance aircraft, this research aims to set the benchmark scenarios of future performance tests to be able to more easily compare results obtained from this research to other research on the performance of these type of aircraft models.

The failure cases considered in this research are limited to lock-in-place and hard-overs, which means that at time t_{fail}, the effector will be locked in-place at a defined failure angle δ_{fail}. In this case, the connection between actuator and flight control system is cut off. Other than the failure type, the failure time also has an impact on the performance. It is likely that the same failure that occurs in straight flight and during a turn or evasive manoeuvre will result in a significant difference in flight performance measured. To prove this fact, a sensitivity analysis is done on the failure time. Another part of the sensitivity analysis is to investigate the effect of turbulence on the performance of the failed scenarios flown using the Dryden turbulence model.

Although there are currently no benchmark trajectories for fault tolerant control flight performance testing of high performance aircraft models in case of effector failures, there is one available for commercial aircraft in [27]. For high performance aircraft, these flight trajectories are also applicable. However, high performance aircraft have been designed for aggressive and evasive manoeuvres to be able to perform their missions. Therefore, two flight phases have been designed to reflect the full capabilities of these aircraft. One is an avoidance manoeuvre, a 180 degree turn within 10 seconds, while the other is a 270 degrees roll manoeuvre within 1 second. Although these time-frames will not be the minimum time-frames in which these actions can be performed, they are sufficiently aggressive for the tests in this research. The current model of the ICE aircraft does not include any additional turbulence model due to ground effect, therefore the final approach trajectory will not be included in this research and is left for future research. The full benchmark flight scenario for the qualification of the fault tolerant control system with four trajectories is shown in figure 12 and are described below.

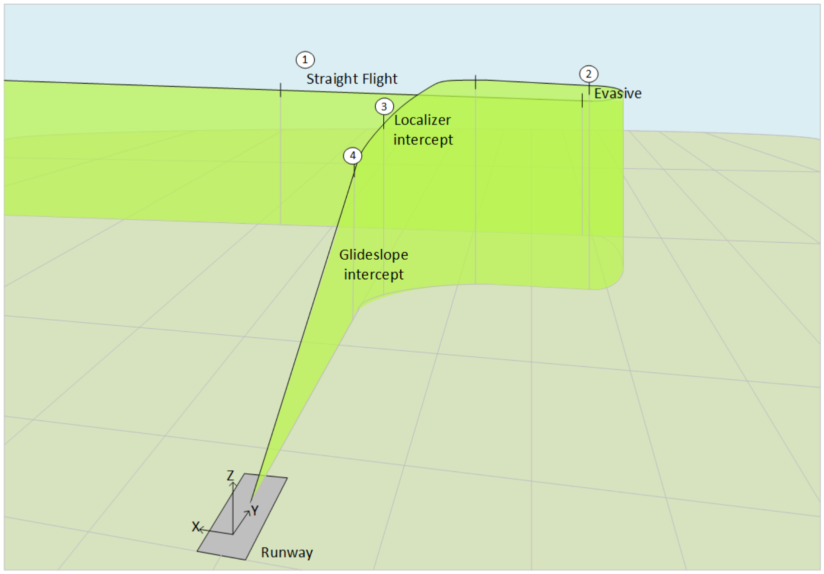

Fig. 12 Benchmark flight scenario for qualification of the INCA FTC system of the ICE aircraft model with effector failures.

1. Straight Flight

During straight flight, the altitude, flight speed and heading is kept constant using the Altitude Hold mode for lateral control, Heading Hold mode for longitudinal control and auto-throttle for constant airspeed. In table 4, the aircraft states are listed that are used to determine the performance between straight flight with and without failure. By analysing the closed loop system time responses, one can compare the quality of different control strategies. During this manoeuvre, the aircraft should remain within a predefined box like a tunnel in the sky.

2. Evasive manoeuvre

A 180 degree turn (change in heading) is performed to investigate to which degree mission specific manoeuvres can be flown in case of effector failure for high performance aircraft. This turn is followed by a 270 degree roll manoeuvre to quickly attain straight flight conditions. For the evasive manoeuvre a direct p and q rate control input is given, and a $\beta_{ref} = 0$ for Hold mode. Followed by straight flight using the previous discussed autopilot. In table 5, the assessment criteria for this manoeuvre are listed.

The turn itself is an upwards spiral manoeuvre. One criteria is that it should be performed within 10 seconds. Such a turn can only be achieved at a lower velocity than cruise velocity which is achieved by a sudden increase in angle of attack. The performance of this manoeuvre is evaluated in two phases, the first phase is the turn within 10 seconds and

Table 4 Aircraft state variables for straight flight

Symbol	Quantity
V	Velocity
γ	Flight path angle
α	Angle of attack
β	Sideslip angle
n_z	Load factor
ϕ	Roll angle

Table 5 Aircraft state variables for evasive manoeuvre

Symbol	Quantity
V	Velocity
p	Roll rate
q	Pitch rate
q	Yaw rate
α	Angle of attack
β	Sideslip angle
n_z	Load factor
A_y	Lateral Specific Force
ϕ	Roll angle

is evaluated by the change in heading. The second phase is the the roll manoeuvre to attain straight flight and the criteria that is measured specifically for this phase is the time it takes to return the aircraft to equilibrium conditions.

3. Left-hand turn and localizer intercept

A left hand turn is performed to get in range of the localizer of the nearest runway. For this manoeuvre, the Heading Angle Hold mode is used to turn towards the runway till the localizer intercept mode is engaged. In table 6, the aircraft state variables for this manoeuvre are listed.

Table 6 Aircraft state variables for left-hand turn and localizer intercept

Symbol	Quantity
λ	Localizer deviation during end
V	Velocity
p	Roll rate
q	Pitch rate
q	Yaw rate
α	Angle of attack
β	Sideslip angle
n_z	Load factor
A_y	Lateral Specific Force
ϕ	Roll angle

Table 7 Aircraft state variables for the glideslope intercept

Symbol	Quantity
λ	Localizer deviation
Γ	Glideslope deviation during end
V	Velocity
p	Roll rate
q	Pitch rate
q	Yaw rate
α	Angle of attack
n_z	Load factor

4. Glideslope intercept

When the aircraft is close enough to the airport, the glideslope intercept mode is engaged. The reference trajectory is given by a glideslope of 3 degrees. In table 7, the aircraft state variables for this manoeuvre are listed.

The flight trajectories described in this section will be used to assess the performance of the aircraft. The designed flight envelope limits for nominal aircraft operations, i.e. load limits, rotational rate limits, maximum and minimum velocity, can be used to identify catastrophic failures. After the failure event, the reference trajectories still have to be followed consecutively as shown in figure 12.

The two main evaluation criteria are,

- The operating limits of the aircraft may not be exceeded after failure
- The ability to reconfigure the controller such that the aircraft states are controlled with adequate performance

The performance can be measured by the time to reach equilibrium and the time to accomplish for manoeuvres where only an end-point is defined. The input commands and performance criteria are different for each flight trajectory as different autopilot (and gains) are used to complete the flight trajectories. Throughout all flight phases, the commanded speed is kept constant. The aircraft has been tuned per flight trajectory.

VII. Results and Discussion

The evaluation of the FTC performance of INCA using the autopilots designed in chapter V for the benchmark trajectories defined in VI was based on real-time simulation setup with the high-fidelity ICE model described in chapter III.A. The evaluation was done for the lock-in-place and hard-over effector failures for every flight trajectory. The metrics used to evaluate the performance of each failure were the tracking performance of the flight control system with respect to the failure free case and the severity of the failure bounded by load factor, maximum yaw rate and minimum velocity. First, a sensitivity analysis of the impact of the chosen simulation parameters, failure time and initial flight condition, is tested. Then the aircraft parameters and the control effector deflections are analysed for each flight trajectory.

In this section a sensitivity analysis for different types of experiment parameters is discussed in section VII.A and the performance of each trajectory in section VII.B.

A. Sensitivity Analysis

Using a sensitivity analysis, one can show the impact of model parameters such as the failure time and initial conditions on the results that are obtained. All the analysis in this section are performed only for the evasive manoeuvre and straight flight manoeuvre. Because the left hand turn is a much less demanding manoeuvre than the evasive manoeuvre and the glideslope intercept is a special case of straight flight with a small glide path angle and heading angle difference. The first part of the evasive manoeuvre is performed by providing control inputs directly to the inner loop. To initiate the turn a roll rate input p is given of 50 deg/s for 1 second and simultaneously a pitch rate command of 20 deg/s during 10 seconds while the sideslip input is kept at $\beta = 0$. After 10 seconds a 1.35 roll rate input of 200 deg/s is given to roll the aircraft around after the turn is finished. The second part starts at 16 seconds after the turn manoeuvre was initiated, the auto pilot system is engaged for altitude and heading control with $h_{ref} = h_{trim}$ and $\psi_{ref} = 180$ degrees. The straight flight manoeuvre is also controlled by the auto pilot with the altitude and heading control engaged at $h_{ref} = h_{trim}$ and $\psi_{ref} = 0$. The simulation length for all tests is 40 seconds not only to limit total simulation time for all tests but also because only a short simulation time is needed to analyse the robustness of the flight system for single manoeuvres.

1. Dryden turbulence model

The influence of turbulence is added with a Dryden Turbulence model. The settings were chosen with a wind speed of 5 ft/s at low-altitude, a medium/high altitude scale length of 1750 ft and the noise seed of $ug = 23341$, $vg = 23342$, $wg = 23343$, $pg = 2344$. The Dryden models uses the mathematical representation specified in the Military Specification MIL-F-8785C. The continuous Dryden Wind Turbulence Simulink Model block has been used to simulate the turbulence. Turbulence is used to determine to what degree the outcomes of the failures tests depend on the turbulence settings. For this purpose 20 realisations, 20 flights with varying noise seeds, of the same effector failure are run to determine the mean and the variance of the total RMS error between the fault free body rates and the effector failure case. The total RMS error is the addition of the RMS error of p, q and r between the failure free case and the failure case. A single manoeuvre where all effectors are tested in this way generates a total of 521 simulations to test 13 effectors for both the upper and lower limits. These 521 simulations are visualised in a single figure with both a boxplot to show the mean of the RMS error as well as a bar graph for those tests that failed before the end of the simulation. A simulation fails when the limit load factor of 20, a yaw rate higher than 200 deg/s, the minimum velocity or minimum altitude has been reached. No RMS error is recorded for failed flights but are visualised in the bar graph.

2. Failure time

To investigate the effect of failure time during the flight manoeuvre, two different failure times are compared to each other for the evasive manoeuvre case. A comparison of failure time for the straight flight manoeuvre is not performed as during normal operations of this manoeuvre no significant change is aircraft states are present between time T_0 and T_1. The standard failure time of $T_{fail} = 5$ is compared to the failure time of $T_{fail} = 11$, the second failure time occurs during the end of the fast roll manoeuvre while the standard failure occurs during the turning phase. An impression of the flight trajectory for every realisation is given in figure 13a and figure 13b. In both trajectory one can see that large

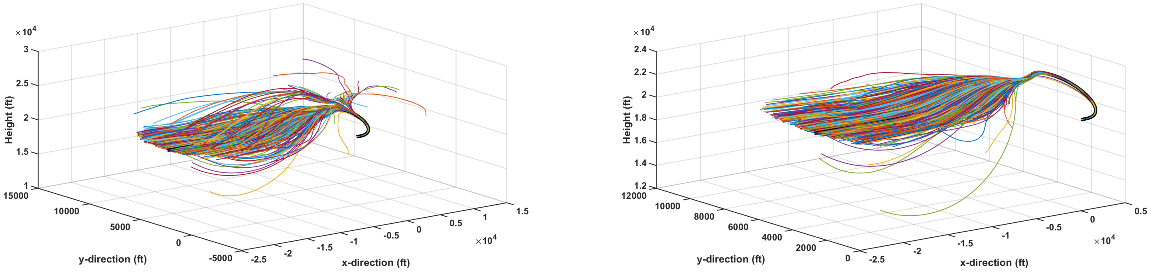

(a)

(b)

Fig. 13 Aircraft trajectories starting at trim conditions FL200 and target velocity of 880 ft/s of the evasive manoeuvre for all realisations with a) failure time $T = 5$ and b) failure time $T = 11$ during 40 seconds of simulation time of hard-over failure testing.

deviations from the nominal trajectory occurs close to time of failure. A closer look at the specific effectors can be seen in figure 14a for $T_{fail} = 5$ and in figure 14b for $T_{fail} = 11$. The failures case tested here is for hard-overs to find at which failure condition it is likely to find more realisations that stay within specified structural limits. A more in-dept analysis will be given for each critical effector in the next section of this chapter. Both figures show high RMS error and a failed realisations for the same effectors: SSDs, elevons and TV. The most significant difference is that the failure at 11 seconds has a greatly reduced tolerance to a hard-over of the left elevon at 15/20 realisations failed compared to the 5 seconds case where no realisation failed. A possible explanation is that the left elevon is used during the roll manoeuvre and at that time a hard-over causes a more significant flight trajectory change than the same failure during the turn at the failure time of 5 seconds.

3. Initial conditions

Another important parameter that has an impact on the flight performance is the starting condition, i.e. flight level and velocity, at which trim conditions have been established has an impact on which manoeuvres are possible due to effector failures. In this analysis the previously discussed trajectory at failure time $T = 5$ is compared at two different flight levels: FL200 and FL100. The failure cases are identical to the ones used in the failure time sensitivity analysis. For the evasive manoeuvre the results of this analysis are shown in figures 14b and figure 14c. What is noticeable is that at FL100 more flights fail and also almost every hard-over of any effector can cause failures compared to the FL200 case.

An initial condition analysis has also been performed for the straight flight manoeuvre. The angles used in this failure analysis are the maximum and minimum obtainable angles for each effector specified in table 2. The results are shown in figure 15a for FL200 and in figure 15b for FL100. From these figures it can be shown that the most critical effector failures occur for hard-over failures of the SSDs, AMTs and yaw TV. One significant change between FL200 and FL100 is that at FL100 yaw TV causes failures instead of the AMTs at FL200. This might indicate that at higher speed and altitude AMT is more critical and at lower speed and altitude the yaw TV for straight flight.

B. Trajectory Performance

Although a lot of results are obtained from each flight trajectory, only a chosen few are shown in this section to provide a clear overview. For each flight trajectory, the Root-Mean Square (RMS) error between the fault-free flight and flight with a failure is measured of the rotation rates p, q and r. The flights are then ordered from high to low based on the total RMS error of these rates. In the figures shown in this section, only the highest, lowest and the flights closest to the median of the RMS are shown. The normal flight is shown as a straight solid line. The 'worst-case' with the highest total RMS error flight is shown as the dashed line. The average total RMS error case is shown as the dotted line and the flight close to the fault-free case as the dash-dot line.

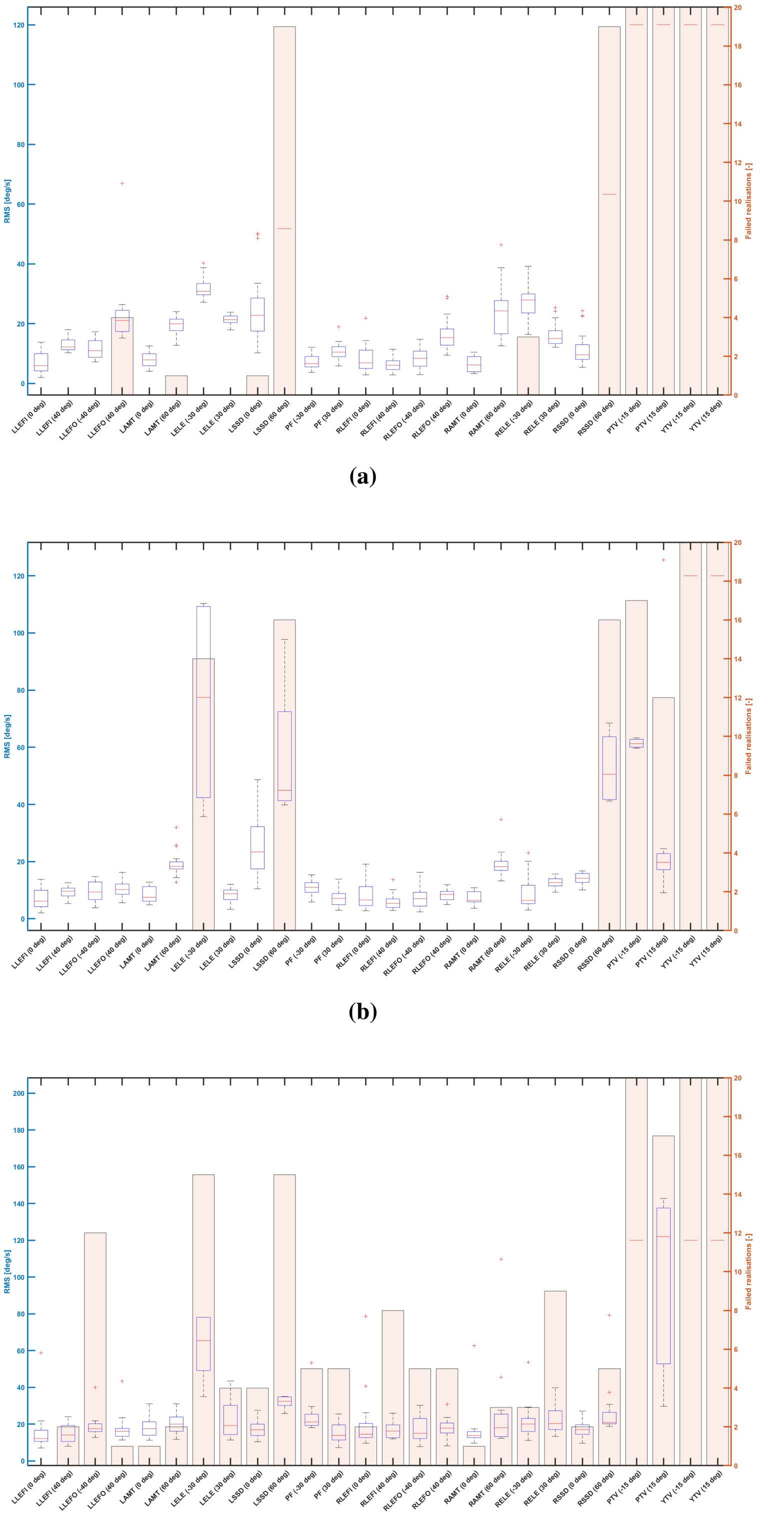

(a)

(b)

(c)

Fig. 14 The total RMS error between the realisations and the fault free flight case for each realisation shown in a boxplot for evasive flight of 40 seconds with FL200 and target velocity of 880 ft/s on the left y-axis and the corresponding failed realisations on the right y-axis in a) for failure time $T_{fail} = 5$ and in b) for failure time $T_{fail} = 11$ and in c) for failure time $T_{fail} = 5$ at FL100 instead of FL200.

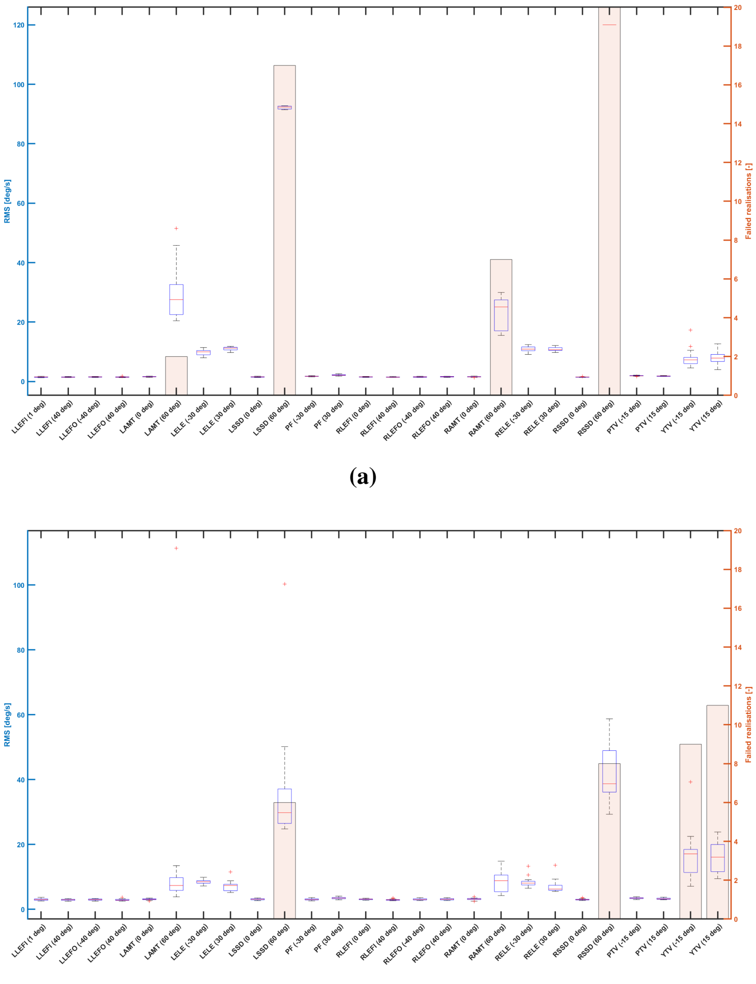

(a)

(b)

Fig. 15 The total RMS error between the realisations and the fault free flight case for each realisation shown in a boxplot for straight flight of 40 seconds on the left y-axis and the corresponding failed realisations on the right y-axis in a) for FL200 and in b) for FL100.

Straight flight

All flight manoeuvres tested start from trim conditions in straight flight. Straight flight is performed at a height of 20000 ft with $M = 0.85$ in trim conditions and the failure is introduced after 5 seconds. Starting with the limit deflections, both upper and lower limits, the scenario is flown for a duration of 40 seconds. Not all flights can be performed as the loads on the aircraft become unrealistically high. For the ICE aircraft, the limits loads are assumed to be $n_z > 20$ or $n_z < -20$ before the structural integrity of the aircraft is affected. For these failure cases the minimum or maximum allowable failure deflection has been determined. The aircraft trajectories are shown in figure 16a and the aircraft states for failures within these limits is shown in figure 16b. The RMS errors are shown for the highest, average and smallest RMS error in table 8.

In these figures, it can be seen that the 'worst case', where the LSSD is stuck at 59 degrees, can not be considered to be flying a straight level flight. An initial spike in the roll angle can be observed along with a large drop in speed and a constant high AOA during the first 15 seconds after failure. Although the load limits were not exceeded in this case, the aircraft is clearly not controllable with just the autopilots engaged. In case the RELE is stuck at -30 deg, much less noticeable aircraft states deviations are observed at failure time. However, the trajectory does diverge from the original heading due to the failure event.

In figure 17a, the thirteen aircraft effector deflections during straight flight are shown. In these figures the effector

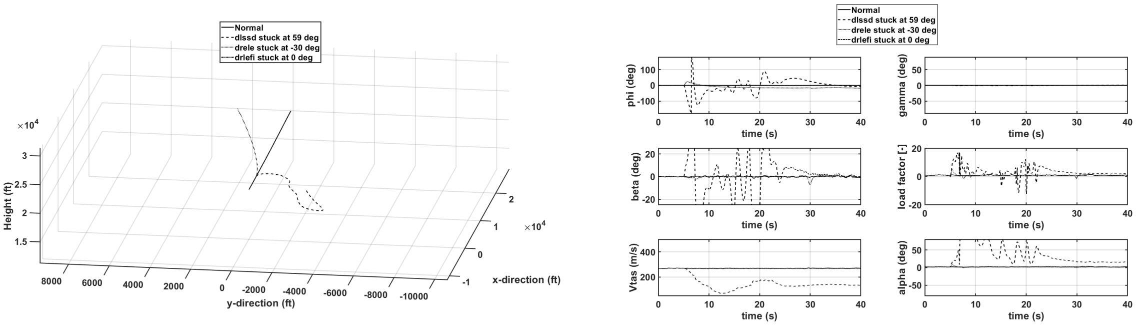

(a)

(b)

Fig. 16 Aircraft trajectory and aircraft states during the limit failures that are within structural limits for straight flight.

Performance	LSSD (59 deg)	RELE (-30 deg)	RLEFI (0 deg)
p [deg/s]	57.94	5.493	0.0006792
q [deg/s]	23.11	2.47	0.0009798
r [deg/s]	37.6	2.394	0.0003714
Total	118.6	10.36	0.00203

Table 8 RMS of the error between the normal straight flight manoeuvre and flights with failure shown for the highest, medium and smallest total RMS error

failure of the effectors can be seen and how the control effort of failed flights is much larger than of the fault-free case. As well as near saturation of the pitch flap from the average failure case and right side saturation of the Right LEFO and Right ELE in the worst case.

Evasive manoeuvre

The 180 degrees turn within 10 seconds is performed from straight flying conditions as defined previously. At time $T = 5$, the effector failure occurs and at time $T = 10$, the manoeuvre should be finished. To return to straight flight, a 270 degree roll manoeuvre is performed at time $T = 10$. The trajectories of the flights are shown for the combined manoeuvre in figure 18a and the states are shown in figure 18b. The RMS errors are shown for the highest, average and smallest RMS error in table 9.

Performance	RAMT (30 deg)	RELE (-30 deg)	LSSD (1 deg)
p [deg/s]	44.92	29.34	18.93
q [deg/s]	16.28	7.775	1.793
r [deg/s]	12.81	8.85	2.896
Total	74.02	45.96	23.62

Table 9 RMS of the error between the normal evasive manoeuvre and flights with failure shown for the worst, medium and smallest total RMS error

In these figures, one can see that both the worst case, LAMT stuck at 38 degree, and the average case, RELE stuck at -30 degree, diverge by large margin from the fault-free scenario. This is caused by the failure which resulted in spikes at different time for these two failure cases of β and α. The effector deflections belonging to this manoeuvre are shown in

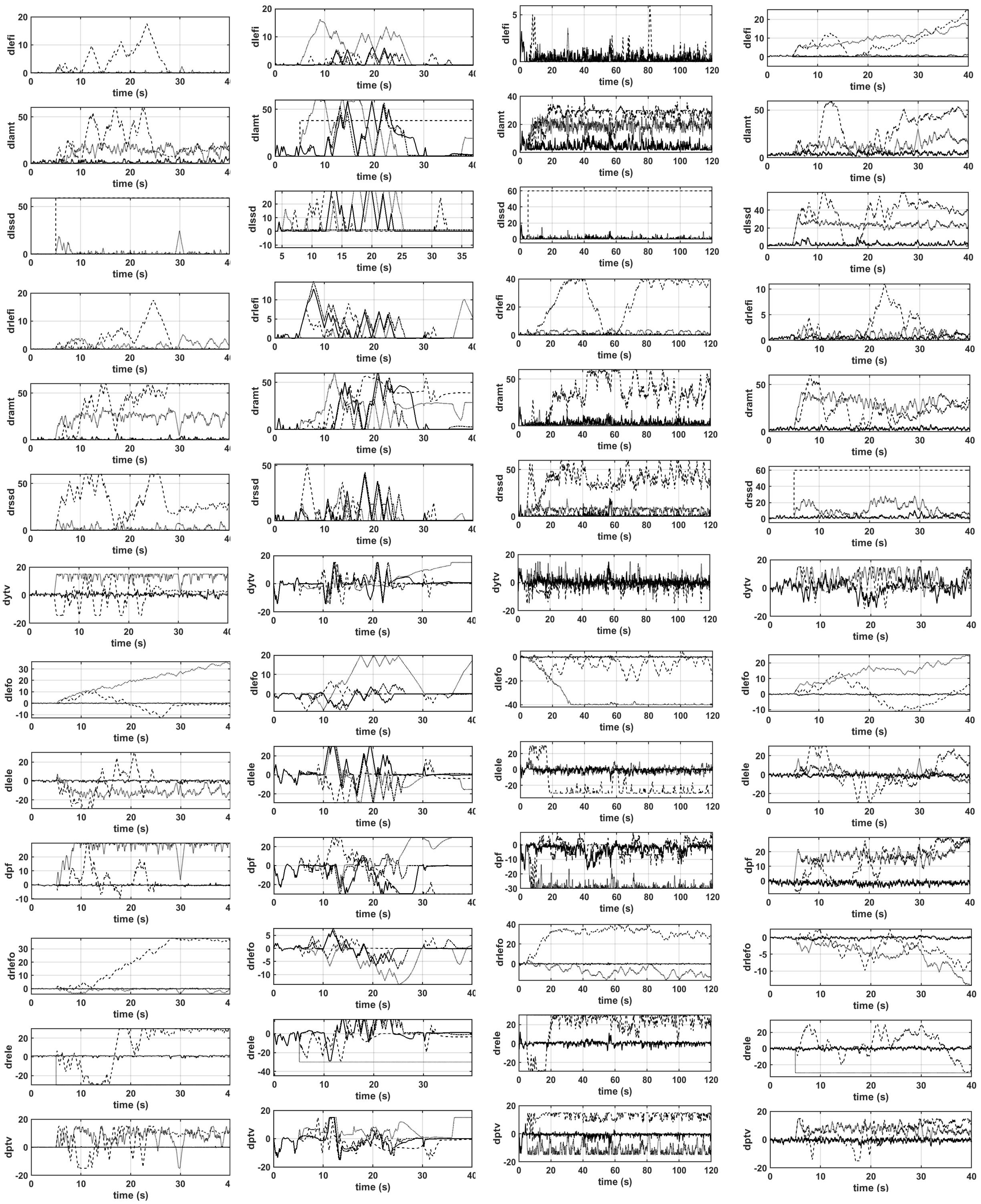

(a) **(b)** **(c)** **(d)**

Fig. 17 Aircraft effector deflections during (a) the limit failures that are within structural limits for straight flight, (b) a 180-degree turn within 10 seconds followed by a 270 degree roll and straight flight of the tested limit cases, (c) the left hand turn and localizer hold mode of the tested limit cases, and (d) glideslope of the tested limit cases.

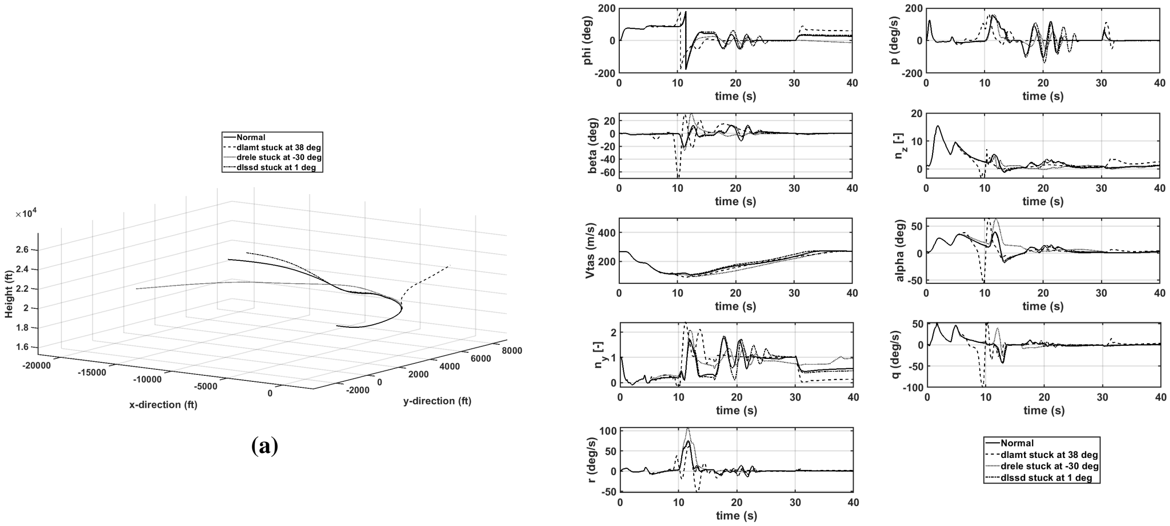

(a)

(b)

Fig. 18 Aircraft trajectory and aircraft states of a 180-degree turn within 10 seconds followed by a 270 degree roll and straight flight of the tested limit cases.

figure 17b.

From these figures it can be seen that this manoeuvre requires quite a bit of control effort even without effector failure. For the worst and average case, the pitch flap is saturated at the end of the manoeuvre. For the average case, the TV in both directions gets saturated at the end as well.

1. Left hand turn & localizer

This manoeuvre is tested starting at trim conditions at $FL = 100$, with 440 ft/s. For the first 40 seconds the heading angle hold mode is activated for a 280 degree heading and the altitude hold mode at 10000 ft. At 40 seconds the localizer is engaged as the aircraft enters the airports range. With a runway at 270 degrees at (4500ft, -100,000ft). The simulation is run for 120 seconds. The flight trajectory is shown in figure 19a. It can be seen that for the case where the LSSD is stuck at 60 degrees the normal flight trajectory can not be followed adequately. In figure 19b, the aircraft state variables are shown. The RMS errors are shown for the highest, average and smallest RMS error in table 10.

Performance	**LSSD (60 deg)**	**RELE (30 deg)**	**LEFI (0 deg)**
p [deg/s]	12.04	1.653	0.02026
q [deg/s]	6.876	1.367	0.01156
r [deg/s]	6.178	0.7615	0.007722
Total	25.09	3.782	0.03954

Table 10 RMS of the error between the normal localizer intercept manoeuvre and flights with failure shown for the highest, medium and smallest total RMS error

The initial spike in α and β causes the trajectory to change drastically. During the mode change a spike in ϕ and p can be observed, this is due to the sudden change in heading reference. In figure 17c, the effector deflections are shown during this manoeuvre.

From these deflections, it can be seen that for the worst case with the LSSD stuck at 60 degrees, a large control effort is asked from the right-side control effectors to compensate for this. For the case the RELE is stuck at 30 degrees, most compensation is asked of the PF and the LAMT as well as pitch TV.

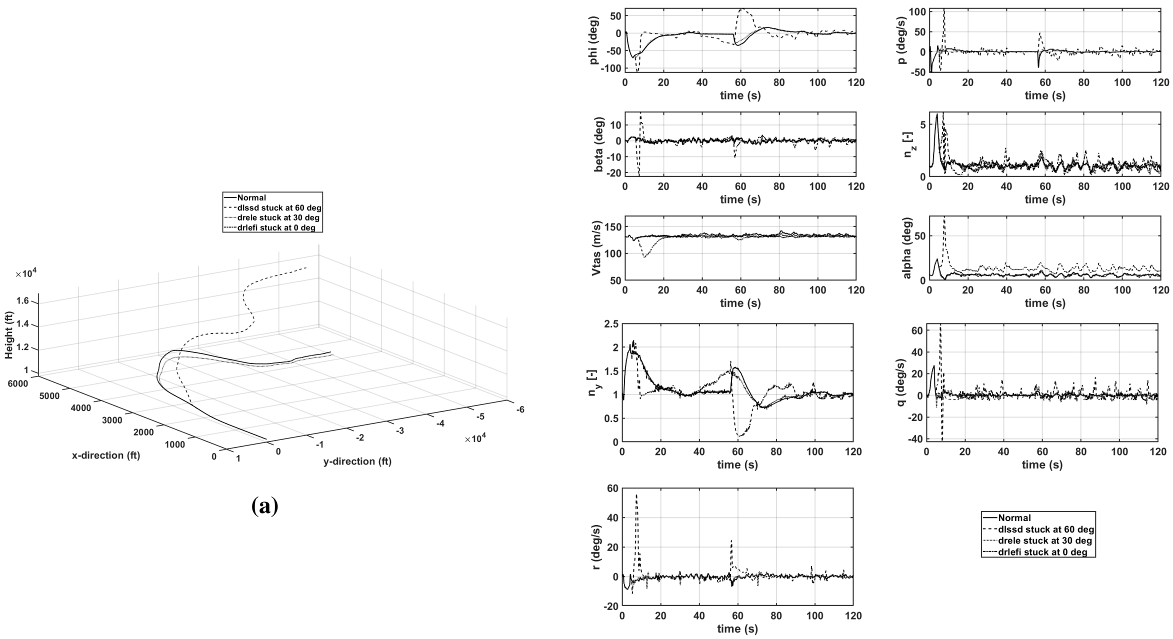

(a)

(b)

Fig. 19 Aircraft trajectory and aircraft states of the left hand turn and localizer hold mode starting at FL100 with 440ft/s for 120 seconds of the tested limit cases.

Glideslope

Like the Localizer Hold mode the Glideslope is tested at FL=100 for 440ft/s. This time it is the RSSD instead of the LSSD that has the highest RMS error. In figure 20a the Glideslope trajectory is shown.

It can be seen that a stuck RSSD of 60 degree does not follow the glideslope at all. While the average RMS error case, the RELE stuck at -30 degree, is not far off. The aircraft states confirm that mainly the worst case causes a large deviation from fault-free aircraft states as shown in figure 20b. The RMS errors are shown for the highest, average and smallest RMS error in table 11.

Performance	RSSD (60 deg)	RELE (-30 deg)	RLEFI (0 deg)
p [deg/s]	34.96	4.619	0.04157
q [deg/s]	24.76	2.656	0.02473
r [deg/s]	15.59	2.095	0.03048
Total	75.31	9.371	0.09678

Table 11 RMS of the error between the normal glideslope manoeuvre and flights with failure shown for the highest, medium and smallest total RMS error

In this table it can be seen that the highest RMS error is caused by roll rate control and that the total RMS of the RSSD at 60 degrees is at least 8 times higher than the RMS of the RELE at -30 degrees. The effector deflections during the glideslope are given in figure 17d. In these figures, the effect on the control allocation due to the failure is shown by large deflections of the SSDs and AMTs after failure time t_{fail}.

All trajectories have been tested and the most critical effectors during each trajectory was identified. Because this aircraft has not been build yet, it is interesting to compare the criticality of the effectors identified during the design phase to the simulated criticality of the effectors in this paper. In [14], actuator redundancy is discussed and a ranking system is made of the criticality of combined actuator failures in order to determine which effectors would require dual hydraulic systems, an example is shown in figure 21. This information shows that during the design the yaw TV, SSD

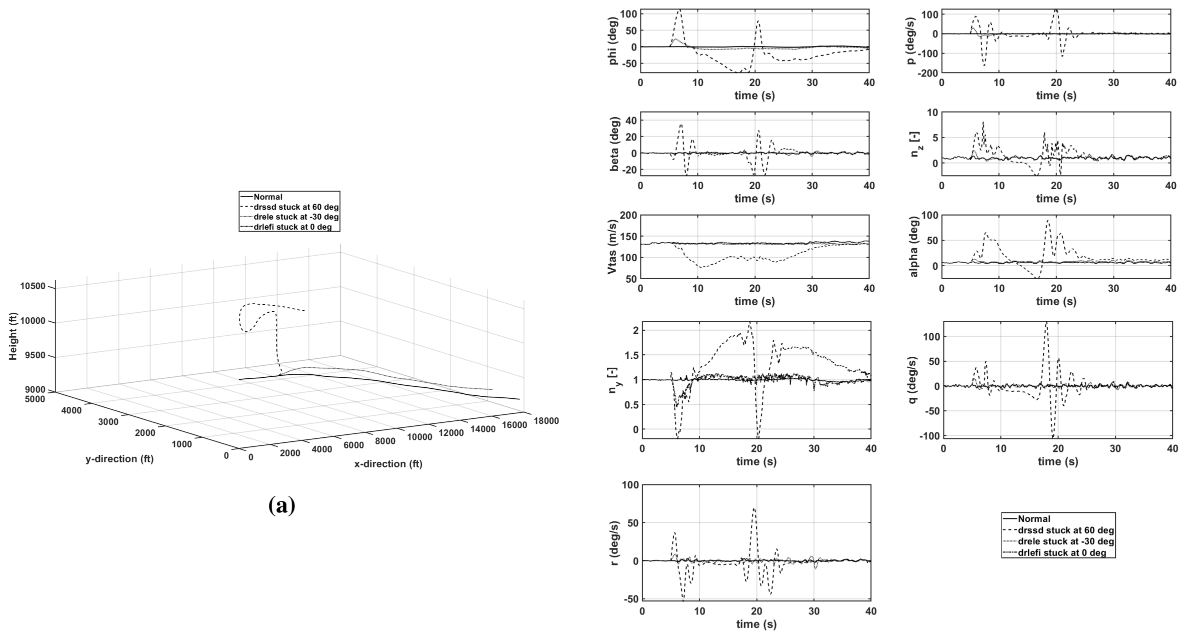

(a)

(b)

Fig. 20 Aircraft trajectory and aircraft states of the glideslope starting at FL100 with 440ft/s for 40 seconds of the tested limit cases.

and Elevons were already found to be the most critical. However the AMT were not evaluated in this criticality matrix, but in this paper it was shown that they do have a big impact on the performance during evasive manoeuvres.

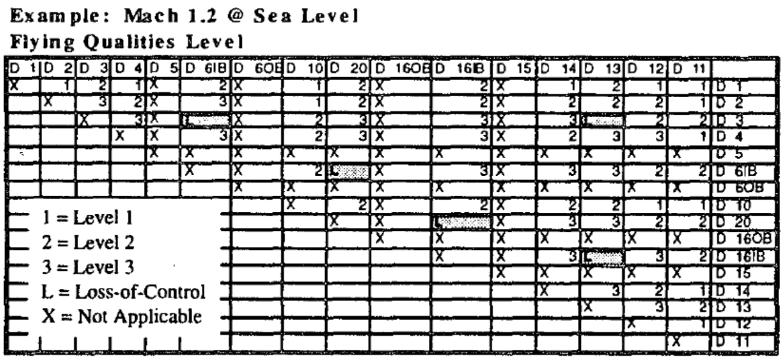

Example: Mach 1.2 @ Sea Level
Flying Qualities Level

D 1	D 2	D 3	D 4	D 5	D 6IB	D 6OB	D 10	D 20	D 16OB	D 16IB	D 15	D 14	D 13	D 12	D 11	
X	1	2	1	X	2	X	1	2	X	2	X	1	2	1	1	D 1
	X	3	2	X	3	X	1	2	X	2	X	2	2	2	1	D 2
		X	3	X	L	X	2	3	X	3	X	3	L	2	2	D 3
			X	X	3	X	2	3	X	3	X	2	3	3	1	D 4
				X	X	X	X	X	X	X	X	X	X	X	X	D 5
					X	X	2	L	X	3	X	3	3	2	2	D 6IB
						X	X	X	X	X	X	X	X	X	X	D 6OB
							X	2	X	2	X	2	2	1	1	D 10
								X	X	L	X	3	3	2	2	D 20
									X	X	X	X	X	X	X	D 16OB
										X	X	3	L	3	2	D 16IB
											X	X	X	X	X	D 15
												X	3	2	1	D 14
													X	3	2	D 13
														X	1	D 12
															X	D 11

1 = Level 1
2 = Level 2
3 = Level 3
L = Loss-of-Control
X = Not Applicable

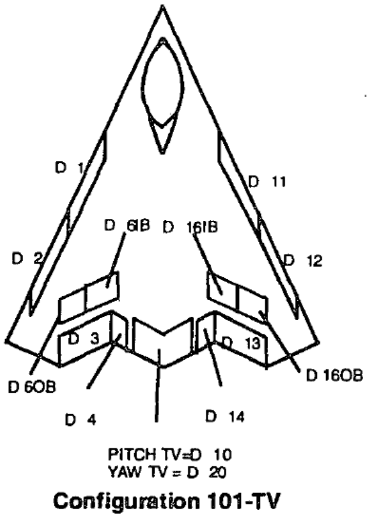

Fig. 21 Example Control Surface Criticality Matrix 101-series [14]

VIII. Conclusion and recommendation

In this paper the robustness of the INCA method for fault tolerant control has been evaluated for stuck effectors in their maximum and minimum deflection positions on the high performance ICE aircraft model. By using a FDI module, the faulty effectors are detected and the control law is updated such that these effectors are not chosen by INCA. For the evaluation of the fault tolerant flight control system, benchmark flight trajectories have been defined to be able to compare the results obtained in this research to similar research efforts. To be able to automatically control the aircraft for all flight scenarios and test cases multiple autopilots were designed and tuned.

A sensitivity analysis of turbulence, trim conditions and time of failure shows that turbulence barely effect the performance, however the time of the fault and the trim condition does have a large impact. For straight flight using an altitude and heading hold mode, combined with an auto-throttle control module the most critical effector failures to maintain straight flight are the SSD's. A run-a-way failure to the maximum deflection position of either SSD will results in a loss-of-control event. A different conclusion can be drawn for the evasive manoeuvre that was performed. For this scenario the SSD's are not the most critical effector failures but the Thrust Vectoring, in particular the thrust vectoring for longitudinal control. If the thrust vectoring is stuck in its position it is catastrophic for the aircraft during this flight manoeuvre. The SSD, AMT and elevons are the second worst performers during the evasive manoeuvre to be stuck. During the localizer hold mode and the glideslope the worst effects are the SSDs like the straight flight scenario. During all the flight trajectories, if one of the elevons is stuck at limit deflection the flight performance is moderately effected and the trajectory cannot be followed accurately using the designed autopilots only.

Future directions and application can be automatic recovery trajectories following critical failure for each manoeuvre, i.e. for a maximum SSD failure in straight flight the flight control system could switch to a turning manoeuvre to prevent loss-of-control. Moreover one can investigate other types of effector failures that were not investigated in this paper. Improvements of FDI or the control laws used in this paper can be compared to the results obtained in this research. The effect of limiting effector deflection range and rate limits specified in table 2 on the operational range and the viability of using this to prevent loss-of-control events can be investigated as well. Another method one can try is to update the aerodynamic model in real-time, however note that computational complexity of the solution does have to be taken into account.

References

[1] Lombaerts, T., Huisman, H., Chu, Q., Mulder, J., and Joosten, D., "Nonlinear reconfiguring flight control based on online physical model identification," *Journal of Guidance, Control, and Dynamics*, Vol. 32, No. 3, 2009, pp. 727–748. doi:10.2514/1.40788.

[2] Calise, A., Lee, S., and Sharma, M., "Development of a reconfigurable flight control law for tailless aircraft," *Journal of Guidance, Control, and Dynamics*, Vol. 24, No. 5, 2001, pp. 896–902.

[3] Lombaerts, T. J. J., Chu, Q. P., Mulder, J. A., and Joosten, D. A., "Real time damaged aircraft model identification for reconfiguring flight control," *AIAA Atmospheric Flight Mechanics Conference*, Vol. 2, 2007, pp. 1207–1231.

[4] Lu, P., van Kampen, E.-J., de Visser, C., and Chu, Q., "Aircraft fault-tolerant trajectory control using Incremental Nonlinear Dynamic Inversion," *Control Engineering Practice*, Vol. 57, 2016, pp. 126–141. doi:10.1016/j.conengprac.2016.09.010.

[5] De Visser, C. C., Mulder, J. A., and Chu, Q. P., "Global nonlinear aerodynamic model identification with multivariate splines," *AIAA Atmospheric Flight Mechanics Conference*, ???? No. AIAA-2009-5726, 2009.

[6] de Visser, C. C., Mulder, J. A., and Chui, Q. P., "A multidimensional spline based global nonlinear aerodynamic model for the Cessna Citation II," *AIAA Atmospheric Flight Mechanics Conference*, 2010.

[7] de Visser, C. C., Mulder, J. A., and Chu, Q. P., "Validating the multidimensional spline based global aerodynamic model for the cessna citation II," *AIAA Atmospheric Flight Mechanics Conference*, 2011.

[8] Reiner, J., Balas, G., and Garrard, W., "Flight control design using Robust dynamic inversion and time-scale separation," *Automatica*, Vol. 32, No. 11, 1996, pp. 1493–1504. doi:10.1016/S0005-1098(96)00101-X.

[9] Tol, H., De Visser, C., Van Kampen, E., and Chu, Q., "Nonlinear multivariate spline-based control allocation for high-performance aircraft," *Journal of Guidance, Control, and Dynamics*, Vol. 37, No. 6, 2014, pp. 1840–1862. doi:10.2514/1.G000065.

[10] Tol, H., De Visser, C., Sun, L., Van Kampen, E., and Chu, Q., "Multivariate spline-based adaptive control of high-performance aircraft with aerodynamic uncertainties," *Journal of Guidance, Control, and Dynamics*, Vol. 39, No. 4, 2016, pp. 781–800. doi:10.2514/1.G001079.

[11] Jiang, J., and Yu, X., "Fault-tolerant control systems: A comparative study between active and passive approaches," *Annual Reviews in Control*, Vol. 36, No. 1, 2012, pp. 60–72.

[12] Zhang, Y., and Jiang, J., "Bibliographical review on reconfigurable fault-tolerant control systems," *Annual Reviews in Control*, Vol. 32, No. 2, 2008, pp. 229–252. doi:10.1016/j.arcontrol.2008.03.008.

[13] Matamoros, I., and de Visser, C., "Incremental Nonlinear Control Allocation for a Tailless Aircraft with Innovative Control Effectors," *Msc Thesis at Delft University of Technology*, 2017.

[14] Dorsett, K., and Mehl, D., "Innovative Control Effectors (ICE)," , 1996.

[15] Dorsett, F. S., K.M., and Houlden, H., "Innovative Control Effectors (ICE) Phase II," , 1997.

[16] Niestroy, M., Dorsett, K., and Markstein, K., "A tailless fighter aircraft model for control-related research and development," *AIAA Modeling and Simulation Technologies Conference*, 2017.

[17] Petersen, J. A., and Bodson, M., "Constrained quadratic programming techniques for control allocation," *IEEE Transactions on Control Systems Technology*, Vol. 14, No. 1, 2006, pp. 91–98.

[18] Harkegard, O., "Efficient active set algorithms for solving constrained least squares problems in aircraft control allocation," *Decision and Control, 2002, Proceedings of the 41st IEEE Conference on*, Vol. 2, IEEE, 2002, pp. 1295–1300.

[19] van der Peijl, I., and de Visser, C., "Physical Splines for Aerodynamic Modelling of Innovative Control Effectors," *Msc Thesis at Delft University of Technology*, 2017.

[20] de Visser, C., Chu, Q., and Mulder, J., "A new approach to linear regression with multivariate splines," *Automatica*, Vol. 45, No. 12, 2009, pp. 2903 – 2909. doi:https://doi.org/10.1016/j.automatica.2009.09.017.

[21] Tol, H. J., de Visser, C. C., and Kotsonis, M., "Model reduction of parabolic PDEs using multivariate splines," *International Journal of Control*, Vol. 0, No. 0, 2016, pp. 1–16. doi:10.1080/00207179.2016.1222554, URL `https://doi.org/10.1080/00207179.2016.1222554`.

[22] Johnson, E. N., and Calise, A. J., "Pseudo-control hedging: A new method for adaptive control," *Advances in navigation guidance and control technology workshop*, 2000, pp. 1–2.

[23] Lam, Q., Barkana, I., and Grove, W., "Direct adaptive control treatment to flight control input saturation," *To be Presented at the AIAA 2005 GN&C Conference, AIAA2005-6179*, 2005.

[24] Johnson, E. N., and Kannan, S. K., "Adaptive trajectory control for autonomous helicopters," *Journal of Guidance Control and Dynamics*, Vol. 28, No. 3, 2005, pp. 524–538.

[25] Simplício, P., Pavel, M., van Kampen, E., and Chu, Q., "An acceleration measurements-based approach for helicopter nonlinear flight control using Incremental Nonlinear Dynamic Inversion," *Control Engineering Practice*, Vol. 21, No. 8, 2013, pp. 1065 – 1077. doi:https://doi.org/10.1016/j.conengprac.2013.03.009, URL `http://www.sciencedirect.com/science/article/pii/S0967066113000634`.

[26] Boskovic, J. D., Yu, S.-H., and Mehra, R. K., "A stable scheme for automatic control reconfiguration in the presence of actuator failures," *American Control Conference, 1998. Proceedings of the 1998*, Vol. 4, IEEE, 1998, pp. 2455–2459.

[27] Edwards, C., Lombaerts, T., Smaili, H., et al., "Fault tolerant flight control," *Lecture Notes in Control and Information Sciences*, Vol. 399, 2010, pp. 1–560.

A. Aerodynamic equations of the ICE model

The force coefficients C_X, C_Y, C_Z and the moment coefficients C_L, C_M and C_N shown in equations 36 to 41 respectively consist of up to 18 coefficients. The coefficients that start with the Δ sign indicate increments due to the influence of the first effector on the second effector mentioned in the the dependent variables on that coefficient. For example in equation 36:$\Delta C_{X_8}(\alpha, \delta_{lamt}, \delta_{lel})$ means an increment increase due to the influence of the LAMT on the LEL.

$$\begin{aligned}
C_X = {} & C_{X_1}(\alpha, M) + C_{X_2}(\alpha, \beta, M) + C_{X_3}(\alpha, \beta, M, \delta_{liblef}) \\
& + C_{X_4}(\alpha, \beta, M, \delta_{liblef}, \delta_{loblef}) + C_{X_5}(\alpha, M, \delta_{lssd}, \delta_{lel}) + C_{X_6}(\alpha, M, \delta_{lssd}, \delta_{lel}, \delta_{pf}) \\
& + C_{X_7}(\alpha, \delta_{lel}, \delta_{lamt}) + \Delta C_{X_8}(\alpha, \delta_{lamt}, \delta_{lel}) + \Delta C_{X_9}(\alpha, \delta_{loblef}, \delta_{lamt}) \\
& + \Delta C_{X_{10}}(\alpha, \delta_{ramt}, \delta_{rel}) + \Delta C_{X_{11}}(\alpha, \delta_{roblef}, \delta_{ramt}) + C_{X_{12}}(\alpha, \beta, \delta_{lssd}) \\
& + C_{X_{13}}(\alpha, \beta, \delta_{riblef}) + C_{X_{14}}(\alpha, \beta, M, \delta_{riblef}, \delta_{roblef}) + C_{X_{15}}(\alpha, M, \delta_{rssd}, \delta_{rel}) \\
& + C_{X_{16}}(\alpha, \beta, \delta_{ramt}) + C_{X_{17}}(\alpha, \beta, \delta_{rssd})
\end{aligned} \tag{36}$$

$$\begin{aligned}
C_Y = {} & C_{Y_1}(\alpha, M) + C_{Y_2}(\alpha, \beta, M) - C_{Y_3}(\alpha, \beta, M, \delta_{liblef}) \\
& - C_{Y_4}(\alpha, \beta, M, \delta_{liblef}, \delta_{loblef}) + C_{Y_5}(\alpha, M, \delta_{lssd}, \delta_{lel}) + C_{Y_6}(\alpha, \delta_{lel}, \delta_{lamt}) \\
& + C_{Y_7}(\alpha, \beta, \delta_{lssd}) + \Delta C_{Y_8}(\alpha, \delta_{lamt}, \delta_{lel}) + \Delta C_{Y_9}(\alpha, \delta_{loblef}, \delta_{lamt}) \\
& - \Delta C_{Y_{10}}(\alpha, \delta_{ramt}, \delta_{rel}) + \Delta C_{Y_{11}}(\alpha, \delta_{roblef}, \delta_{ramt}) + C_{Y_{12}}(\alpha, \beta, \delta_{riblef}) \\
& + C_{Y_{13}}(\alpha, \beta, M, \delta_{riblef}, \delta_{roblef}) - C_{Y_{14}}(\alpha, M, \delta_{rssd}, \delta_{rel}) - C_{Y_{15}}(\alpha, \beta, \delta_{ramt}) \\
& - C_{Y_{16}}(\alpha, \beta, \delta_{rssd})
\end{aligned} \tag{37}$$

$$\begin{aligned}
C_Z = {} & C_{Z_1}(\alpha, M) + C_{Z_2}(\alpha, \beta, M) + C_{Z_3}(\alpha, \beta, M, \delta_{liblef}) \\
& + C_{Z_4}(\alpha, \beta, M, \delta_{liblef}, \delta_{loblef}) + C_{Z_5}(\alpha, M, \delta_{lssd}, \delta_{lel}) + C_{Z_6}(\alpha, M, \delta_{lssd}, \delta_{rssd}, \delta_{pf}) \\
& + C_{Z_7}(\alpha, \beta, \delta_{lamt}) + \Delta C_{Z_8}(\alpha, \delta_{lamt}, \delta_{lel}) + \Delta C_{Z_9}(\alpha, \delta_{loblef}, \delta_{lamt}) \\
& + \Delta C_{Z_{10}}(\alpha, \delta_{ramt}, \delta_{rel}) + \Delta C_{Z_{11}}(\alpha, \delta_{roblef}, \delta_{ramt}) + C_{Z_{12}}(\alpha, \beta, \delta_{lssd}) \\
& + C_{Z_{13}}(\alpha, \beta, \delta_{riblef}) + C_{Z_{14}}(\alpha, \beta, M, \delta_{riblef}, \delta_{roblef}) + C_{Z_{15}}(\alpha, M, \delta_{rssd}, \delta_{rel}) \\
& + C_{Z_{16}}(\alpha, \beta, \delta_{ramt}) + C_{Z_{17}}(\alpha, \beta, \delta_{rssd}) + \frac{\bar{c} \cdot q}{2V} C_{Z_{18}}(\alpha, M)
\end{aligned} \tag{38}$$

$$\begin{aligned}
C_L = {} & C_{L_1}(\alpha, M) + C_{L_2}(\alpha, \beta, M) - C_{L_3}(\alpha, \beta, \delta_{liblef}) \\
& - C_{L_4}(\alpha, \beta, M, \delta_{liblef}, \delta_{loblef}) + C_{L_5}(\alpha, M, \delta_{lel}, \delta_{lssd}) + C_{L_6}(\alpha, M, \delta_{lel}, \delta_{lamt}) \\
& - C_{L_7}(\alpha, M, \delta_{lssd}) + \Delta C_{L_8}(\alpha, \delta_{lamt}, \delta_{lel}) + \Delta C_{L_9}(\alpha, \delta_{loblef}, \delta_{lamt}) \\
& - \Delta C_{L_{10}}(\alpha, \delta_{ramt}, \delta_{rel}) - \Delta C_{L_{11}}(\alpha, \delta_{roblef}, \delta_{ramt}) + C_{L_{12}}(\alpha, \beta, \delta_{ribref}) \\
& + C_{L_{13}}(\alpha, \beta, \delta_{riblef}, \delta_{robref}) - C_{L_{14}}(\alpha, \beta, M, \delta_{rssd}, \delta_{rel}) - C_{L_{15}}(\alpha, M, \delta_{ramt}) \\
& - C_{L_{16}}(\alpha, \beta, \delta_{rssd}) + \frac{b \cdot p}{2V} C_{L_{17}}(\alpha, M) + \frac{b \cdot r}{2V} C_{L_{18}}(\alpha, M)
\end{aligned} \tag{39}$$

$$\begin{aligned}
C_M = {} & C_{M_1}(\alpha, M) + C_{M_2}(\alpha, \beta, M) + C_{M_3}(\alpha, \beta, \delta_{liblef}) \\
& + C_{M_4}(\alpha, \beta, M, \delta_{liblef}, \delta_{loblef}) + C_{M_5}(\alpha, M, \delta_{lel}, \delta_{lssd}) + C_{M_6}(\alpha, M, \delta_{lssd}, \delta_{rssd}, \delta_{pf}) \\
& + C_{M_7}(\alpha, \beta, \delta_{lamt}) + \Delta C_{M_8}(\alpha, \delta_{lamt}, \delta_{lel}) + \Delta C_{M_9}(\alpha, \delta_{loblef}, \delta_{lamt}) \\
& + \Delta C_{M_{10}}(\alpha, \delta_{ramt}, \delta_{rel}) + \Delta C_{M_{11}}(\alpha, \delta_{roblef}, \delta_{ramt}) + C_{M_{12}}(\alpha, \beta, \delta_{lssd}) \\
& + C_{M_{13}}(\alpha, \beta, \delta_{riblef}) + C_{M_{14}}(\alpha, \beta, \delta_{riblef}, \delta_{robref}) + C_{M_{15}}(\alpha, \beta, M, \delta_{rssd}, \delta_{rel}) \\
& + C_{M_{16}}(\alpha, M, \delta_{ramt}) + C_{M_{17}}(\alpha, \beta, \delta_{rssd}) + \frac{\bar{c} \cdot q}{2V} C_{M_{18}}(\alpha, M)
\end{aligned} \tag{40}$$

$$\begin{aligned}
C_N = {} & C_{N_1}(\alpha, M) + C_{N_2}(\alpha, \beta, M) - C_{N_3}(\alpha, \beta, M, \delta_{liblef}) - C_{N_4}(\alpha, \beta, M, \delta_{liblef}, \delta_{loblef}) \\
& + C_{N_5}(\alpha, M, \delta_{lssd}, \delta_{lel}) + C_{N_6}(\alpha, M, \delta_{lel}, \delta_{lamt}) + C_{N_7}(\alpha, \beta, \delta_{lssd}) + \Delta C_{N_8}(\alpha, \delta_{lamt}, \delta_{lel}) \\
& + \Delta C_{N_9}(\alpha, \delta_{loblef}, \delta_{lamt}) - \Delta C_{N_{10}}(\alpha, \delta_{ramt}, \delta_{rel}) - \Delta C_{N_{11}}(\alpha, \delta_{roblef}, \delta_{ramt}) \\
& + C_{N_{12}}(\alpha, \beta, \delta_{riblef}) + C_{N_{13}}(\alpha, \beta, M, \delta_{riblef}, \delta_{roblef}) - C_{N_{14}}(\alpha, M, \delta_{rssd}, \delta_{rel}) \\
& - C_{N_{15}}(\alpha, \beta, \delta_{ramt}) - C_{N_{16}}(\alpha, \beta, \delta_{rssd}) + \frac{b \cdot p}{2V} C_{N_{17}}(\alpha, M) + \frac{b \cdot r}{2V} C_{N_{18}}(\alpha, M)
\end{aligned} \tag{41}$$

B. Inputs and output of the base ICE model

In figure 22 the original ICE aircraft model is shown. The outputs of this model are the velocity in inertial axis V_e, the position in inertial axis X_e, the body Euler angles ϕ, θ and ψ, the velocities in the body axis u, v and w, the rotation rates in the body axis p, q and r, the body rotational acceleration in the body axis $\dot{p}$, $\dot{q}$ and $\dot{r}$ and the accelerations in the body axis a_x, a_y and a_z. Further outputs of the model are the dynamic pressure $\bar{q}$, the airspeed V, the Mach number M, the angle of attack α and the sideslip angle β. For the computation of the aerodynamic coefficients, look-up tables are used from experimental data and results outside of the range are extrapolated linearly for low AOA and clipped for high AOA. Linear interpolation should be performed for α, β and M and cubic spline interpolation everywhere else. Note that this was not fully implemented in the model provided. Not all aerodynamic coefficients are defined on the same range of α, β and M. For example C_{X_1} is defined on $[-5°, 90°]$ while C_{X_3} is defined on $[-2.5°, 45°]$ AOA.

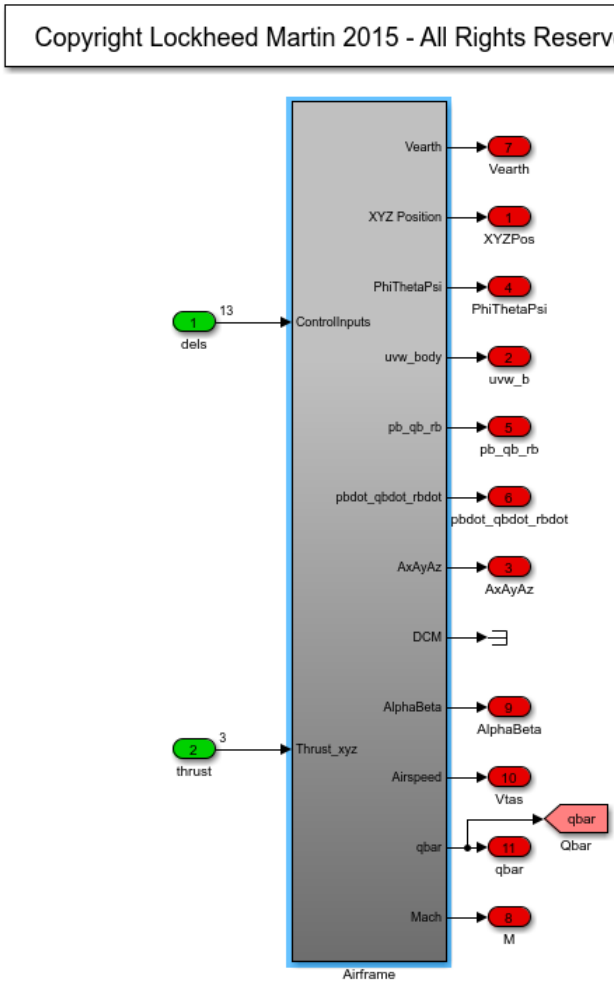

Fig. 22 ICE aircraft model as designed originally [16]

B

Straight Flight: example test cases

run (#)	time (s)	V_{min} (ft/s)	V_{max} (ft/s)	$n_{z_{max}}$ (-)	α_{max} (deg)	RMS (deg/s)
1.0	40.0	120.8	133.0	4.939	27.53	28.91
2.0	11.68	71.54	134.6	6.103	170.2	-
3.0	11.97	67.46	133.8	5.89	179.7	-
4.0	40.0	86.86	134.2	5.596	41.41	57.93
5.0	40.0	117.3	135.3	5.119	27.8	44.21
6.0	40.0	99.05	133.6	6.304	36.07	38.67
7.0	40.0	101.6	134.7	5.385	33.93	47.66
8.0	40.0	91.13	133.7	6.116	37.77	47.23
9.0	8.51	87.35	135.5	4.007	179.6	-
10.0	40.0	99.93	135.2	5.562	32.53	42.23
11.0	40.0	113.2	133.2	4.419	28.08	27.85
12.0	40.0	71.59	135.9	6.281	59.58	98.14
13.0	40.0	120.0	133.1	4.778	25.93	32.17
14.0	40.0	112.3	134.9	5.552	30.58	28.5
15.0	40.0	116.4	135.6	4.2	26.02	25.98
16.0	40.0	46.34	138.4	8.196	85.53	74.94
17.0	40.0	124.9	133.8	4.207	23.92	25.38
18.0	13.97	68.03	135.7	9.442	150.3	-
19.0	40.0	114.4	137.3	5.739	30.04	33.18
20.0	40.0	109.8	133.4	6.198	36.39	31.46

Table B.1: RSSD failure tests at 59 degrees for straight flight at FL100 and 430 ft/s

run (#)	time (s)	V_{min} (ft/s)	V_{max} (ft/s)	$n_{z_{max}}$ (-)	α_{max} (deg)	RMS (deg/s)
21.0	40.0	129.1	135.2	2.057	11.64	11.37
22.0	40.0	129.4	134.0	1.468	9.584	4.518
23.0	40.0	129.3	135.1	1.63	10.14	9.467
24.0	40.0	129.1	135.4	1.67	9.932	9.768
25.0	40.0	128.7	135.5	3.292	16.72	17.13
26.0	40.0	128.8	135.1	2.307	14.39	13.58
27.0	40.0	129.0	134.5	2.035	12.45	12.9
28.0	40.0	129.4	134.9	1.817	10.93	10.26
29.0	40.0	129.1	134.1	1.557	9.707	6.636
30.0	40.0	129.2	135.2	1.404	9.224	5.127
31.0	40.0	129.2	134.4	1.55	9.853	5.047
32.0	40.0	129.0	136.4	1.402	8.863	6.428
33.0	40.0	129.4	134.2	1.744	10.39	5.877
34.0	40.0	129.2	135.9	1.839	11.06	10.58
35.0	40.0	129.2	134.3	1.682	10.33	7.934
36.0	40.0	129.3	133.8	1.51	9.563	4.594
37.0	40.0	129.4	135.3	1.569	9.861	5.602
38.0	40.0	129.4	134.2	1.992	11.7	12.95
39.0	40.0	126.8	134.5	2.776	17.62	17.13
40.0	40.0	129.3	134.8	1.55	9.677	7.909

Table B.2: RAMT failure tests at 59 degrees for straight flight at FL100 and 430 ft/s

run (#)	time (s)	V_{min} (ft/s)	V_{max} (ft/s)	$n_{z_{max}}$ (-)	α_{max} (deg)	RMS (deg/s)
41.0	40.0	101.6	133.2	5.908	33.93	31.28
42.0	40.0	88.99	135.8	5.755	39.12	46.63
43.0	40.0	112.9	134.9	5.648	29.92	33.54
44.0	10.77	91.13	134.0	8.464	174.9	-
45.0	40.0	116.1	133.8	5.026	30.39	29.69
46.0	11.87	74.09	134.2	7.756	87.87	-
47.0	40.0	69.13	133.7	8.214	63.29	46.39
48.0	40.0	104.2	138.6	8.405	64.71	68.72
49.0	40.0	85.43	134.9	8.35	57.81	42.98
50.0	40.0	101.0	134.8	5.849	37.34	47.37
51.0	40.0	124.7	134.8	4.384	24.96	25.83
52.0	40.0	114.2	134.7	4.552	29.18	26.3
53.0	40.0	117.5	134.3	4.75	26.73	24.01
54.0	40.0	113.8	133.8	5.23	30.43	31.78
55.0	29.83	84.91	162.3	6.223	87.85	-
56.0	40.0	97.52	133.8	7.229	68.48	53.09
57.0	40.0	81.96	161.0	10.45	99.22	49.66
58.0	27.04	38.61	135.1	7.593	179.2	-
59.0	40.0	117.7	133.4	4.727	25.89	27.24
60.0	40.0	119.4	135.1	4.433	25.08	26.76

Table B.3: LSSD failure tests at 59 degrees for straight flight at FL100 and 430 ft/s

run (#)	time (s)	V_{min} (ft/s)	V_{max} (ft/s)	$n_{z_{max}}$ (-)	α_{max} (deg)	RMS (deg/s)
61.0	40.0	129.2	134.2	1.42	9.143	4.669
62.0	40.0	128.9	135.7	1.733	10.78	7.867
63.0	40.0	129.2	134.7	1.721	10.56	9.94
64.0	40.0	129.5	135.0	1.538	9.758	4.902
65.0	40.0	129.5	135.2	1.595	10.13	4.721
66.0	40.0	129.6	134.6	1.581	10.86	12.09
67.0	40.0	128.6	134.6	1.496	9.591	7.073
68.0	40.0	128.6	134.8	1.926	12.73	12.89
69.0	40.0	129.0	134.2	1.771	10.8	7.645
70.0	40.0	128.9	134.4	1.771	10.57	8.672
71.0	40.0	129.0	135.2	2.117	14.14	19.61
72.0	40.0	129.3	134.1	1.811	11.58	7.196
73.0	40.0	128.4	135.6	3.387	18.96	22.33
74.0	40.0	128.3	135.5	2.015	12.09	11.82
75.0	40.0	129.2	134.7	1.746	11.06	8.965
76.0	40.0	127.7	137.3	1.577	9.936	5.021
77.0	40.0	128.4	134.9	3.151	16.66	14.99
78.0	40.0	129.0	135.7	1.587	10.38	5.809
79.0	40.0	128.8	135.7	2.211	13.44	12.0
80.0	40.0	129.1	134.2	1.512	9.594	7.097

Table B.4: LAMT failure tests at 59 degrees for straight flight at FL100 and 430 ft/s

C

Evasive manoeuvre: example test cases

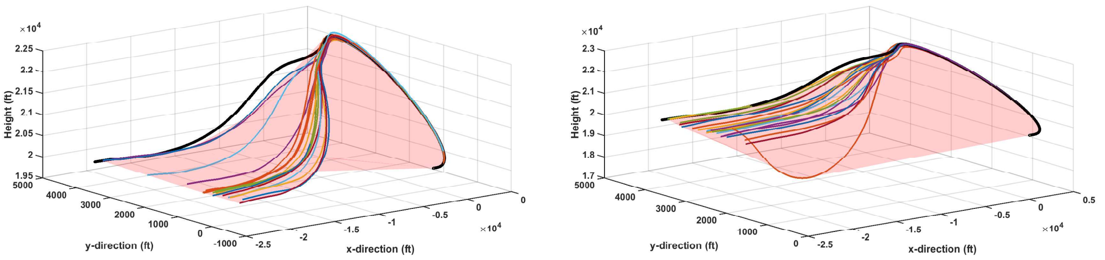

(a) (b)

Figure C.1: (a) realisation of the YTV failure stuck at 1 degrees (b) realisation of the YTV failure stuck at -1 degrees. Both are measured at FL200 and velocity of 880 fps for 40 second flight with failure time $T = 5$

run (#)	time (s)	V_{min} (ft/s)	V_{max} (ft/s)	$n_{z_{max}}$ (-)	α_{max} (deg)	RMS (deg/s)
1.0	40.0	133.4	272.8	9.722	34.62	16.06
2.0	40.0	132.1	271.0	9.607	36.14	19.63
3.0	40.0	129.1	270.9	9.745	38.31	23.9
4.0	40.0	125.0	270.8	9.689	41.61	27.23
5.0	40.0	140.4	271.9	9.541	32.28	13.8
6.0	40.0	135.6	272.4	9.899	34.75	14.41
7.0	40.0	129.5	271.8	9.888	37.27	17.51
8.0	40.0	129.2	271.8	9.83	38.38	15.94
9.0	40.0	130.3	272.1	9.789	38.49	21.8
10.0	40.0	134.9	270.9	9.689	35.95	17.24
11.0	40.0	129.0	270.7	9.883	46.94	25.71
12.0	40.0	119.2	271.9	9.615	42.69	25.42
13.0	40.0	121.2	272.9	9.59	39.1	20.55
14.0	27.29	133.8	269.3	15.63	170.0	-
15.0	40.0	137.6	270.6	9.746	33.37	14.34
16.0	27.88	139.2	271.4	13.28	178.4	-
17.0	40.0	125.3	274.2	9.937	39.35	18.26
18.0	40.0	143.1	271.5	9.708	32.84	13.6
19.0	40.0	131.1	271.8	9.714	36.04	17.08
20.0	40.0	137.4	270.6	14.47	36.37	36.95

Table C.1: Realisation data of 40 seconds of evasive flight at FL200 and velocity 880 fps for failure of LLEFO (40 deg)

run (#)	time (s)	V_{min} (ft/s)	V_{max} (ft/s)	$n_{z_{max}}$ (-)	α_{max} (deg)	RMS (deg/s)
21.0	40.0	104.4	269.3	9.798	66.19	31.71
22.0	24.17	83.97	269.6	17.68	179.7	0
23.0	40.0	113.1	270.2	9.798	68.25	33.9
24.0	40.0	113.6	269.6	10.0	65.02	33.1
25.0	40.0	109.9	268.9	9.453	71.93	33.06
26.0	40.0	112.2	269.3	9.517	66.4	32.24
27.0	40.0	111.3	271.6	9.716	70.09	31.16
28.0	40.0	113.7	269.7	9.972	73.29	33.43
29.0	40.0	110.9	269.9	9.862	66.16	32.73
30.0	40.0	107.6	269.2	9.767	66.4	29.8
31.0	40.0	105.7	272.0	9.726	69.01	33.2
32.0	40.0	111.8	269.1	9.965	63.54	31.82
33.0	40.0	112.2	269.5	10.01	66.87	29.59
34.0	40.0	107.6	268.7	9.734	65.19	31.65
35.0	40.0	109.1	269.4	9.769	68.97	31.11
36.0	40.0	109.3	269.6	10.11	68.97	43.39
37.0	40.0	113.2	269.2	9.512	69.24	36.77
38.0	40.0	114.2	269.7	10.1	66.38	34.84
39.0	40.0	113.4	268.5	9.911	69.97	31.17
40.0	40.0	106.6	270.2	9.899	67.58	34.48

Table C.2: Realisation data of 40 seconds of evasive flight at FL200 and velocity 880 fps for failure of LELE (-30 deg)

run (#)	time (s)	V_{min} (ft/s)	V_{max} (ft/s)	$n_{z_{max}}$ (-)	α_{max} (deg)	RMS (deg/s)
41.0	40.0	197.7	272.3	9.968	16.99	23.18
42.0	40.0	188.0	271.8	9.971	19.54	20.17
43.0	40.0	189.6	270.0	9.864	18.76	20.21
44.0	40.0	191.8	270.3	10.07	18.27	21.39
45.0	40.0	183.4	270.2	9.855	17.93	19.92
46.0	40.0	198.8	270.2	10.14	17.4	23.69
47.0	40.0	188.2	270.5	9.924	18.99	18.25
48.0	40.0	198.6	271.8	10.04	17.55	21.16
49.0	40.0	196.5	272.1	10.18	17.52	21.99
50.0	40.0	193.1	269.6	10.26	18.01	21.12
51.0	40.0	198.2	270.7	9.903	17.14	23.41
52.0	40.0	192.6	269.9	10.09	19.14	21.0
53.0	40.0	193.6	269.5	9.925	18.2	19.81
54.0	40.0	200.9	271.0	10.36	17.84	23.49
55.0	40.0	188.9	270.0	9.949	18.48	20.51
56.0	40.0	198.6	270.7	9.962	17.39	23.54
57.0	40.0	192.9	270.7	9.872	19.96	18.44
58.0	40.0	198.4	271.6	10.11	18.03	21.35
59.0	40.0	195.9	270.8	9.984	17.67	21.64
60.0	40.0	196.5	271.4	9.868	17.66	23.26

Table C.3: Realisation data of 40 seconds of evasive flight at FL200 and velocity 880 fps for failure of LELE (30 deg)

run (#)	time (s)	V_{min} (ft/s)	V_{max} (ft/s)	$n_{z_{max}}$ (-)	α_{max} (deg)	RMS (deg/s)
61.0	40.0	150.1	272.5	9.786	29.2	16.25
62.0	40.0	161.3	272.1	9.734	25.15	15.82
63.0	40.0	163.4	272.5	11.59	29.86	39.95
64.0	40.0	143.4	273.0	9.976	32.49	13.1
65.0	40.0	147.1	272.2	9.991	28.81	9.053
66.0	40.0	167.2	272.6	9.899	25.05	15.09
67.0	40.0	144.6	272.0	10.47	61.29	51.83
68.0	40.0	143.4	274.3	9.934	29.06	13.06
69.0	40.0	162.9	272.1	9.735	25.6	39.81
70.0	40.0	151.0	272.9	9.886	27.47	26.92
71.0	40.0	154.0	271.8	9.676	26.74	25.9
72.0	40.0	154.0	272.1	9.964	28.07	17.95
73.0	40.0	155.5	273.6	9.858	26.96	25.18
74.0	40.0	146.2	272.1	9.865	29.38	10.39
75.0	40.0	155.3	271.6	9.963	27.28	29.77
76.0	18.0	160.4	269.2	9.637	179.1	-
77.0	20.31	143.5	268.7	13.91	179.8	-
78.0	40.0	164.7	276.4	9.752	24.91	19.22
79.0	40.0	140.2	271.6	9.848	31.65	14.98
80.0	40.0	164.8	274.2	9.67	24.15	18.72

Table C.4: Realisation data of 40 seconds of evasive flight at FL200 and velocity 880 fps for failure of LSSD (0 deg)

run (#)	time (s)	V_{min} (ft/s)	V_{max} (ft/s)	$n_{z_{max}}$ (-)	α_{max} (deg)	RMS (deg/s)
81.0	38.49	92.17	269.3	11.79	166.3	-
82.0	29.33	100.8	268.9	9.915	93.36	-
83.0	27.55	99.02	269.1	9.766	178.4	-
84.0	18.14	84.95	269.0	9.626	162.8	-
85.0	17.77	105.0	269.1	9.763	136.1	-
86.0	19.68	85.5	268.9	10.42	152.1	-
87.0	12.11	119.8	268.6	9.911	100.4	-
88.0	12.18	124.1	269.0	9.779	98.46	-
89.0	20.9	77.84	269.3	9.804	78.64	-
90.0	12.32	132.9	270.2	9.752	108.3	-
91.0	22.49	66.71	269.9	9.772	179.8	-
92.0	22.06	143.6	268.9	17.25	84.63	-
93.0	13.2	133.9	269.0	13.6	90.01	-
94.0	26.64	109.9	270.9	9.901	90.08	-
95.0	23.4	99.61	268.8	9.794	179.6	-
96.0	12.61	128.3	269.0	10.28	179.1	-
97.0	12.93	124.9	269.2	9.76	179.4	-
98.0	21.03	85.9	269.8	9.964	163.2	-
99.0	18.18	99.46	268.9	9.833	168.6	-
100.0	20.28	95.05	268.9	9.833	179.2	-

Table C.5: Realisation data of 40 seconds of evasive flight at FL200 and velocity 880 fps for failure of LSSD (56 deg)

run (#)	time (s)	V_{min} (ft/s)	V_{max} (ft/s)	$n_{z_{max}}$ (-)	α_{max} (deg)	RMS (deg/s)
101.0	40.0	148.4	271.2	9.935	27.65	10.16
102.0	40.0	133.0	272.3	9.778	34.52	12.25
103.0	40.0	139.0	271.3	9.702	33.5	12.78
104.0	40.0	137.8	271.7	9.791	39.57	24.86
105.0	40.0	149.3	271.1	9.695	28.19	11.1
106.0	40.0	136.7	271.2	9.925	45.55	27.51
107.0	40.0	146.2	271.6	9.422	28.44	11.77
108.0	40.0	166.2	272.0	9.975	24.76	7.629
109.0	40.0	131.9	271.5	9.724	37.44	17.47
110.0	40.0	144.1	271.5	9.792	28.31	12.4
111.0	40.0	155.8	271.6	9.987	26.92	6.907
112.0	40.0	137.6	272.6	9.639	34.85	11.3
113.0	40.0	127.5	271.1	9.57	39.6	31.8
114.0	40.0	146.3	272.7	10.06	27.9	11.24
115.0	40.0	157.2	269.8	9.851	23.52	10.89
116.0	40.0	138.2	270.4	10.03	33.48	12.67
117.0	40.0	126.7	270.8	9.671	37.45	18.78
118.0	40.0	161.0	271.5	9.718	25.98	5.229
119.0	40.0	132.9	271.6	9.734	35.17	14.34

Table C.6: Realisation data of 40 seconds of evasive flight at FL200 and velocity 880 fps for failure of RLEFO (40 deg)

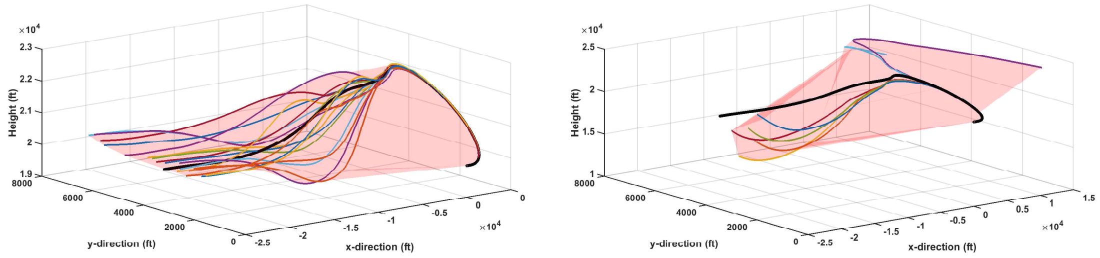

(a) (b)

Figure C.2: (a) realisation of the LSSD failure stuck at 0 degrees (b) realisation of the RSSD failure stuck at 53 degrees. Both are measured at FL200 and velocity of 880 fps for 40 second flight with failure time $T = 5$

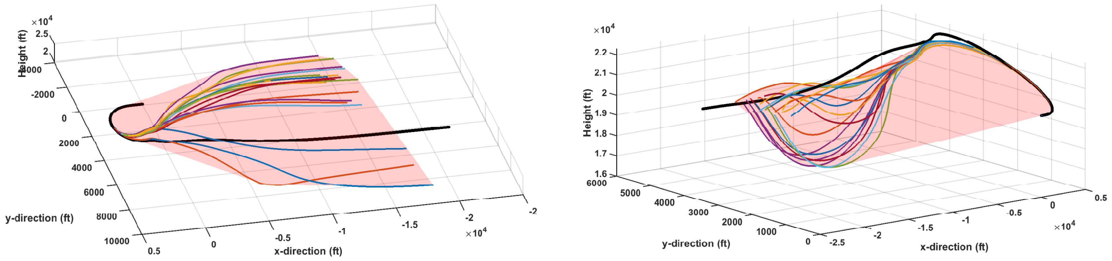

(a) (b)

Figure C.3: (a) realisation of the RELE failure stuck at 30 degrees (b) realisation of the RELE failure stuck at -30 degrees. Both are measured at FL200 and velocity of 880 fps for 40 second flight with failure time $T = 5$

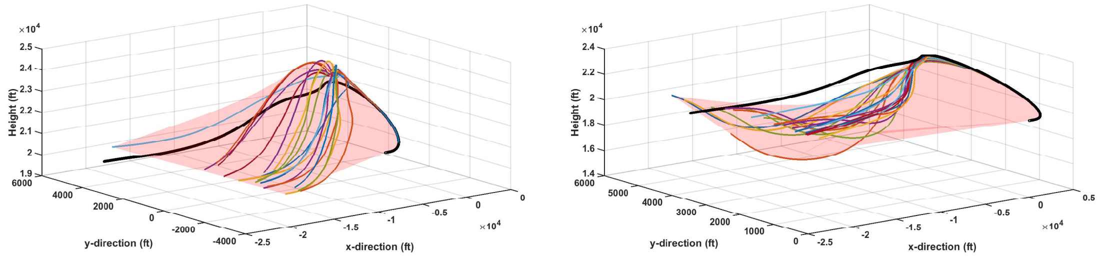

(a) (b)

Figure C.4: (a) realisation of the LELE failure stuck at -30 degrees (b) realisation of the RAMT failure stuck at 60 degrees. Both are measured at FL200 and velocity of 880 fps for 40 second flight with failure time $T = 5$

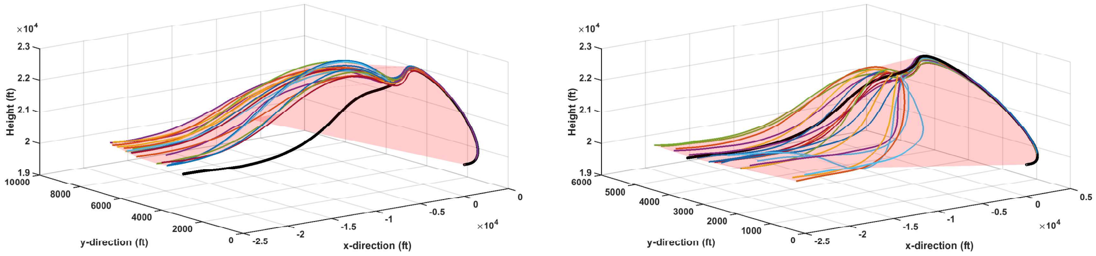

(a) (b)

Figure C.5: (a) realisation of the LLEFO failure stuck at 40 degrees (b) realisation of the RLEFO failure stuck at 40 degrees. Both are measured at FL200 and velocity of 880 fps for 40 second flight with failure time $T = 5$

run (#)	time (s)	V_{min} (ft/s)	V_{max} (ft/s)	$n_{z_{max}}$ (-)	α_{max} (deg)	RMS (deg/s)
120.0	40.0	127.9	270.7	9.721	38.88	33.79
121.0	40.0	123.7	269.7	9.638	54.19	22.97
122.0	40.0	143.1	268.6	9.744	41.28	23.14
123.0	40.0	124.3	269.0	9.806	56.9	27.06
124.0	40.0	127.3	270.4	9.716	56.12	28.59
125.0	40.0	152.0	269.4	9.697	28.94	13.27
126.0	40.0	120.5	269.6	9.774	57.59	23.86
127.0	40.0	122.5	269.1	10.03	62.07	28.6
128.0	40.0	165.7	269.9	9.964	27.07	13.96
129.0	40.0	140.2	269.4	10.11	33.08	18.83
130.0	40.0	125.3	269.8	9.668	57.28	24.23
131.0	40.0	124.0	270.0	9.806	61.7	27.38
132.0	40.0	143.0	268.5	9.803	37.65	18.28
133.0	40.0	124.3	269.4	10.22	47.02	21.16
134.0	40.0	121.3	269.4	9.935	61.86	28.41
135.0	40.0	122.2	269.7	9.912	52.6	28.04
136.0	40.0	123.6	269.2	10.13	51.81	29.13
137.0	40.0	168.0	270.2	9.894	26.0	13.84
138.0	40.0	155.2	270.0	9.988	28.36	14.37
139.0	40.0	138.8	270.1	9.734	32.03	22.19
140.0	40.0	127.2	269.7	9.754	65.78	25.92

Table C.7: Realisation data of 40 seconds of evasive flight at FL200 and velocity 880 fps for failure of RAMT (60 deg)

run (#)	time (s)	V_{min} (ft/s)	V_{max} (ft/s)	$n_{z_{max}}$ (-)	α_{max} (deg)	RMS (deg/s)
141.0	40.0	148.7	269.1	10.25	35.51	16.56
142.0	17.61	138.6	268.8	10.24	176.2	-
143.0	40.0	143.0	269.1	10.08	43.66	21.73
144.0	40.0	160.4	270.2	9.843	29.34	13.55
145.0	40.0	144.3	269.6	9.983	41.26	23.94
146.0	40.0	141.2	269.5	10.06	36.69	19.61
147.0	40.0	144.8	268.9	10.26	59.52	30.58
148.0	40.0	123.1	269.5	10.25	56.71	34.21
149.0	40.0	132.6	268.7	10.45	55.61	29.61
150.0	40.0	144.5	269.6	9.97	34.58	18.22
151.0	40.0	122.6	270.0	9.937	51.96	22.44
152.0	40.0	135.7	271.6	9.882	51.41	29.34
153.0	40.0	129.8	269.3	10.11	62.75	33.97
154.0	40.0	145.4	270.5	10.12	34.69	15.43
155.0	40.0	132.0	269.4	9.854	51.44	30.52
156.0	40.0	125.5	269.1	10.38	51.46	23.79
157.0	40.0	135.1	271.0	10.03	39.59	20.62
158.0	18.21	121.3	269.7	9.835	147.6	-
159.0	40.0	127.9	269.6	9.777	54.84	29.84
160.0	40.0	130.7	268.8	9.884	52.92	27.6

Table C.8: Realisation data of 40 seconds of evasive flight at FL200 and velocity 880 fps for failure of RELE (-30 deg)

run (#)	time (s)	V_{min} (ft/s)	V_{max} (ft/s)	$n_{z_{max}}$ (-)	α_{max} (deg)	RMS (deg/s)
161.0	21.02	134.3	268.9	9.951	179.8	-
162.0	20.34	111.6	269.6	9.839	65.38	-
163.0	40.0	145.0	269.3	9.968	63.79	27.5
164.0	40.0	139.8	269.3	9.869	56.31	28.52
165.0	18.01	140.5	268.2	16.11	63.9	-
166.0	21.43	134.5	270.2	14.92	66.46	-
167.0	21.61	140.3	268.3	9.734	178.7	-
168.0	24.9	134.2	270.7	9.782	175.4	-
169.0	18.49	134.6	269.7	23.56	178.7	-
170.0	18.71	120.5	269.0	9.765	179.7	-
171.0	26.7	125.4	268.7	13.06	101.6	-
172.0	18.71	141.5	269.2	10.75	96.27	-
173.0	17.97	129.4	268.4	9.98	113.3	-
174.0	40.0	134.4	268.5	9.752	52.06	32.87
175.0	40.0	104.5	268.2	9.824	107.0	57.14
176.0	19.99	103.4	269.0	18.26	129.0	-
177.0	40.0	134.7	269.6	9.865	57.66	26.03
178.0	40.0	33.97	268.9	10.88	89.37	54.28
179.0	17.73	131.1	269.7	9.677	72.83	-
180.0	40.0	138.5	269.5	9.92	46.04	36.82

Table C.9: Realisation data of 40 seconds of evasive flight at FL200 and velocity 880 fps for failure of RSSD (53 deg)

run (#)	time (s)	V_{min} (ft/s)	V_{max} (ft/s)	$n_{z_{max}}$ (-)	α_{max} (deg)	RMS (deg/s)
181.0	13.03	127.9	268.2	10.05	176.8	-
182.0	40.0	121.2	272.4	9.451	64.83	39.6
183.0	13.25	131.8	268.4	9.861	175.4	-
184.0	19.19	97.07	270.0	9.88	98.92	-
185.0	15.53	114.9	270.1	9.523	96.86	-
186.0	40.0	126.6	272.5	9.532	63.67	37.29
187.0	19.86	125.6	269.2	16.13	179.8	-
188.0	19.22	94.84	269.4	11.69	178.6	-
189.0	14.89	105.2	268.6	10.07	121.8	-
190.0	19.23	131.4	269.6	9.806	77.34	-
191.0	12.68	120.3	269.1	9.917	147.3	-
192.0	14.49	119.1	271.4	9.524	89.78	-
193.0	12.84	125.8	269.8	9.79	165.9	-
194.0	14.25	124.7	270.5	9.939	88.63	-
195.0	18.57	95.19	269.4	9.567	111.0	-
196.0	22.5	130.2	268.8	20.71	150.8	-
197.0	15.01	126.7	270.5	9.563	115.5	-
198.0	40.0	143.5	269.4	9.612	35.41	22.83
199.0	13.68	127.6	269.3	13.12	179.5	-
200.0	18.65	120.1	269.2	9.813	135.4	-

Table C.10: Realisation data of 40 seconds of evasive flight at FL200 and velocity 880 fps for failure of PTV (-5 deg)

run (#)	time (s)	V_{min} (ft/s)	V_{max} (ft/s)	$n_{z_{max}}$ (-)	α_{max} (deg)	RMS (deg/s)
201.0	40.0	173.3	272.6	9.69	19.32	21.51
202.0	40.0	162.9	272.5	9.629	21.18	23.32
203.0	40.0	170.6	272.8	9.598	19.42	25.7
204.0	40.0	156.3	275.2	9.875	21.98	33.33
205.0	17.78	159.0	270.1	13.42	67.55	-
206.0	40.0	161.3	274.2	9.761	21.9	24.83
207.0	40.0	165.5	273.5	9.819	20.43	24.22
208.0	40.0	169.6	273.3	9.815	19.72	24.72
209.0	40.0	168.2	271.5	10.18	20.85	24.99
210.0	23.34	157.5	270.2	9.754	178.2	-
211.0	40.0	167.4	275.4	9.824	19.7	20.46
212.0	40.0	162.1	273.3	9.644	21.03	23.12
213.0	40.0	162.9	274.4	9.809	22.21	20.88
214.0	40.0	171.1	272.4	9.863	20.31	21.13
215.0	40.0	166.7	272.5	9.843	21.03	15.44
216.0	40.0	164.1	273.0	9.971	21.11	27.7
217.0	40.0	161.4	274.0	9.801	22.2	16.45
218.0	18.75	167.0	268.6	14.57	161.9	-
219.0	23.67	149.3	269.1	11.85	178.2	-
220.0	40.0	167.2	271.3	10.01	19.42	20.99

Table C.11: Realisation data of 40 seconds of evasive flight at FL200 and velocity 880 fps for failure of YTV (-1 deg)

run (#)	time (s)	V_{min} (ft/s)	V_{max} (ft/s)	$n_{z_{max}}$ (-)	α_{max} (deg)	RMS (deg/s)
221.0	40.0	162.7	272.3	10.02	20.48	18.89
222.0	40.0	162.3	271.8	9.85	20.96	18.43
223.0	40.0	167.9	271.5	9.737	20.84	17.04
224.0	40.0	171.7	272.7	9.768	20.01	14.68
225.0	40.0	156.7	272.6	9.546	22.78	19.41
226.0	40.0	163.3	272.7	9.531	21.73	19.6
227.0	18.43	169.6	269.5	20.42	38.91	-
228.0	40.0	167.3	274.2	9.913	20.65	16.2
229.0	40.0	159.5	273.6	9.855	21.43	17.92
230.0	40.0	155.6	271.0	9.928	24.59	25.68
231.0	40.0	159.0	273.5	9.909	22.0	19.85
232.0	40.0	156.3	273.3	9.761	24.26	23.08
233.0	40.0	164.5	271.6	9.898	21.09	21.08
234.0	40.0	157.4	271.3	9.606	23.54	23.11
235.0	40.0	169.8	274.8	9.848	20.12	14.0
236.0	40.0	167.6	272.5	9.937	20.72	20.83
237.0	40.0	162.9	273.3	9.548	21.88	17.8
238.0	40.0	164.2	271.5	9.786	21.1	18.57
239.0	40.0	162.1	273.2	9.828	21.07	20.29
240.0	40.0	153.9	272.2	9.617	22.49	21.31

Table C.12: Realisation data of 40 seconds of evasive flight at FL200 and velocity 880 fps for failure of YTV (1 deg)